Università degli Studi di Genova

Facoltà di Scienze M.F.N.

Dottorato XXXII Ciclo

PHD Thesis

The Beam Dump eXperiment

Luca Marsicano

Advisors:

Dott. Marco Battaglieri

Dott. Andrea Celentano

Contents

Introduction

Hadronic matter makes about 14% of the known universe. The remaining 86% is "Dark Matter" (DM). Since it does not interact with the ordinary matter via electromagnetic force, DM is not visible and, to date, it escaped detection.

The search for DM is one of the hottest topic in modern physics. Despite the increasing number of astrophysical and cosmological observations proving the existence, so far no particle physics experiment has detected DM yet. Up to now, most of the experimental efforts have been focused on the so called "WIMP" (*Weakly Interacting Massive Particle*) paradigm, which predicts heavy DM (10 GeV-10 TeV mass range) interacting with Standard Model (SM) particles via the weak force mediators (W or Z bosons). More recently, due to the lack of clear evidence of WIMPs, other models of DM gained the interest of the physics community. These models consider Light DM particles (LDM), in MeV-GeV mass range. Among LDM theories, the *Dark Photon* theory predicts the existence of a *Dark Sector* interacting with SM particles via a new massive vector boson (*Dark Photon*, *Heavy Photon* or A'), mediator of a new force. This scenario, despite being theoretically well motivated, is remarkably experimentally unexplored.

The *Beam Dump eXperiment* (BDX), is an approved experiment at Jefferson Lab (JLab), aiming to discover the DM predicted witihn the *Dark Photon* theory. The experiment uses the CEBAF (Continuous Electron Beam Accelerator Facility) 11 GeV electron beam, impinging on the JLab Hall-A beam-dump, to produce a beam of DM particles, detected by a $\sim 1\ m^3$ detector made of thallium doped cesium iodide (CsI(Tl)) crystals located $\sim 20\ m$ downstream. In order to achieve excellent background rejection, the experimental setup includes active vetos and passive shielding surrounding CsI(Tl) crystals.

Given the weakness of the DM-SM interaction, the scattering of a DM particle in the BDX detector is a rare event. Therefore, the characterization of the expected background is a critical aspect of the experiment. Both cosmogenic and penetrating SM particles produced by the beam interaction in the dump contribute to the background of the experiment. While the cosmogenic contribution can be measured during the experiment when

the beam is off, beam-related background can only be estimated via Monte Carlo (MC) simulations. Therefore, a careful assessment of possible systematics introduced by the MC is needed. The beam-correlated background characterization was made by measuring the muon flux produced by the interaction of the CEBAF beam with Hall-A dump in a dedicated experimental campaign in spring 2018 [1]. The comparison to the flux predicted by MC allowed us to validate the BDX simulation framework.

The reach of BDX, i.e. the region that the experiment can probe in the LDM theory parameter space, depends critically on the background rejection capability and signal detection efficiency. For this reason, the detector setup was fine-tuned through a dedicated study. The response to LDM and background events was evaluated for different setups and selection cuts. As a result of this procedure, the configuration resulting in the best sensitivity was selected [2]. The reach calculation was performed taking into account the different LDM production mechanisms, including the contribution of secondary particles produced in the beam-dump. In particular, the effect of the secondary positrons annihilation was found to be extremely significant. In the majority of the sensitivity studies, this contribution is neglected, but recent results [3] [4] demonstrated that this process significantly enhances the sensitivity of lepton beam-dump experiments.

Currently, the BDX collaboration is focused on the deployment and operation of a small detector, called BDX-MINI, built to perform a preliminary physics measurement searching for LDM at JLab. This test will pave the way to the realization of the full BDX experiment. The measurement is currently ongoing but results are expected by the end of this year.

During my PhD I was involved in all aspects of the BDX experiment: design, simulation, prototyping and data analysis. The main results of my work are reported in this thesis. This manuscript is organized as follows: the first Chapter provides an introduction to the theory of LDM, with particular attention to the *Dark Photon* paradigm; the second Chapter illustrates the BDX experimental setup, the LDM production and detection mechanisms and the expected backgrounds; Chapter 3 and 4 describe, respectively, the BDX-HODO measurement, with a detailed description of the simulations, and the BDX experimental setup and analysis cuts optimization. Chapter 5 reports about BDX-MINI detector characterization, calibration and sensitivity estimate. Finally, Chapter 6 describes in detail the calculation of the secondary positron annihilation contribution to the sensitivity of BDX and other electron-beam thick-target experiment.

Chapter 1

Light Dark Matter

1.1 The Hypothesis of Thermal Origin

From the second half of the last century, multiple proofs of the existence of Dark Matter (DM) resulteded from astrophysical and cosmological observations. Stellar rotation curves in galaxies and dwarf-galaxies, the power spectrum of temperature fluctuations in the Cosmic Microwave Background (CMB), the power spectrum of matter density fluctuations, the ratios of light element yields from Big Bang Nucleosynthesis (BBN), the morphology of galaxy cluster collisions and astrophysical mass measurements based on gravitational lensing, all consistently indicate that 85% of the matter and 25% of the total energy of our universe comprises an electrically neutral, non relativistic population of Dark Matter (see [5]) .

The Standard Model of elementary particles (SM) contemplates different neutral particles (Neutrons, Higgs Boson, Neutrinos etc.), but none of them can be a viable DM candidate: Neutron's and Higgs Boson's lifetimes are too short to accommodate current DM abundance and Neutrinos, whose masses satisfy $m_\nu \leq 1\ eV$, are relativistic throughout much of cosmological evolution, which would have inhibited the formation of the large scale structure observed in the Universe [6]. Existence of DM in term of a new form of matter provides therefore an evidence of physics beyond the SM, and its detection would open new scenarios in fundamental physics.

However, no unequivocal Dark Matter signal have been detected to date by particle physics experiments. The most critical issue of DM search lies in the extent of the parameter space accessible to DM theories: constraints on its properties are in fact inferred from its gravitational influence on visible matter in astrophysical and cosmological contexts. Being the gravitational interaction very weak, it is impossible to reveal DM short distance properties. Indeed, without introducing additional assumptions on DM interactions with

SM particles, the viable mass window for DM particles is dauntingly large, going from $10^{-22}eV$ to $100M_{\odot}$ [7] [8].

This large range of masses can be restricted if further assumptions on the origin of the current DM abundance are made. In the most popular class of models, that predicts additional DM-SM interactions -other than gravitational interaction-, current DM survives as a relic from an era of thermodynamic equilibrium with the SM in the early universe, and its abundance was set when the interaction rate with the SM became subdominant to the expansion rate of the universe. This mechanism is known as "freeze-out" [9].

The "thermal" origin hypothesis of DM imposes that the mass should be higher than ∼10 KeV; otherwise DM would remain relativistic until late times, washing out the observed structure on small scales [10]. On the other hand, DM particles with masses above ∼10 TeV would require an annihilation rate at thermodynamic equilibrium which violates perturbative unitarity in minimal models [8]. Therefore, in this scenario, the range of viable masses of DM is restricted to 10 KeV - 10 TeV. These considerations are common to all theories assuming a thermal origin for DM, regardless of the nature of the supposed DM-SM interaction.

Despite the mass constraints the range remains considerably wide and, within the 10 KeV-GeV interval, mostly unexplored.

1.2 From WIMPs to Light Dark Matter

In the thermal origin paradigm, DM has been produced in the early universe by collisions of thermal plasma particles. The equilibrium was obtained by production and annihilation of DM pairs in particle – antiparticle collisions:

$$\chi + \bar{\chi} \longleftrightarrow SM + SM.$$

Here χ is the generic DM particle and $\bar{\chi}$ the antiparticle. In the early universe, at temperatures T much higher than the DM mass m_{DM}, the colliding SM pairs had enough energy to efficiently produce DM pairs. The annihilation reactions converting DM into SM particles were initially in equilibrium with the DM-producing processes. The rate of these processes at equilibrium is given by [9]:

$$\Gamma_{ann} = < \sigma v > n_{eq}.$$

Here σ is the DM annihilation cross-section, v is the relative velocity of the annihilating particles and n_{eq} is the density of DM particles at equilibrium. The angle bracket denote an average over the thermal distribution.

The expansion of the universe caused a progressive reduction of the temperature of the plasma, until it became lower than DM mass; as a consequence, the $SM + SM \rightarrow \chi + \bar{\chi}$ process stopped, and the number of DM particles decreased exponentially as $\sim e^{-\frac{m_{DM}}{KT}}$. Given the expansion of the universe, the number density of particles n_{eq} decreased, and with it the collision rates. When the mean free path for DM-DM collision became longer than the Hubble radius, also the $\chi+\bar{\chi} \rightarrow SM+SM$ process stopped and the DM comoving density remained approximately constant[9]. This phenomenon is known as "freeze out". In this picture, the currently observed DM abundance Ω_{DM} is bound to the annihilation rate at the time of DM-SM decoupling $< \sigma v >_{relic}$:

$$\Omega_{DM} \propto \frac{1}{< \sigma v >_{relic}}.$$

Therefore, in order to comply with the observed value $\Omega_{DM} \sim 0.3$ [11], the thermally averaged annihilation cross section must be of order $< \sigma v >_{relic} \sim 10^{-23} cm^3 s^{-1}$ [12]. This result provides a strong constraint to DM properties, reducing the mass search area. Indicated with g_{DM} the coupling that determines the intensity of the DM-DM interaction, the cross section σ times the relative particles velocity v for an annihilation process of a DM pair into two SM final states, roughly scales as $< \sigma v > \sim \frac{g_{DM}^4}{m_{DM}^2}$; consequently, fixing the order of magnitude of m_{DM} one can get an indication on the value of g_{DM}.

Historically, in the few GeV- 10 TeV DM mass range, the particle physics model landscape for DM and its interactions has been connected to the electroweak scale [10]. A particle with mass in the range of 100 GeV interacting via SM electroweak force would in fact satisfy the constraints on the value of $< \sigma v >_{relic}$. Moreover, heavy particles interacting via the weak force are predicted to be the the lightest neutral superpartner in supersymmetric extensions of the SM, introduced to address the electroweak hierarchy problem [13]. DM candidates with this properties are referred as "WIMPs" (*Weakly Interacting Massive Particles*) and the coincidence for which, in this paradigm, no additional interactions are required to yield the observed DM abundance is the so-called *WIMP miracle* [10].

Experimental efforts to detect WIMPs include *direct detection, indirect detection* and *collider production searches*. *Direct detection* experiments aim to measure the signal produced by the scattering of non-relativistic, cosmogenic WIMPs on the nuclei of large volumes of active material. Experiments belonging to this category generally employ cryogenic crystal detectors (CDMS, CRESST, Edelweiss), noble gas scintillators (LUX, XENON, DarkSide), high-purity crystal scintillators (DAMA/LIBRA) or bubble chambers [14].

Indirect detection efforts focus on the observation of signals from locations where high

density of WIMPs is thought to accumulate: in the centers of galaxies and galaxy clusters, as well as in the smaller satellite galaxies of the Milky Way. A typical signal of WIMPs is an excess of gamma rays, which are predicted both as final products of DM annihilation, or are produced as charged particles interact with ambient radiation via inverse Compton scattering. Through the non-observation of an annihilation signal, the Fermi-LAT gamma ray telescope has recently placed bounds on theWIMP annihilation rate [15].

Finally, heavy DM can also be tested at high energy accelerators as Large Hadron Collider (LHC), studying events with missing (transverse) energy in association with visible SM states [16] [17].

The rich variety of experimental techniques used to search for WIMPs allowed to explore DM range between few GeV to 10 TeV. However, null results from direct detection experiments including LUX [18], CDMS II [19] and XENON [20], along with the failure to produce evidence of super-symmetry in the LHC experiment has cast doubt on the WIMP hypothesis. The interest towards other DM candidates is therefore growing.

The MeV-GeV DM mass range is fairly unexplored when compared to the experimental efforts towards WIMPs detection. This is also due to the fact that the experimental strategies employed to probe WIMP theories became highly ineffective in the detection of Light DM (LDM). *Direct detection* experiments typically require that an energy $E \geq$ KeV scale is released in the detector through the scattering of a DM particle on a nuclear target. For such a two-body elastic scattering process, the nucleus recoil energy scales as $E \sim \mu v^2$; $\mu = \frac{m_N m_{DM}}{m_N + m_{DM}}$ is the nucleus-DM reduced mass and $v = 10^{-3}c$ is the relative velocity of the pair in the lab frame. For DM particles with mass $m_{DM} \leq 1$ GeV the recoil energy becomes too small to be detected by this class of experiments. The indirect detection strategy too presents difficulties when applied to the search of LDM: the products of annihilation of sub-GeV particles would have energies in the range of complicated and poorly understood astrophysical backgrounds, which would make hard to distinguish a potential DM signal. LDM could be studied at collider experiments, with a signature of a missing energy in conjunction with other visible final states; still its low mass implies a weak recoil against the visible particles and, as a result, a hardly distinguishable signal from SM backgrounds.

In conclusion, it is clear that LDM search requires the development of new ad hoc experiments. In fact, despite the ongoing effort to extend the sensitivity of "traditional" DM detection to low masses, techniques employed for WIMPs detection are still not efficient to search for LDM in the 1-100 MeV mass range.

1.3 New "Dark" Mediators

As discussed in previous section, a key point of the WIMP paradigm is the possibility to explain current DM abundance without introducing new interactions between *Dark Sectors* and SM. This feature derives from an appropriate choice of the WIMP mass range and therefore cannot be extended to LDM models. If we try to estimate the annihilation rate for a *Dark Sector* χ particle in the MeV-GeV range via the weak process:

$$\chi + \bar{\chi} \rightarrow Z^* \rightarrow SM + SM,$$

we obtain the scaling: $< \sigma v > \sim G_F^2 m_\chi^2 \sim \times 10^{-27} cm^3 s^{-1} (\frac{m_\chi}{100 MeV})^2$. This rate is insufficient to account for an efficient DM annihilation rate in the early universe. Consequently, to comply with the present DM abundance in the framework of thermal LDM, it is necessary to postulate a new interaction between SM and the *Dark Sector*, mediated by a new force carrier. This carrier, as well as the DM particles, has to be neutral under the SM gauge group[1].

From a theoretical point of view, the relevant DM-SM interaction can be obtained through the so called "renormalizable portals", i.e. interactions consisting of SM gauge singlet operators with mass dimension < 4 [21],

$$\hat{O}_{portal} = H^\dagger H; \quad LH; \quad B_{\mu\nu},$$

and a new SM-neutral degree of freedom, which can be a scalar ϕ, a fermion N, or a vector A'. Here H is the SM Higgs doublet, L is a lepton doublet of any generation and $B_{\mu\nu} = \partial_\mu B_\nu - \partial_\nu B_\mu$ is the hypercharge field strength tensor.

The three different option (scalar, vector or fermionic mediator) lead to three different scenarios; however, as we shall see, scalar and fermionic mediators can be ruled out by different considerations. Thus, we will focus our attention on the theory of a new vector mediated interaction.

1.4 Excluding Fermion And Scalar Portal

If the SM-DM mediator is a fermion N, its interaction proceeds through the *neutrino* portal [21] which consists in the coupling of a set of singlet fermions N_j to the LH composite fermionic operator of the SM, resulting in the neutrino Yukawa interaction:

$$L_{int} = y_{ij} L_i H N_j,$$

[1] Otherwise it would have been discovered in direct searches in previous experiments (e.g. LEP)

here i, j are flavour indices. In this picture N plays the role of a right-handed neutrino and could be itself a viable cosmologically metastable DM candidate in a narrow mass range. Nevertheless, being N supposed with mass in the MeV-GeV range (LDM range), Yukawa couplings of order $y_{ij} \sim 10^{-12}$ are required in order to obtain the observed neutrino masses. Since this value is way too weak to allow DM thermalization at early times, fermion portal option is less motivated in the thermal DM scenario [22].

If, instead, the mediator is a scalar ϕ the only admitted interactions are through the Higgs portal:

$$\phi HH, \quad \phi^2 HH.$$

These operators induce a mixing between the mass of the ϕ and the SM Higgs boson, which causes the ϕ to interact with the SM fermions with a coupling proportional to their masses [23].

If we suppose a fermionic DM candidate χ, the lagrangian for scalar mediator LDM is:

$$\mathscr{L} \supset g_D \phi \bar{\chi}\chi + \frac{m_\phi^2}{2}\phi^2 + AH^\dagger H\phi + \frac{m_f}{v} H \bar{f_L} f_R + h.c.$$

Here g_D is the coupling of the new force, A is a constant with dimensions of a mass, f is a SM fermion with mass m_f and v is the Higgs vacuum expectation value. After electroweak symmetry breaking, diagonalizing the scalar mass terms induces a mixing between ϕ and the neutral component of the Higgs doublet [23]. In the mass eigenbasis, this mixing leads to a coupling between DM mediator and SM fermions:

$$\mathscr{L}_{\phi,f} = \phi \sin\theta \frac{m_f}{v} \bar{f} f = g_f \phi \bar{f} f.$$

Here θ is the $\phi - H$ mixing angle. In this picture the thermal relic DM density is achieved through different mechanisms depending on the value of the rate $\frac{m_\chi}{m_\phi}$.

If $m_\chi < m_\phi$, DM annihilation can only proceed via direct-annihilation to SM fermions through the process:

$$\chi\bar{\chi} \longrightarrow \phi^* \longrightarrow f\bar{f},$$

with an annihilation rate scales roughly as:

$$\sigma v(\chi\bar{\chi} \to f\bar{f}) \propto g_D \sin\theta \left(\frac{m_f}{v}\right)^2 \left(\frac{m_\chi}{m_\phi}\right)^4.$$

Since in thermal LDM paradigm annihilation to light SM fermions ($m_f \ll v$) is required, the mixing angle θ must satisfy $\sin\theta \sim \mathscr{O}(1)$ over most of the $m_\chi < GeV$ range [23]. This value of θ would lead to a large branching ratio for the process $B \to K\phi$, which contributes to the $B^+ \to K^+\bar{\nu}\nu$ and $K^+ \to \pi^+\bar{\nu}\nu$ observables. However, the observed ratios for these

processes are in complete disagreement with those predicted by this model; therefore the hypothesis of a scalar DM mediator ϕ with mass $m_\phi > m_\chi$ could be discarded [23].

If, instead, $m_\chi > m_\phi$, DM annihilation is still viable through the $\chi\chi \to \phi\phi$ channel, defined as the *secluded annihilation* channel. However, secluded annihilation rate does not depend on the value of ε, therefore arbitrary small values of the coupling are compatible with thermal origin. Consequently, this scenario is not suitable for experimental exploration, although theoretically motivated [23].

1.5 Vector Mediated Models

The vector portal, where a new vector boson (*Dark Photon, Heavy Photon* or A') acts as mediator of a new "dark" force and couples with the SM hypercharge, is compatible with the thermal origin hypothesis and, to date, largely unexplored for the LDM parameters.

Let A' be a spin 1 boson; in the simplest picture its coupling with the SM is given by the *kinetic mixing* interaction [24]:

$$\mathscr{L}_{Kin.Mix.} = \frac{1}{2}\varepsilon_Y B_{\mu\nu} F'^{\mu\nu}.$$

Here ε_Y is a dimensionless coupling constant, $B_{\mu\nu} = \partial_\mu B_\nu - \partial_\nu B_\mu$ is the hypercharge field strength and $F'_{\mu\nu} = \partial_\mu A'_\nu - \partial_\mu A'_\nu$ is the *Dark Photon* field strength. In this scenario, the A' acts as the gauge boson from a spontaneously broken $U(1)_D$ symmetry, and DM is charged under this gauge group. The Lagrangian describing this setup is:

$$\mathscr{L}_{A'} \supset -\frac{1}{4}F'_{\mu\nu}F'^{\mu\nu} + \frac{1}{2}\varepsilon_Y B_{\mu\nu}F'^{\mu\nu} + \frac{1}{2}m_{A'}A'_\mu A'^\mu + g_D A'_\mu J^\mu_\chi + g_Y B_\mu J^\mu_Y, \tag{1.1}$$

where we introduced the mass of the *Dark Photon* $m_{A'}$, the dark gauge coupling $g_D = \sqrt{4\pi\alpha_D}$ and the DM and SM hypercharge currents J^μ_χ and J^μ_Y. After electroweak symmetry breaking, the kinetic mixing term of the Lagrangian induces the coupling of the A' with the SM photon and the Z boson:

$$\mathscr{L}_{Kin.Mix.} \longrightarrow \frac{1}{2}\varepsilon F'_{\mu\nu}F^{\mu\nu} + \frac{1}{2}\varepsilon_Z F'_{\mu\nu}Z^{\mu\nu},$$

where $\varepsilon = \varepsilon_Y \cos\theta_W$, $\varepsilon_Z = \varepsilon_Y \sin\theta_W$ and θ_W is the weak mixing angle. This leads to the *Dark Photon* interaction with SM and DM:

$$g_D A'_\mu J^\mu_\chi + g_Y B_\mu J^\mu_Y \longrightarrow A'_\mu \left(g_D J^\mu_\chi + \varepsilon e J^\mu_{EM}\right),$$

being J^μ_{EM} the usual SM electromagnetic current and having omitted higher order terms in ε. Here, SM fermions acquire an effective electromagnetic "millicharge" under the short-range force carried by the A', namely $e\varepsilon$.

The phenomenology in the LDM sector will depend on how DM couples to A', i.e. what is the dark current J^{μ}_{χ}. No assumption has been in fact made until now on the DM particles χ. For instance, DM could be a priori a spin $\frac{1}{2}$ fermion as well as a spinless boson. However, as for the scalar portal, a general distinction based on the value of the rate $\frac{m_{A'}}{m_{\chi}}$ can be made regardless of the DM nature. Depending on whether the mass of the A' is greater or smaller than the mass of the χ, relic DM density is achieved through different annihilation mechanisms [25]:

- If $m_{\chi} > m_{A'}$ the relevant DM annihilation process is "secluded":

  $$\chi\bar{\chi} \longrightarrow A'A'.$$

  For this process, the rate scales as:

  $$< \sigma v > \sim \frac{g_D^4}{m_{\chi}^4}.$$

  Since this rate does not depend on the SM-mediator coupling ε, arbitrarily small values of ε can be compatible with thermal LDM in this regime. Therefore, the secluded scenario does not lend itself to decisive laboratory tests.

- If $m_{\chi} < m_{A'}$ the relevant process is "direct" annihilation:

  $$\chi\bar{\chi} \longrightarrow A'^{*} \longrightarrow SM \quad SM,$$

  whose rate scales as:

  $$< \sigma v > \sim \frac{\varepsilon^2 g_D^2 m_{\chi}^2}{m_{A'}^4}.$$

  This scenario offers a predictive target for discovery or falsifiability since the dark coupling g_D and mass ratio $\frac{m_{\chi}}{m_{A'}}$ are at most $\mathcal{O}(1)$ in this regime, so there is a minimum value of ε compatible with a thermal history (smaller values of g_D require nonperturbative dynamics in the A'-SM coupling or intricate model building).

From now on we will focus our attention on the latter predictive regime, whose exploration is the goal of the Beam Dump Experiment [26]. In the case of direct annihilation, the minimum annihilation rate requirement for thermal origin translates into a minimum value of the thermal target y:

$$y = \frac{\varepsilon^2 g_D^2}{4\pi} \left(\frac{m_{\chi}}{m_{A'}} \right)^4 \simeq < \sigma v >_{relic} m_{\chi}^2.$$

This constraint is valid for every DM variation, provided that $m_{\chi} < m_{A'}$. The precise value of y depends on the choice of LDM candidate. This model is compatible with a finite set of LDM candidates which can be either fermions or scalars, cosmologically particle-antiparticle symmetric or asymmetric, and may couple elastically or inelastically to the A'. In the following section I briefly describe the main characteristics of these LDM variations.

1.6 Relevant LDM Variations With a Vector Mediator

Symmetric Fermion LDM: If the LDM candidate χ is a symmetric fermion, the coupling with the A' is given by the term:

$$g_D A' \bar{\chi} \gamma^\mu \chi.$$

In this scenario, the LDM particles abundance is symmetric with respect to particles and antiparticles, so the annihilation rate must satisfy $\langle \sigma v \rangle \sim 3 \times 10^{-26}\ cm^2 s^{-1}$ to achieve the observed relic abundance. For Dirac fermions, the annihilation cross section proceed via s-wave:

$$< \sigma v >_{relic} \quad \propto \quad \varepsilon^2 \alpha_D \frac{m_\chi^2}{m_{A'}^4} = \frac{y}{m_\chi^2},$$

and was therefore constant throughout cosmic evolution, including during the epoch of the CMB near $kT \sim eV$. Although the DM abundance has frozen out by this point, out-of-equilibrium annihilation to SM particles would have re-ionize hydrogen leaving an imprint in the SM ionized fraction [27]. For a particle-antiparticle symmetric population of χ, this scenario is completely ruled out by measurements of the CMB power spectrum [28].

Asymmetric Fermion LDM: Assuming that the cosmic abundance of Dirac fermion χ is set by a primordial asymmetry, then the annihilation process depletes antiparticles during the CMB epoch so their effective abundance of antiparticles is suppressed by factors $\sim e^{-\sigma v}$. Thus, the CMB re-ionization bound does not rule out this scenario [29].

Majorana (Pseudo-Dirac) LDM: The fact that the A' has a non-zero mass means that the $U(1)_D$ in the *Dark Sector* is a broken gauge theory [30]. A generic possibility is that the LDM candidate is a fermion with both a $U(1)_D$ preserving Dirac mass and a $U(1)_D$ breaking Majorana mass which may be induced by the mechanism responsible for spontaneous symmetry breaking in the *Dark Sector*. This would result in a mass splitting of the Weyl spinors χ. Consequently, the *Dark Photon* couples predominantly to the off-diagonal current:

$$J_\chi^\mu = \bar{\chi_1} \gamma^\mu \chi_2 + h.c.,$$

where χ_1 an χ_2 are Majorana spinors with mass splitting: $m_1 - m_2 = \Delta$; all interactions with the A' are off-diagonal in this mass eigenbasis.

In this picture the direct annihilation requires both eigenstates to meet via $\chi_1 \chi_2 \rightarrow A'^* \rightarrow SM$, so at late cosmological times (when the temperature T of the plasma satisfies

$T \ll \Delta$) this process shuts out. For $\Delta \ll m_\chi$ the annihilation rate has the same scaling as the Dirac fermion case:

$$< \sigma v > \propto \varepsilon^2 \alpha_D \frac{m_\chi^2}{m_{A'}^4} \simeq \frac{y}{m_\chi^2} + \mathscr{O}\left(\frac{\Delta}{m_\chi}\right),$$

so the same y target applies. However the CMB bound that rules out the symmetric fermion scenario is here removed: at late time the excited state χ_2 is in fact typically absent, thus shutting of the annihilation $\chi_1\chi_2 \to A'^* \to SM$. The hypothesis of Majorana LDM is therefore viable; its worth noting that this setup falls within the popular class of models known as "inelastic DM" [31].

Scalar LDM Finally we consider the possibility that the LDM candidates is a complex scalar; in this case the DM current is:

$$J_\chi^\mu = i\left(\chi^* \partial^\mu \chi - \chi \partial^\mu \chi^*\right).$$

Due to the momentum dependence in the coupling to the A', the annihilation $\chi\chi^* \to A^* \to SM$ is p wave:

$$< \sigma v > \propto \varepsilon^2 \alpha_D \frac{m_\chi^2 v^2}{m_{A'}^4} \sim \frac{y v^2}{m_\chi^2},$$

where v is the velocity. The dependence of the annihilation rate from the velocity lead to a $\mathscr{O}(10)$ larger target y if compared to the fermion scenario, for fixed m_χ. In fact, being the DM freeze-out temperature $T_f \simeq \frac{m_\chi}{20}$, the χ velocity at freeze out must be of order $v^2 \sim 0.1$ [32].

In conclusion, the vector portal gives a viable scenario for LDM with a thermal origin. Moreover, contrary to scalar and fermion portal, different variations of LDM candidates offer clear thermal targets which can be experimentally explored. This is indeed the scenario targeted by the Beam Dump Experiment (BDX) and serves as a basis for defining its sensitivity.

1.7 Dark Photon Signatures

Within the "direct annihilation" scenario targeted by BDX, the *Dark Photon* experimental signature depends on the $\frac{m_{A'}}{m_\chi}$ ratio. If no χ particles lighter than $\frac{m_{A'}}{2}$ exists in the *Dark Sector*, on-shell A's can only decay to SM particles, e.g. a e^+e^- or a $\mu^+\mu-$ pair. In this scenario, called **visible decay** since the A' decay products are detectable SM particles,

the *Dark Photon* lifetime T scales as $T \propto \varepsilon^{-2}$. Otherwise, if $m_{A'} > 2m_\chi$, *Dark Photon* decays predominantly to a $\chi\bar{\chi}$ pair (**invisible decay**), since α_D, the coupling between the A' and the *Dark Sector*, can be large ($O(1)$) while ε has to be small. In this scenario, the lifetime T of the dark photon does not depend on the coupling ε and, from an experimental point of view, the $A' \to \bar{\chi}\chi$ decay is considered to be instantanous.

Beam-dump experiments such as BDX are sensitive to both scenarios, since they can produce χ particles via a radiative process via both on-shell or off-shell *Dark Photons* (see Sec. 2.1.1). However, BDX has been optimized to search for LDM in the invisible decay pictures, and therefore from now on we will focus our attention on this regime.

1.8 Overview of LDM experimental searches

As noted in Sec 1.2, in the last years the interest in the search for the *Dark Photon* has grown considerably, leading to a significant experimental activity. The parameter space of vector-mediated LDM is characterized by the *Dark Photon* and LDM masses ($m_{A'}$ and m_χ), the coupling α_D of the A' to the LDM particle χ and the kinetic mixing represented by ε. Part of this space has already been ruled out by various experiments, but large regions are still open, as shown in Fig. 1.1. The goal of the BDX experiment is to explore them. In this section I briefly discuss the most relevant past, current and future searches probing the LDM paradigm (for a more complete overview, see [25] and [33]).

B-Factories: Mono-photon and missing-energy production at B-factories set a limit on models of LDM. The BaBar search for a $\Upsilon(3S) \to \gamma +$ invisible [34] constrains the process $e^+e^- \to \gamma + A'^* \to \gamma\chi\chi$ [35] [36] [37]. Since the A' production rate only depends on ε and the beam energy, the BaBar results do not directly translate to limits for the y variable. To cast BaBar limits on ε^2 and $m_{A'}$ in the $y - m_\chi$ parameter space, a specific choice on α_D and the value of the ratio $\frac{m_\chi}{m_{A'}}$ must be fixed.

High Energy Colliders: Since kinetic mixing induces a shift in the mass of the Z_0 boson, electroweak precision tests at LEP can constrain the existence of the A'. This constraint depends on ε and only mildly on $m_{A'}$ [38][39]. At the LHC, LDM can be produced in association with a QCD jet, thus appearing as a missing-energy event (with a significant transverse component). The study of this channel places a constraint on the y vs. m_χ plane; these constraints do not scale with y so one must fix the value of $\frac{m_\chi}{m_{A'}}$ and α_D in constructing y for colliders [25].

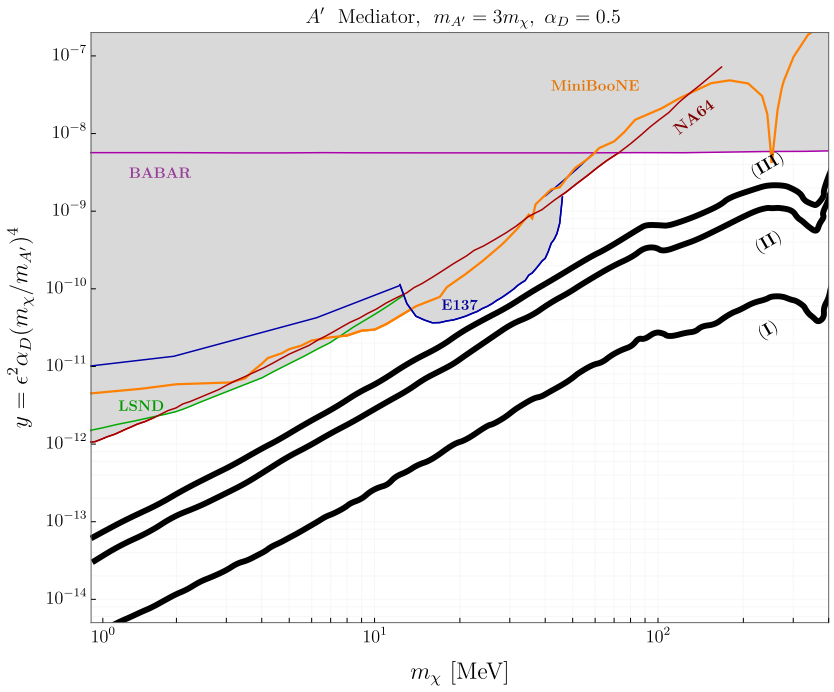

Figure 1.1: Example of the viable parameter space for light dark matter (for $\alpha_D = 0.5$ and $m_{A'} = 3m_\chi$) in the representative kinetically-mixed scenario alongside appropriate constraints. The "y" variable on the vertical axis is chosen because it is proportional to the annihilation rate, so the thermal target is fixed for a given choice of m_χ. The three continuous black lines represent the thermal relic target for different hypothesis on the LDM nature: elastic and inelastic scalar (I), Majorana fermion (II), and pseudo-Dirac fermion (III).

Visible Decay: Many experiments searching for resonances of the $Mediator \to SM + SM$ channel (see previous section) have been performed. These searches can target LDM models in the regime $m_{DM} < m_{A'} < m_e$ or whenever $\varepsilon \gg g_D$. Several different complementary approaches were proposed (for a summary, see [40]).

Missing Energy Experiments: This class of experiments aims to reconstruct a LDM signal from missing energy in the process of secluded annihilation of the A'. The PADME experiment, currently ongoing at Frascati [41], uses a positron beam impinging on a thin target to search for missing energy in the channel:

$$e^+e^- \to \gamma(A' \to \chi\chi),$$

This experiment aims to reconstruct the missing mass $M^2_{MISS} = (P_{e-} + P_{beam} - P_\gamma)^2$, measuring the momentum of the outgoing photon P_γ. Similar efforts have been proposed at Cornell [42].

Another missing energy experiment NA64, currently running at CERN SPS, is sensitive to invisible A' decay in the channel:

$$eZ \to eZ(A' \to \chi\chi).$$

NA64 has performed a first measurement in 2016, collecting a total of $\sim 4.3\times10^{10}$ electrons on target, and significantly more data were taken in 2017 and 2018 [43]. The projected sensitivity of NA64 makes this experiment one of BDX direct competitors for search of LDM with diagonal couplings to the *Dark Photon*.

Missing Momentum Experiments In this class of experiments the LDM is produced in the fixed-target reaction $e^-Z \to eZ(A' \to \bar{\chi}\chi)$ and identified through the missing momentum carried away by the unobserved DM particles. These searches rely on the detector hermeticity to achieve excellent background rejection, a critical aspect. LDMX, currently in development stage [44] is a promising example of missing momentum experiment. LDMX will make use of a tracker and an hermetic calorimeter to reconstruct the missing momentum in the process of secluded annihilation of the A's produced in a thin target by a multi-GeV electron beam.

Direct Detection Experiments: Elastic LDM-nuclear interactions are constrained by recent results from CRESST-III [45], whose low threshold allows for sensitivity down to a few 100s of MeV in DM mass. New ideas for detection of DM through the scattering on electrons have been recently proposed to overcome the sensitivity limits of tra-

ditional direct detection experiments (see Section 1.2). Even if these searches are currently background-limited ([46][47]), new techniques have the potential to also target the thermally-motivated parameter space of light DM. However, for Majorana LDM, the sensitivity of direct detection experiments is still quite limited.

Beam Dump Experiments: Experiments of this category, to which BDX belongs, aim to produce *Dark Photons* through the collision of an intense beam of SM charged particles on a thick target (the dump). The LDM particles produced by the decay of the $A's$ travel up to a detector placed downstream the dump, where they can be interact and be detected.

The considerable sensitivity of beam-dump experiments to light dark matter is underscored by the reinterpretation of previous neutrino experiments [48], [49], [50], [51]. For example, LSND measurement of meson production and decay [52] can be used to derive the most stringent constraints to date on the parameter space for invisibly-decaying dark mediators that couple to both baryons and leptons [49]. That experiment delivered $\sim 10^{23}$ 800 MeV protons to the LANSCE beam-dump.

As far as running experiments are concerned, the MiniBooNE experiment at Fermilab, originally designed to study neutrino oscillations, recently completed a measurement run searching for ∼MeV mass DM [53]. In the experiment, the 8.9 GeV proton beam from the FNAL accelerator impinges on a 50-m long iron beam-dump. Dark matter particles are produced through neutral mesons decay (π_0, η), where one of the photons converts to an A' that, in turns, decays to a $\bar{\chi}\chi$ pair. Given the large charge collected, limits set by MiniBooNE on the invisibly decaying *Dark Photon* scenario are comparable to LSND constraints.

Unlike MiniBooNE, BDX at JLab will use an electron beam to produce DM particles. As to proton beam-dump experiments, electron beam-dump experiments (such as E137 at SLAC) offer comparable signal yields and do not suffer from the same level of neutrino background. In particular, BDX could improve the sensitivity over LSND for LDM masses above the $\frac{m_{\pi_0}}{2}$ threshold.

An accurate description of the plan of the Beam Dump Experiment is provided in the next Section, with particular attention to the experimental setup, LDM production and detection mechanisms and to the expected background.

Chapter 2

BDX: the Beam Dump eXperiment

BDX is an approved experiment at Jefferson Lab aiming to produce and detect Light Dark Matter (LDM) particles expected in vector-mediated LDM theoretical models [26]. BDX makes use of CEBAF (Continuous Electron Beam Accelerator Facility) 11 GeV electron beam impinging on the JLab Hall-A beam-dump, which is enclosed in a concrete tunnel at the end of the beam transport line. The interaction between the energetic electrons and the atoms of the dump leads to the production of Dark Matter through different processes discussed in the following section. Subsequently, the A' decays to LDM particle-antiparticle pairs ($\chi\bar{\chi}$), which travel almost unaltered through the length of the dump. A $\sim 1\ m^3$ active volume detector composed of CsI(Tl) (Thallium doped Cesium Iodide) crystals is located in the trajectory of the LDM beam, $\sim$ 20 m downstream of the Hall-

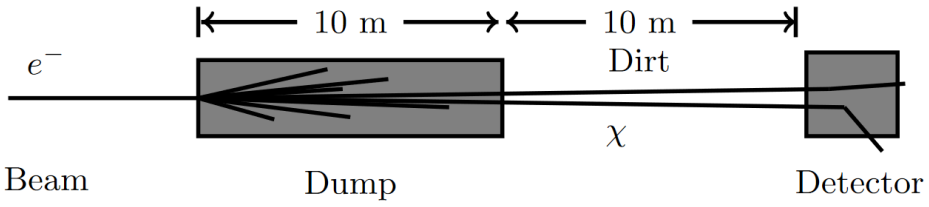

Figure 2.1: Schematic of experimental setup. The CEBAF multi-GeV electron beam produces a secondary beam of *Dark Sector* particles impinging on the beam-dump. In the optimal setup, the detector is placed $\sim$ 20 m downstream with respect to the dump, at such a distance that muons and energetic neutrons are ranged out.

A beam-dump. A small fraction of the LDM particles may scatter off electrons in the detector giving rise to an electromagnetic shower of order $\sim$ 100 MeV (see Fig. 2.1).

The expected low signal rate (due to the weakness of the mixing between the SM photon and the A') makes the background rejection a critical issue for BDX. To range out all SM beam products except neutrinos, the distance between the dump and the detector is filled with passive shielding; to reduce beam-unrelated background, mainly due to cosmic neutrons and muons, the BDX detector features an active veto and passive shielding surrounding the CsI(Tl) electromagnetic calorimeter. Thanks to the cosmic background suppression capability and the high intensity of the CEBAF electron beam (up to $\sim$ 65 μA at 11 GeV), BDX will be able, with a $\sim$ 280 days run, to exceed by up to two orders of magnitude the sensitivity of current competitor experiments. In the following sections, details of the BDX experimental setup are reported, as well as the χs production and detection mechanisms. Finally, the evaluation of the expected background yield is reported.

2.1 LDM Production And Interaction

Whether the *Dark Sector* is quite simple or has a rich structure of light particles, the fixed-target phenomenology of stable χs (or unstable χs with lab-frame lifetimes $> \mu s$) is well-described by the simplest case — the Lagrangian 1.1. Here the label χ could refer to scalar or fermion LDM, with diagonal or off-diagonal couplings to the A'. In this theoretical scenario, an electron beam-dump experiment such as BDX can produce χs through different processes, given the large number of SM energetic particles produced in the dump by the primary electron beam. The χs can then scatter off nucleons or electrons in the detector volume. The evaluation of the expected signal rate, accounting for the different χ production mechanisms, was performed through a multi-step numerical calculation; a detailed description of this study is provided in Ch. 4 and 5. Here a brief description of the χs production and interaction mechanisms which contribute to the BDX sensitivity is provided. For a more thorough review of the thick-target χ fenomenology, see [26] and [4].

2.1.1 LDM Production

An energetic electron beam impinging on a thick target such as a beam-dump gives rise to an electromagnetic shower consisting of a large number of Standard Model particles, i.e. electrons, positrons, photons, muons (to a lesser extent), etc. In the *Dark Photon* scenario, the interaction of SM particles in the dump can produce χs through different

processes; here I describe the most relevant ones for the sake of BDX.

A'-strahlung: A's can be produced through a radiative process as energetic electrons (or positrons) interact with Al nuclei in the dump (see Fig. 2.2) . The secondary χ beam arises from the decay of on-shell or off-shell A's , depending on the rate of the masses m_χ and $m_{A'}$.

- if $m_\chi < m_{A'} < 2m_\chi$, the χs are produced via an A'-strahlung process with an off-shell A'. In this regime, the χ production yield depends on the model parameters as $\sim \frac{\alpha^3 \alpha_D \varepsilon^2}{m_\chi^2}$, where α is the electromagnetic fine-structure constant.
- if $m'_A > 2m_\chi$ χs arise from radiative A' on-shell production, followed by the $A' \to \chi\bar{\chi}$ decay. In this regime, the χs production scales as $\sim \frac{\alpha^3 \varepsilon^2}{m'_A}$.

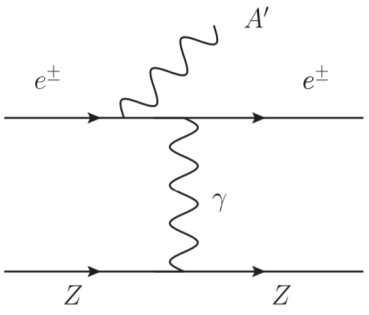

Figure 2.2: A' production in electron-nucleus collisions via radiative process.

In both cases, the A' energy distribution is peaked at the energy of the primary electron and the A' angle relative to the beam line is peaked forward [35]. The χs emission angle is therefore dominated by the opening angle of the $A' \to \chi\bar{\chi}$ decay. This description is valid whether χ refers to scalar or fermion LDM. The DM production mechanism is analogous to the one expected in the equally-motivated paradigm of Majorana LDM with off-diagonal couplings.

Secondary positrons annihilation: As mentioned above, the interaction of the primary electron beam in a thick-target initiates an electromagnetic shower, resulting in the production of a large number of secondary particles, among which positrons. These particles can annihilate with electrons in the beam-dump, producing an A' via a resonant ($e^+e^- \to A'$) or non-resonant ($e^+e^- \to A'\gamma$) process, as shown in Fig. 2.3. The cross section for these processes scales as $\varepsilon^2\alpha$ and $\varepsilon^2\alpha^2$ respectively, compared to the $\varepsilon^2\alpha^3$ scaling of the A'-strahlung diagram. The production of A's through positron annihilation is usually neglected in the evaluation of the sensitivity of electron beam-dump experiments searching for LDM. However, in a recent study [4] I proved that, given the more advantageous cross-section dependence on α, the annihilation processes (the resonant one in particular) are competitive with A'-strahlung for certain regions of the LDM parameter

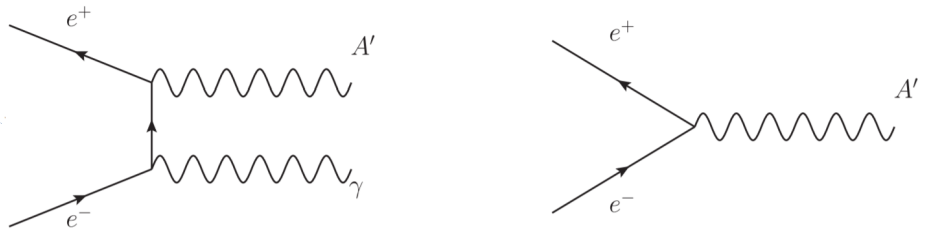

Figure 2.3: A' production via non-resonant (left) and resonant (right) positron annihilation.

space, in the $m_{A'} > 2m_\chi$ hypothesis. The cross section for the resonant diagram is given by [3]:

$$\sigma_r = \sigma_{peak} \frac{\Gamma_{A'}^2/4}{(\sqrt{s} - m_{A'})^2 + \Gamma_{A'}^2/4},$$

where s is the e^+e^- invariant mass squared, $\sigma_{peak} = \frac{12\pi}{m_{A'}^2}$ is the resonant cross section at the peak and $\Gamma_{A'} = \frac{1}{3} m_{A'} \varepsilon^2 \alpha_D$ is the A' decay width in the limit $\frac{m_e}{m_{A'}} \to 0$. The total cross section for the non-resonant diagram is:

$$\sigma_{nr} = \frac{8\pi\alpha^2\varepsilon^2}{s} \left[\left(\frac{s - m_{A'}^2}{2s} + \frac{m_{A'}^2}{s - m_{A'}^2} \right) \log \frac{s}{m_e^2} - \frac{s - m_{A'}^2}{2s} \right],$$

with m_e being the electron mass.

The main kinematic characteristics of the two annihilation mechanisms are as follows. In the case of resonant positron annihilation, the kinematics of the produced A' is strongly constrained by the one-body nature of the final state: a *Dark Photon* with mass $m_{A'}$ is produced with energy $E_R = \frac{m_{A'}^2}{2m_e}$, in the same direction of the impinging positron. For the non-resonant case, instead, the angular distribution in the CM frame is concentrated in the e^+e^- direction. This results in an angular distribution in the laboratory frame strongly peaked in the forward direction, the effect being more intense for large values of $m_{A'}$. The A' energy distribution ranges from E_R to the primary positron energy E_0, with an average value of $\frac{E_0}{2}\left(1 + \frac{m_{A'}^2}{2m_e E_0}\right)$ [3].

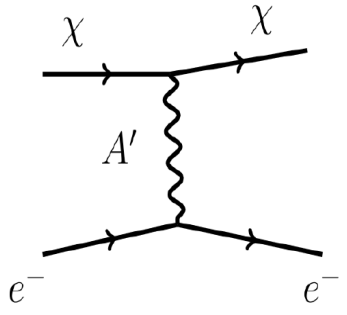

Figure 2.4: χ scattering off an electron in the detector.

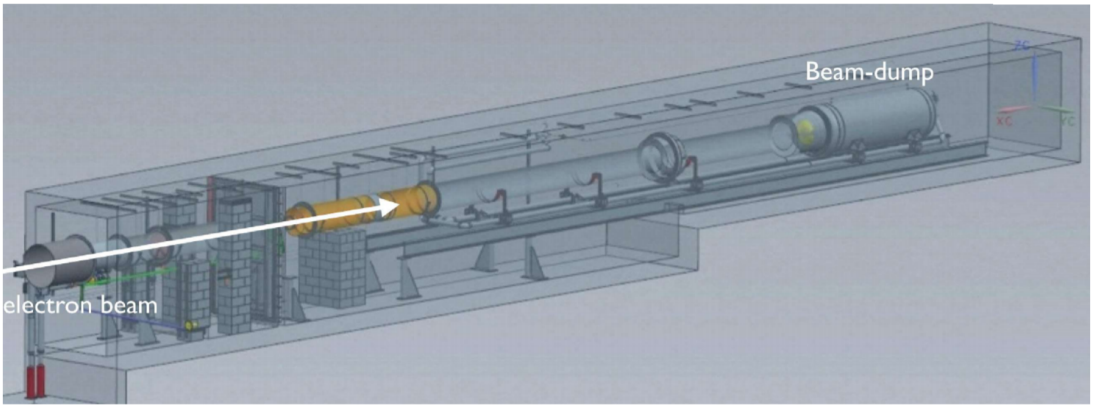

Figure 2.5: The Hall-A beam-dump enclosure in the concreate tunnel.

2.1.2 LDM Interaction

If the χ couples diagonally with the A', the interaction with the atoms of the detector occurs through two main different processes: elastic scattering off electrons (see Fig. 2.4) or quasi-elastic scattering off nucleons, via the exchange of an A'. The interaction cross section depends on the model parameters as follows: $\sigma_{int} \propto \alpha_D \varepsilon^2 / m_{A'}^2$. In the electron case, since $m_e \ll m_\chi$, the scattered electrons typically carries most of the impinging χ energy and gives rise to an electromagnetic shower in the calorimeter. In the nucleon case, due to the much higher mass of the nucleons, the recoil energy would be of the order of $\sim$ MeV. The signal corresponding to this process is therefore much more difficult to identify, due to high background of cosmogenic particles (see Sec. 2.3), which are expected to limit the sensitivity of this channel. For this reason, the sensitivity of BDX has been evaluated considering only the electron channel. However, the experimental detection of the low-energy scattered nucleons remains a secondary goal of the experiment, providing an alternative probe for LDM.

2.2 Experimental Setup

2.2.1 Hall-A Beam-Dump and BDX Experimental Hall

As mentioned above, the Hall-A at JLab is expected to receive from CEBAF a 11 GeV electron beam with a maximum current of about 65 μA. The large power of the beam is dissipated in the Hall-A beam-dump, enclosed in a concrete tunnel at the end of the beam transport line. Figure 2.5 shows a rendering of the dump and the last fraction of the beam line. The dump is made by a set of about 80 aluminum disks, each approximately 40 cm

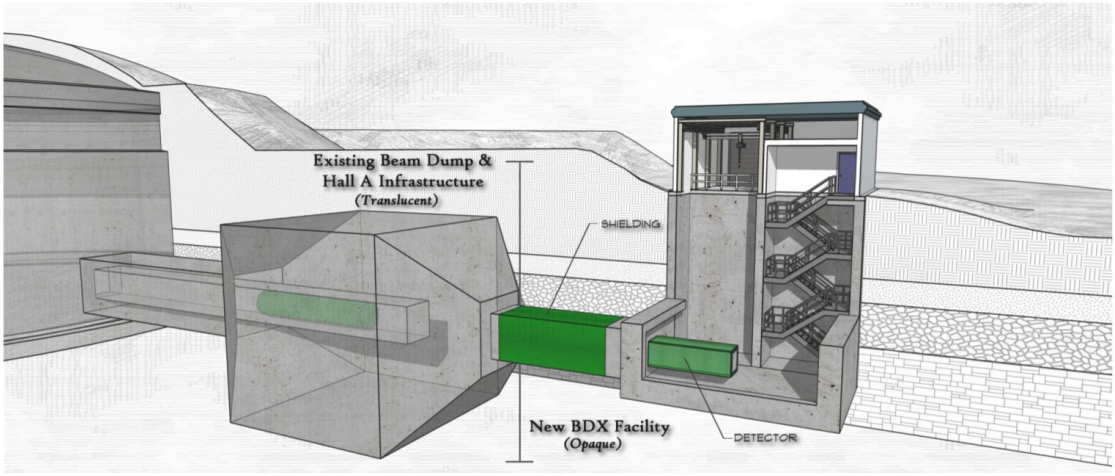

Figure 2.6: Artist's conception of the BDX facility. The drawing shows the existing Hall A beam-dump surrounded by a concrete bunker. The new BDX facility will include a staging building on the surface, additional shielding downstream of the Hall A beam-dump, an underground area for the detectors, and stair and shaft access to the surface.

in diameter of increasing thickness (from 1 to 2 cm), for a total length of approximately 200 cm, followed by a solid Al cylinder 50 cm in diameter and approximately 100 cm long. Both disks and the cylinder are cooled by circulating water. To increase the radiation shielding, the thickness of the concrete tunnel surrounding the Al dump is about 4-5 m thick.

The BDX detector will be placed in a new facility located at the beam height ($\sim$ 8 m below ground-level), 20 m downstream the beam-dump. The new experimental hall, depicted in Fig. 2.6, will feature a $O(5\ m)$ thick concrete overburden to reduce cosmic background; iron blocks will be placed between the exisiting beam-dump bunker and the BDX facility, allowing to range out most of the SM particles produced by the beam interaction in the dump.

2.2.2 BDX Detector

The BDX detector is made by two main components: an electromagnetic calorimeter (Ecal) made of a matrix of inorganic scintillating crystals, used to detect signals, and a veto detector, used to reduce backgrounds (see Fig. 2.7 for a sketch of the detector). A DM event in BDX is characterized by the presence of an electromagnetic shower in the Ecal ($E > 350$ MeV) paired with null activity in the surrounding veto system. The veto detector consists of two layers of plastic scintillators, named Inner (IV) and Outer Veto

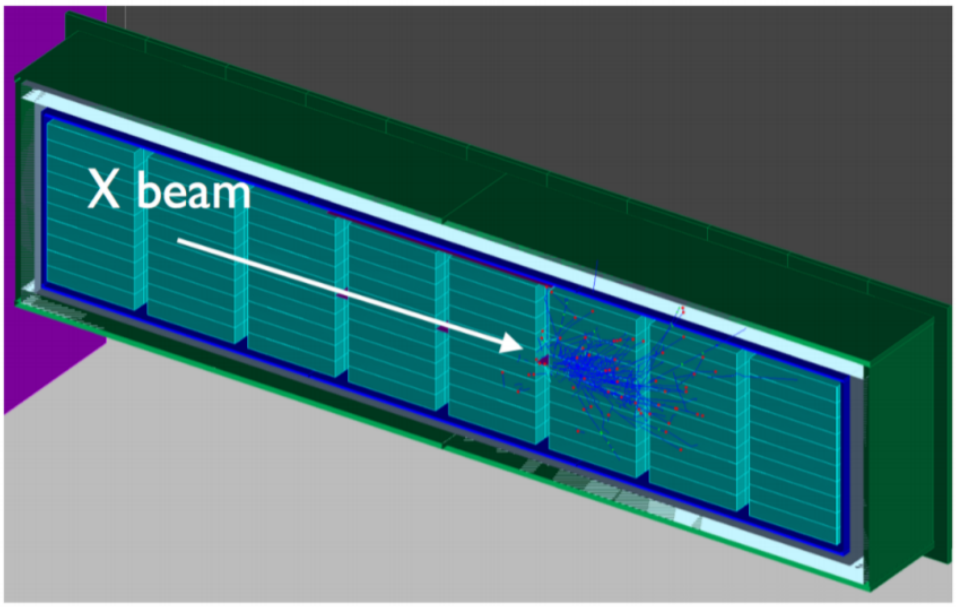

Figure 2.7: The BDX detector as implemented in GEANT4. The Outer Veto is shown in green, the Inner Veto is gray and the lead vault in blue. Crystals, arranged in 8 blocks of 10×10 are shown in light blue. A simulated electromagnetic shower from a $\chi - e^-$ scattering event in the Ecal is also shown.

(OV). A layer of lead ~ 5 cm thick placed between the Ecal and the Vetos is used to shield the latter from the low energy products of the electromagnetic showers escaping the Ecal.

The electromagnetic calorimeter The BDX Ecal is the active target of the experiment. It is made of 800 CsI(Tl) crystals, originally used in the BaBar electromagnetic calorimeter endcap (see Fig. 2.8) [54]. The choice of CsI(Tl) as scintillating material for the ECal has been motivated by extensive tests on different scintillating crystal samples, whose results are presented in [26]. CsI(Tl) proved to be an optimal choice for BDX, given its large light yield and relatively high density. BaBar crystals have different shapes and tapering: they will be inserted in new regular-shaped parallelepiped aluminum alveoli in order to have regular elements easy to assemble in variable-size arrays. The average size of each crystal is $(4.7 \times 5.4 \times 32.5)$ cm^3, while the alveolus size is $(5 \times 5.5 \times 33)$ cm^3. Since the LDM beam is focused in the forward direction, the optimal detector setup to maximize the signal yield has a compact front face and a long longitudinal extension. The detector setup plans for 8 modules of 10×10 CsI(Tl) crystals each, arranged with the long dimension along the beam direction (see Fig. 2.8). This arrangement has a cross section of 50 cm^2 for a total length of ~ 3 m. Crystals will be readout by SiPMs for a fast time

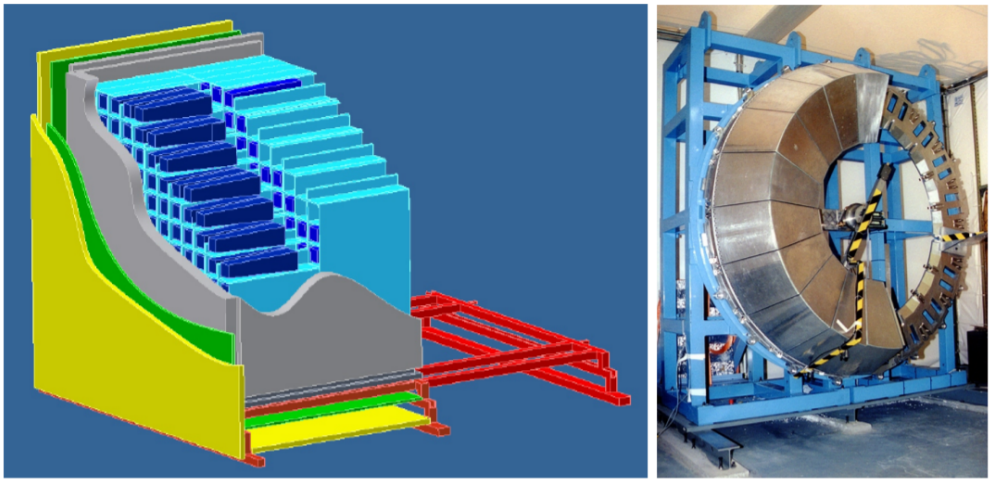

Figure 2.8: Left) Single module drawing of 10×10 CsI(Tl) crystals (dark blue), Al alveoli (light blue), lead vault (gray), Inner Veto (green) and Outer Veto (yellow). Right) Photo of the BaBar End Cap calorimeter.

coincidence with the plastic veto counters. Results of tests performed coupling BaBar crystals to 3×3 mm^2 SIPMs with different pixel sizes (25 and 50 μm) are reported in [26]. They show that a light yield of $\sim$ 10 phe/MeV and a time resolution of about 6-7 ns (for cosmic muons) is achievable, triggering on the signal rise-time. For the BDX Ecal, 4-times larger sensors (6×6) mm^2 will be used, allowing for a larger light yield. Signals from the SiPMs will be amplified by custom charge amplifiers.

The active veto system The Ecal is operated inside two hermetic layers of plastic scintillator vetos (see Fig. 2.8). Due to the relatively large surface covered, both the IV and the OV will be divided in paddles. The IV is made out of 1-cm thick plastic scintillators. To minimize the veto size and the light sensors in particular, the scintillation light in each paddle will be readout by SiPMs through 1 mm wavelength shifting fibers (WLF) hosted in grooves on the scintillator surface. In this way, it will be possible to use multiple SiPMs to read a single paddle. This solution presents many advantages: given the large attenuation length (6 m) of WLS fibers it is possible to readout large paddles with a limited number of SiPMs; the redundancy resulting by the light transmission inside the clear plastic makes any single SiPM inefficiency negligible (a hit on a paddle is acknowledged when at least one of the SiPMs fires). The OV consists of 2 cm-thick plastic scintillators readout using SiPMs, as for the IV. The SiPM signals will be amplified by the same custom charge amplifiers adopted for the ECal readout. The total number of

channels foreseen for the veto system is about one hundred.

Trigger and DAQ Since BDX is searching for extremely rare events, the trigger and data acquisition (TDAQ) system must satisfy the following requirements, in order to make background rejection possible:

- The main trigger should fire whenever the signal from a single crystal exceeds a preset threshold.
- When the trigger is satisfied, the system must readout all signals from all detectors (ECal and Veto systems).
- The activity in the detector preceding and following the trigger by up to 10 μs must be recorded and logged to tape. In this way, it is possible to reconstruct a complete "story" of the event, identifying all potential backgrounds.

In order to satisfy these specifications, a "streaming" TDAQ system was adopted. In this scheme, whenever the signal from each channel crosses a local threshold, the corresponding digitized waveform is transferred to a station of CPUs, connected by a fast network link. Here, an online software receives all data samples, reorganizes the information ordering hits by time, includes calibration constants and, at the end, applies algorithms to find specific correlations between reconstructed hits, keeping and storing only filtered events. Advantages of this scheme include the following: making use of fully reconstructed (and corrected) hits to define a high-level trigger condition; software trigger implementation in a high-level programming language; easily reprogramming to upgrade the trigger configuration and accommodate new requirements dictated by changed triggering conditions. Furthermore, the system can be scaled to match different experimental conditions (unexpected or foreseen in a planned upgrade) by simply adding more computing (CPUs) and/or data transfer (network switches) resources. A first version of a dedicated front-end board compatible with a streaming readout architecture was developed and successfully tested at JLab in April 2019 [55]. This highly configurable acquisition board includes a FPGA and 12 acquisition channels with FADC components that can be chosen within the range from 12 bits, 65 MHz to 14 bits, 250 MHz. The board provides bias voltage and amplification for each SiPM, allowing direct connection to the sensor.

2.3 Beam Unrelated Background

Beam-unrelated background is mainly due to cosmic neutrons, muons and their decay products, including rare decays of muons occurring between the passive shield and the

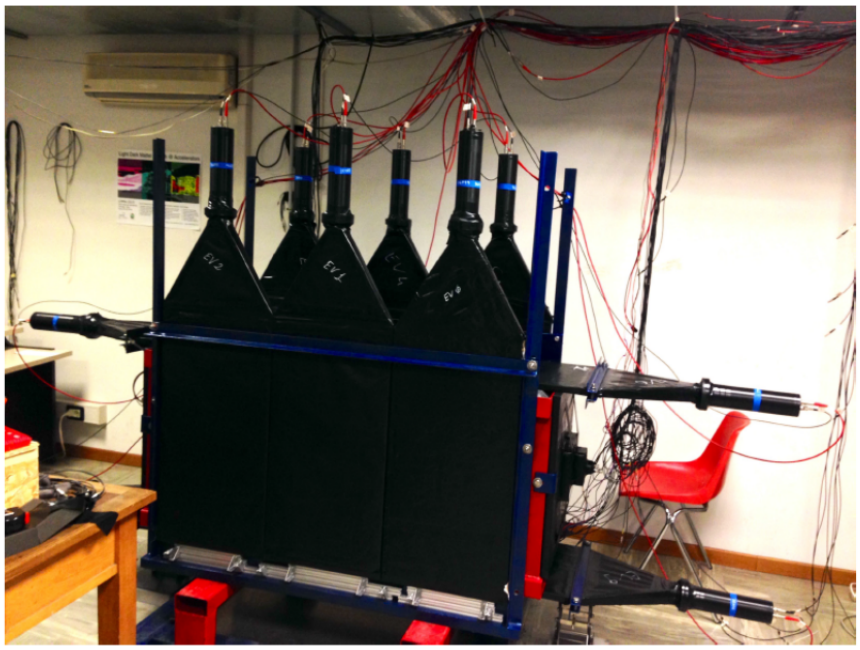

Figure 2.9: The BDX prototype used to validate the proposed technology and conservatively estimate the expected rate of cosmic background.

active veto. These events can in fact result in a energy deposition in the Ecal with no activity in the IV and OV. Both direct cosmic flow (muon and neutron) and secondaries particles (muon, neutron and gamma) contribute to the beam-unrelated background count rate in the detector. The cosmogenic background rates expected in the BDX experiment have been evaluated by extrapolating the results obtained with a prototype of the BDX detector, called BDX-PROTO. The background measurement was performed at Laboratori Nazionali del Sud (LNS) in Catania, in similar experimental conditions to those expected for the BDX experiment in terms of overburden and detector sensitivity. The characterization and operation of BDX-PROTO were the main subject of my Master thesis, whose results are described in [26]. The detector incorporated all the elements of the BDX detector, in order to provide a solid basis for a realistic estimate of the expected rates; it is composed of a single CsI(Tl) crystal, enclosed in two veto layers made with plastic scintillator (called inner and outer veto) and a lead shielding. See Fig. 2.9 for a picture of the detector. The number of cosmic events as a function of the energy threshold for a single crystal was extracted from the spectrum of events collected in anti-coincidence with the Veto System in a $\sim$1 month measurement run held at LNS. Then, an extrapolation was performed by conservatively scaling the experimental rates of a single crystal to the 800 crystals comprising the full detector. Here, I report the results of this study.

Energy threshold (MeV)	Extrapolated rate (Hz)	Expected counts (285 days measurement)
200	$(3.0 \pm 1.2) \times 10^{-5}$	740 ± 300
250	$(2.3 \pm 1.0) \times 10^{-6}$	57 ± 25
300	$(1.9 \pm 0.9) \times 10^{-7}$	4.7 ± 2.2
350	$(1.5 \pm 0.9) \times 10^{-9}$	0.037 ± 0.022

Table 2.1: Inner-veto and outer-veto anti-coincidence rate for the BDX-prototype, measured in the LNS conifiguration.

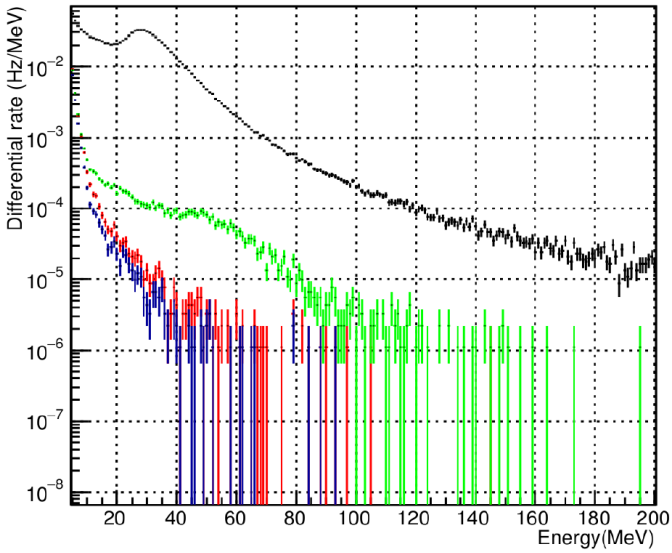

Figure 2.10: Measured event rate as a function of deposited energy in the BDX-PROTO crystal. Different colors refer to the different anti-coincidence selections: black - all events, red -anti-coincidence with IV, green - anti-coincidence with OV, blue - anti-coincidence with both veto systems.

This is certainly an upper limit on the expected rates since it assumes crystal-to-crystal fully uncorrelated counts. Table 2.1 reports some of the rates at different threshold values for high energy, which are relevant for the electron channel. In the table is also shown the projection of the counts integrated over the expected duration of the experiment. For energy thresholds in the 300-350 MeV range, the cosmogenic background counts reduce to zero. Thus, by choosing the appropriate energy threshold we could expect to have zero background.

2.4 Beam Related Background Evaluation

A large number of high energy penetrating particles (such as muons and neutrinos) are produced in the beam-dump by the interaction of the 11 GeV primary electrons. These particle can travel through the dump and shielding and hit the BDX detector, mimicking a LDM signal. This background was evaluated using high-statistics FLUKA [56] Monte Carlo (MC) simulations. The geometry and materials of the existing Hall-A beam-dump (provided by the Jefferson Lab Radiation Control Department) was included in FLUKA-2011.2c.5 together with the iron and concrete shielding and the other components of the foreseen BDX facility. We simulated the 11 GeV electron beam interacting with the beam-dump and we propagated all particles to the location of interest, sampling the flux in different locations. In order to crosscheck results we performed the same procedure using GEANT4 [57], obtaining good agreement between the two tools. Biasing techniques available in FLUKA were used in the simulation in order to obtain the highest statistics with the available computing resources. Biasing consists in a set of techniques that, artificially modifying the physics model used in the simulation, minimize the statistical fluctuations of scored quantities in a given region of interest (including both the energy range and the physical volume), while possibly increasing those elsewhere. In particular, we artificially enhanced the cross-section of photon-induced hadronic reactions, including the process $\gamma N \to \mu^+\mu^- N$, responsible for the production of high-energy muons in the dump. For a detailed description of biasing techniques used, see [2]. The simulation was performed using $\sim$300 cores for about 3 months.

Figure 2.11 shows the flux of different particles as a function of the depth in the shielding between the dump and the detector: all particles except neutrinos are ranged out before reaching the BDX experimental hall. Indeed, given a threshold of O(300) MeV, neutrinos are the only source of beam-related background. I studied in detail this background with a multi-step simulation procedure, described thoroughly in Sec. 4.2. I found that, in the optimal BDX setup, given a $O(350)$ MeV detection threshold, the expected number of

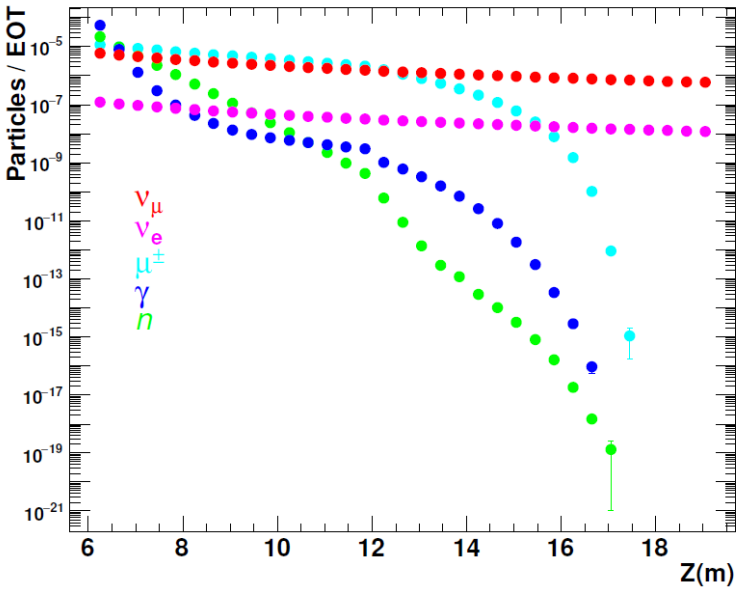

Figure 2.11: Particles fluxes per EOT at different depths in the shielding. The particle transport threshold is fixed to 100 MeV (kinetic energy)

neutrino events is ~ 5.

2.5 BDX Sensitivity

In this Section, I present the expected sensitivity of the BDX experiment, for the electron scattering channel, in the minimal *Dark Photon* scenario. The considered experimental set-up takes advantage of the maximum beam current available at JLab (65 μA) compatible with the Hall-A beam-dump, at the maximum available energy (11 GeV) for a full run that will collect 10^{22} EOT. This corresponds to a total time of 285 calendar days. In case of no events detected above the background fluctuations, BDX will permit to exclude significant regions in the LDM parameter space; for a description of systematic checks that BDX will be able to perform to corroborate any possible finding, see [26].

The evaluation of the optimized BDX sensitivity is one of the tasks I performed during my PHD; here I show the result I obtained, referring to Ch. 4 for a detailed description to the reach evaluation procedure. The red line shown in Fig. 2.12 represents the 90% Confidence Level exclusion limit set by BDX in in case of no measured excess over the predicted background, in the $y - m_\chi$ plane, being m_χ the mass of the LDM candidate and y the *thermal target*, as defined in Sec. 1.5:

$$y = \alpha_D \varepsilon^2 \left(\frac{m_{A'}}{m_\chi} \right)^4 .$$

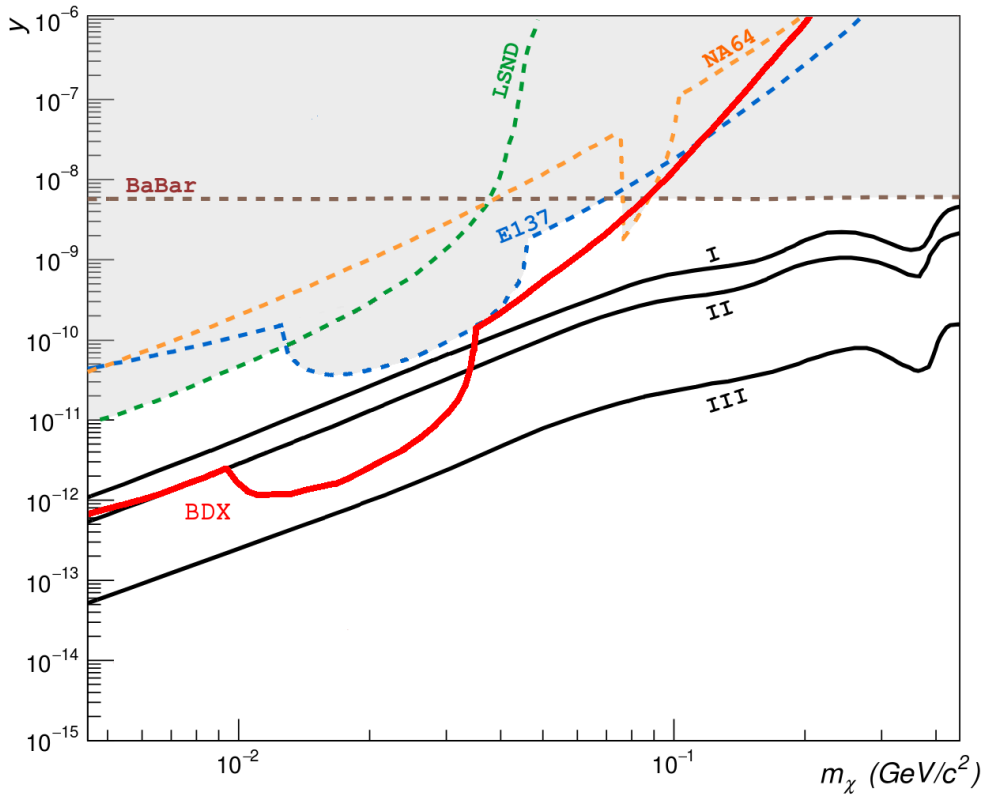

Figure 2.12: The red curve shows BDX projected sensitivity for electron scattering with a 350 MeV energy threshold for thermal relic LDM. The shape of the BDX reach curve is due to the different A' production processes involved: in particular, for χ with mass in the 10–35 MeV range the resonant annihilation of secondary positrons gives a relevant enhancement to the reach of the experiment. The thermal target (i.e. where the model predicts the correct observed DM abundance) is shown in solid black. Grey regions have already been ruled out by previous experiments.

The *relic target* (see Sec. 1.5) is proportional to y, so it does not change as the assumption on α_D varies. In the optimal setup, the expected background with a 350 MeV energy threshold is of $\sim$ 5 events, coming from the interaction in the detector of high energy neutrinos produced in the dump. No background events from cosmogenic particles are expected. As appears from the exclusion plot, BDX extends considerably the possible reach with respect to previous experiments, by up to two orders of magnitude in y depending on the m_χ value.

2.6 Status Of The Experiment

The first BDX proposal [26] has been submitted to Jefferson Lab Program Advisory Committee (PAC) in 2016. The experiment was conditionally approved: the BDX collaboration was asked to validate the simulation tools used through a measurement of the muon flux downstream of the the Hall-A beam-dump and to perform an optimization of the detector setup proposed in [26]. During my PhD I contributed to these two tasks. More details are reported in Ch. 3 and Ch. 4. An updated proposal [2] reporting the results of these studies was submitted to JLab PAC46 (2018), resulting in the full approval of the experiment with maximum scientific rating (A).

After the approval, the BDX collaboration focused its effort on the implementation of a small detector demonstrator, called BDX-MINI. BDX-MINI, a small-scale detector including all the elements of the BDX detector, was built to perform a test measurement run at JLab, proving the capability of an electron beam-dump using CEBAF. The implementation, calibration, and data analysis of BDX-MINI, whose first results are expected in summer 2020, as described in Ch. 5.

Chapter 3

BDX-HODO measurement

As described in the previous chapter, the evaluation of the beam-related background is critical for BDX. The interaction of the electron beam in the dump produces a shower of SM particles in addition to the *Dark Sector* particles. Most of these, such as photons, electrons and neutrons are contained in the beam dump where their energy is degraded to harmless levels. Penetrating particles, such as muons and in particular neutrinos, can propagate for long distances and hit the detector mimicking a DM signal. Monte Carlo simulation is the only tool to assess this background and find the best shielding and analysis cut combination to minimize it. Therefore, it is mandatory to validate simulation tools with measurements. In this respect we performed a measurement downstream the JLab Hall A beam dump to assess the muon flux generated by the interaction of the 10.6 GeV electron beam in the dump and we compared the results to the flux predicted by GEANT4 [57] and FLUKA [56] simulations.

Muons are generated in the dump by the decays of mesons produced in photo-induced hadronic reactions and in the process $\gamma N \to \mu^+\mu^- N$ (high-energy muons). In the shielding setup proposed for BDX, muons are completely ranged out; however, this test was performed in the present unshielded configuration (the space between the dump and the detector is filled with dirt) with a hodoscope detector called BDX-HODO, placed at the foreseen location of the BDX detector. In this chapter I present the details and results of this measurement, with particlular attention to the muon flux simulations and their comparison to data.

3.1 Experimental Setup

Figure 3.1 shows a schematic view of the measurement location: two wells were dug behind Hall A, at a distance of approximately 26 m (Well-1) and 29 m (Well-2) from the beam

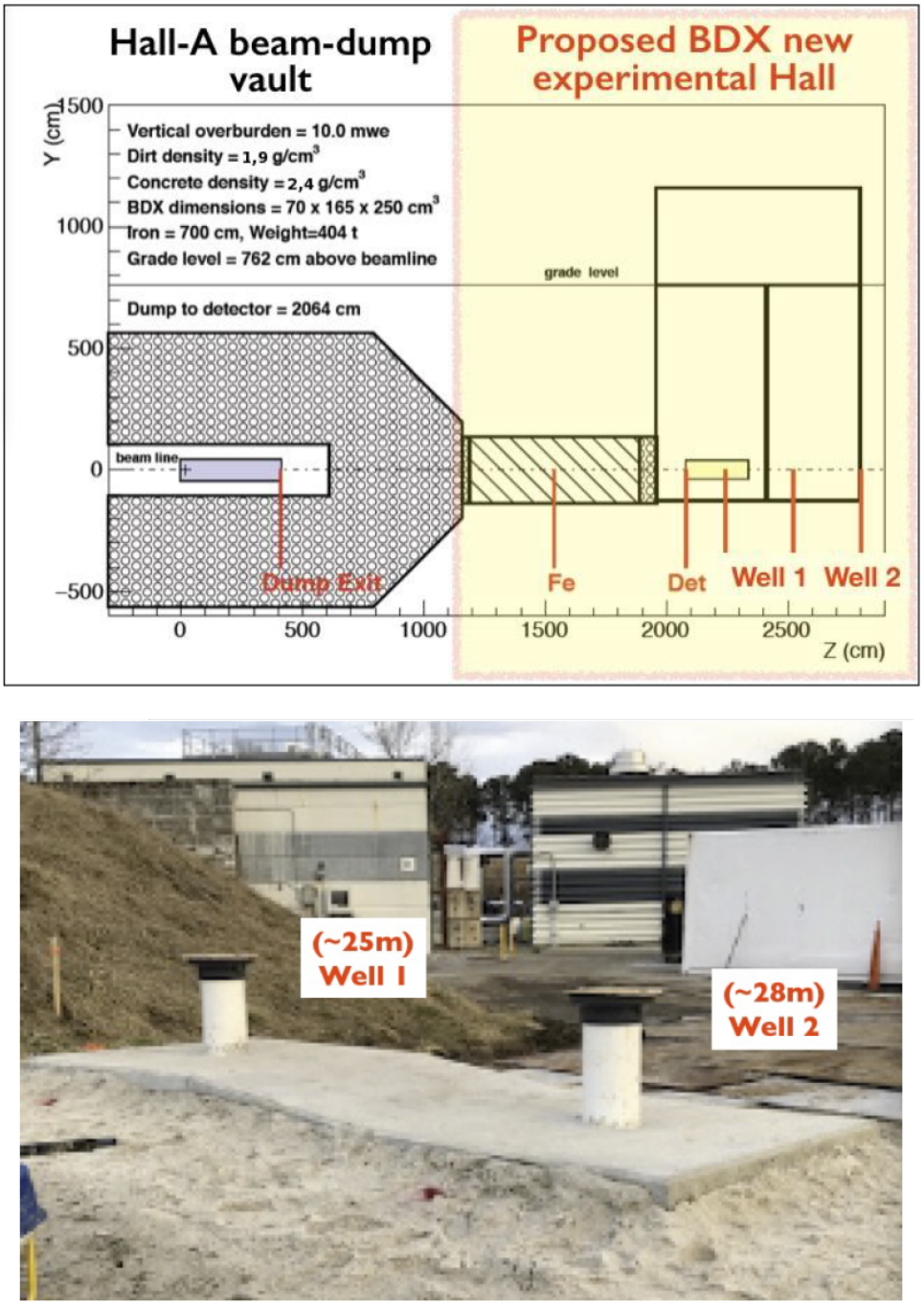

Figure 3.1: The area downstream of the Hall-A beam-dump, with the two wells dug for the the BDX-HODO measurement.

dump. The two wells intercept the muon flux at a depth of about 7 meters. Two independent surveys performed by JLab Facility and JLab Survey groups [58] [59] measured the exact location of the wells with respect to the dump. The detector, described in the next section, was enclosed into a stainless steel cylindrical vessel, in order to prevent any water leaks (see fig. 3.2B). The vessel, supported by two steel cables, was lowered inside the wells using two hand winches attached to the top of the wells. All the electronic connections of the detector were passed through 122 cm long water-tight PVC pipes, screwed together as the detector was lowered inside the well. For a more detailed description of the BDX-HODO measurement setup, see [1].

3.1.1 BDX-HODO detector

To assess the validity of the proposed BDX detector technical choices, BDX-HODO was designed using the same technology: the detector is composed by a single CsI(Tl) crystal, enclosed in plastic scintillator paddles. The crystal, originally employed in the BaBar Ecal endcap, is 31 cm long and has a trapezoidal shape, with a $4.7 \times 4.7\ cm^2$ small face and a $6 \times 6\ cm^2$ large face. A $6 \times 6\ mm^2$ Hamamatsu SiPM (S13360- 6025PE) coupled to the crystal small face is used as light sensor. A total of 13 plastic scintillator paddles surround the crystal: 4 paddles cover the side facing the beam (see fig. 3.3A), 5 paddles cover the opposite side (see fig. 3.3B). The dimensions and arrangement of the scintillators were chosen to provide a cm-scale resolution on the muon impact point on the detector front-face: the coincidence of front and back paddles defines in fact different muon trajectories. The remaining 4 scintillators cover the top-bottom and left-right faces of the crystal, and are used as vetos to reduce cosmic background. Light produced in each scintillator is collected by a wavelength-shifting fiber inserted into a groove on the paddle's surface and conveyed to a $3 \times 3\ mm^2$ Hamamatsu S12572-100 SiPM. The bias voltage for all the SiPMs is provided by custom boards, mounted on a plastic mechanical support on top of the detector, as shown in Fig. 3.2A.

3.1.2 Data Acquisition and Trigger

Each signal from the detector was sent to a 1:1 splitter, based on a passive resistor network. After splitting, one half of the signal was sent to a leading-edge discriminator (CAEN v895), while the other half was fed to a Flash Amplitude-to-Digital Converter (CAEN FADC v1725). The digital output from the discriminator was sent to a programmable logic board (CAEN FPGA v1495) implementing the trigger logic and generating the trigger signal for the FADC. All the readout boards were hosted in a VME64x crate.

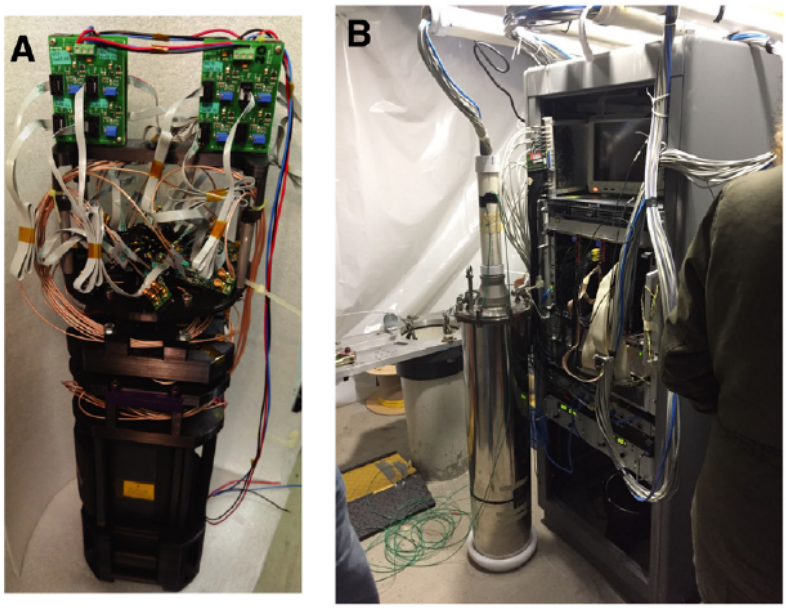

Figure 3.2: Pictures of the detector assembled (A) and inserted into the stainless steel vessel (B).

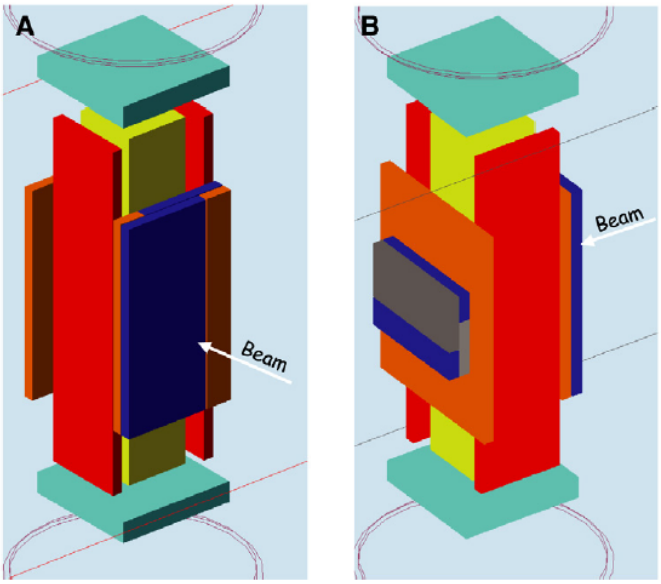

Figure 3.3: GEMC implementation of $BDX - Hodo$, front (A) and back (B) face of the detector. used

Trigger Number	Definition
0	Back-large && (front-1 ‖ front-2)
1	Top && Bottom
2	Left && Right
3	Crystal
4	50-Hz pulser

Table 3.1: Summary of trigger bits implemented in the programmable logic board. The labels *back, front, top, bottom, left* and *right* refer to the position of the plastic paddles involved in the trigger bit with respect to the crystal.

Various trigger conditions were implemented through a custom firmware for the Cyclone EP1C20 FPGA hosted in the programmable logic board v1495. Table 3.1 reports the trigger bit definition. The global trigger signal is defined as the "OR" of all trigger bits. Each trigger bit featured an independent pre-scale factor, and the corresponding rate - before and after pre-scaling — was measured through a scaler counter implemented in the firmware.

3.2 Muon Flux Measurement Campaign

The BDX-HODO measurement campaign was performed using the 10.6 GeV energy electron beam delivered by the CEBAF accelerator. The flux of muons produced in the dump was measured in the two wells at different heights with respects to the beam nominal position and for different beam currents (2.2 μA, 5 μA, 10 μA and 22 μA). The measure of the flux vertical profile at two different locations provided a relative and absolute benchmark for the Monte Carlo simulations.

3.2.1 Data Analysis

The data reconstruction was performed within the "JLab Data Analysis Framework" (JANA) [60]. To obtain the charge, the signal waveform of the crystal was integrated in a 1 μs time window; the result was then converted to MeV using calibration constants evaluated with MC simulations. As for the crystal, the signals from plastic scintillators were numerically integrated in a 1 μs time window but in this case the integral result was normalized to the single photo-electron charge (measured in dedicated runs). The selection of crossing muons was achieved by requiring a triple coincidence between the crystal and the front and back scintillator paddles, which resulted in an effective area of

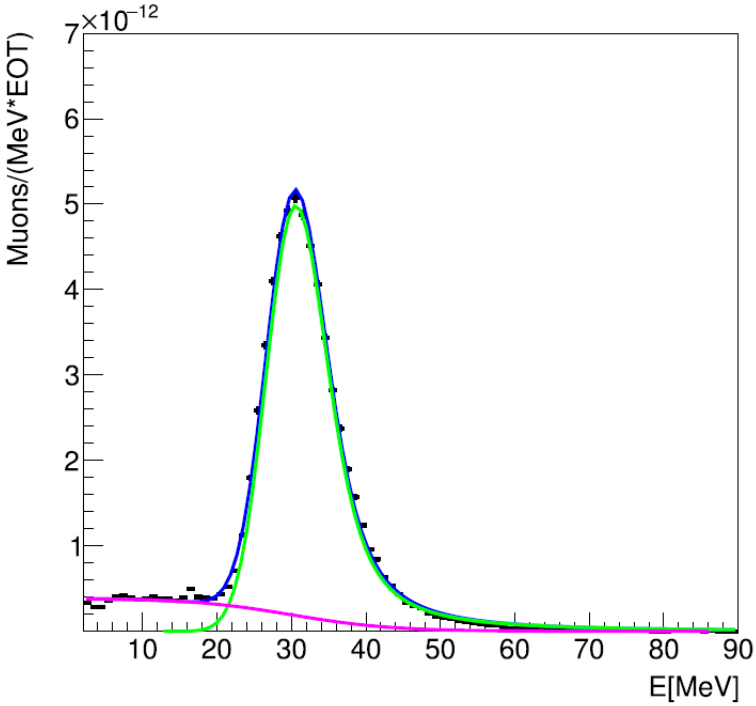

Figure 3.4: Example of a crystal energy spectrum fitted with a Landau convoluted with a Gaussian (green) and a Fermi function (pink).

$\sim$ 100 cm^2. The crystal energy spectrum measured in each data-taking run was fitted with a Landau function convoluted with a Gaussian, while the low energy background was modeled with a Fermi function (see Fig. 3.4). The rate of muons was evaluated by integrating the Landau function from 0 to 120 MeV.

3.2.2 Measurements Results

Figure 3.5 shows the muon rate as a function of the detector height with respect to the beam-line for Well-1 and Well-2 (positive values refer to positions above the beam-line). In the figure, the points have been shifted by -10 cm (Well-1) and -40 cm (Well-2) to center the peaks at the beam-line height. As discussed in the next section, we concluded that this shift is probably due to the presence of a non-uniform dirt density profile between the dump and the wells position. The measured rates can be converted in fluxes considering the area of the detector and the current of the beam: the maximum muon flux measured in Well-1 and Well-2 are $\sim 4\frac{Hz}{\mu A \cdot cm^2}$ and $\sim 8.3 \times 10^{-3}\frac{Hz}{\mu A \cdot cm^2}$. The $\sim$ 470 factor between the fluxes in the two wells (separated by only 2.7 m) indicates the extreme sensitivity of the measured rate to the length of the muon path in the dirt and proves that the position

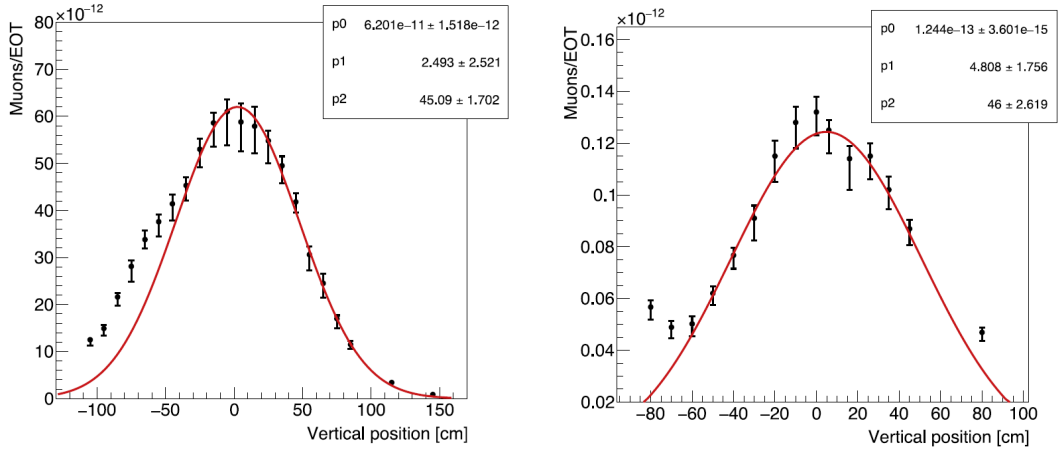

Figure 3.5: Muon rate as a function of the hodoscope vertical position in Well-1 (left panel) and Well-2 (right panel). The corresponding beam current is $I = 22\ \mu A$.

of Well-2 is close to the maximum muon range. The vertical profiles of the rate show approximately symmetrical distributions that were fitted to Gaussian functions obtaining similar widths of about 45 cm for both Well-1 and Well-2.

3.3 Monte Carlo Simulations

The simulation of the muon flux at such a distance ($\sim$ 30 m) from the beam-dump where muons are generated presents several criticisms. Firstly, the position of the wells is close to the maximum muons range: only the most energetic ones can therefore reach BDX-HODO. Moreover, given the small crystal cross-sectional area and its distance from the dump, only a small fraction of most energetic muons hit the detector. For this reason, a straightforward simulation of the flux starting from primary electrons would require an overwhelming computing power. As an example, less than $\sim 10^{-11}$ muons per electron on target (EOT) hit the detector in Well-2. Secondly, as described below, the muon rates depend critically on the density of the material between the dump and the wells so that a few percent change in this quantity results in large variation in the rates. Two soil samples were taken near the wells location resulting in $\rho_{dirt} = 1.93 g/cm^3$ and $1.95 g/cm^3$, which suggests that a order $\sim$ percent uncertainty on ρ_{dirt} must be considered. Another source of error is given by the density of the concrete used to build the bunker surrounding the beam-dump; since we could not sample it we assumed a nominal value in the range 2.2-2.4 g/cm^3 . Therefore, to estimate the systematic associated with the density it is necessary to perform different simulations varying independently ρ_{dirt} and $\rho_{concrete}$.

In order to address these issues we adopted two different approaches, using FLUKA and GEANT4. The FLUKA simulations were performed using a heavily biased model, in order to enhance high energy muon production and transportation towards the detector, which allowed to reduce severely the required computing power [2]. For GEANT4 simulations we used a two step process, without using any biasing. Since the two approaches proved to be in good agreement and being FLUKA more efficient thanks to biasing, we decided to use it to get the muon fluxes impinging on the detector. GEANT4 results were therefore used as a benchmark. The detector response to muons was evaluated in a separate GEANT4 simulation, using muon events obtained with FLUKA as an input.

Since my work focused on the GEANT4 simulations, here I will describe in detail the procedure I followed with GEANT4 to evaluate muon fluxes and to simulate the detector response. For a thorough review of the simulations performed with FLUKA, see [2].

3.3.1 Muon Flux Simulation Procedure

The full geometry of the Hall-A beam dump as well as the concrete bunker and the two wells were implemented in GEANT4 via the GEMC interface [61]. To keep running time reasonable, only particles with energy greater than 100 MeV have been tracked and sampled. As a first step I simulated a total of 1.3×10^{10} 10.6 GeV electrons, and I sampled the muon flux exiting from the beam-dump. The results were used as a benchmark for the heavily-biased FLUKA simulations. Figure 3.6 shows the comparison between the two tools: the agreement is reasonable even if the statistical limitation of the Geant4 data results in larger error bars if compared to FLUKA. Once that the good agreement with FLUKA and Geant4 was established, I proceded as follows:

1. I run a large statistics simulation starting from primary 10.6 GeV electrons impinging on the beam-dump and I sampled the muons crossing a large planar surface located at the end of the dump. Only muons with kinetic energy higher than 4 GeV were considered.

2. I built a 3-D distribution of the sampled muons kinetic energy E, azimutal angle θ (with respect to the beam direction) and distance from the beam axis R (see Fig. 3.7 for a 2-D projection of the obtained distribution).

3. I run a new simulation generating muons from the end of the beam-dump, extracting E, θ and R from the aforementioned 3-D distribution (the polar angle was extracted randomly, given the cylindrical symmetry of the beam dump).

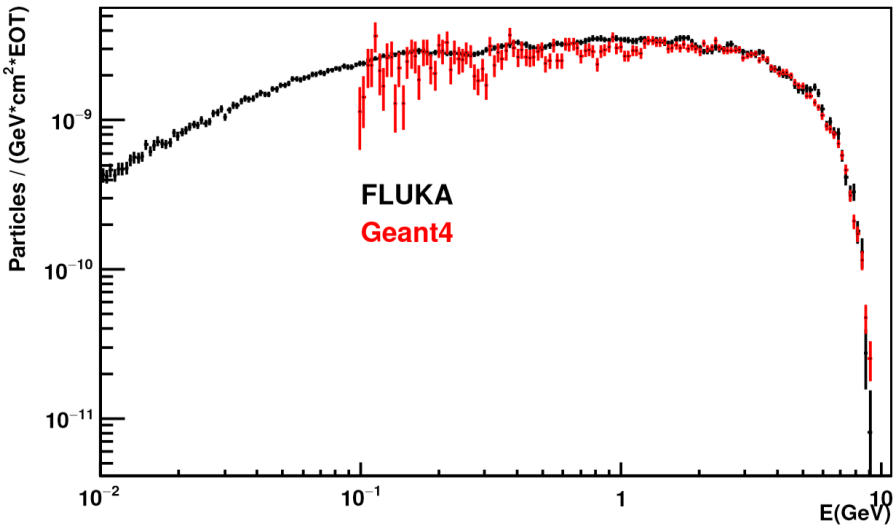

Figure 3.6: Simulated muon fluence at the beam-dump exit by FLUKA (black) and Geant4 (red).

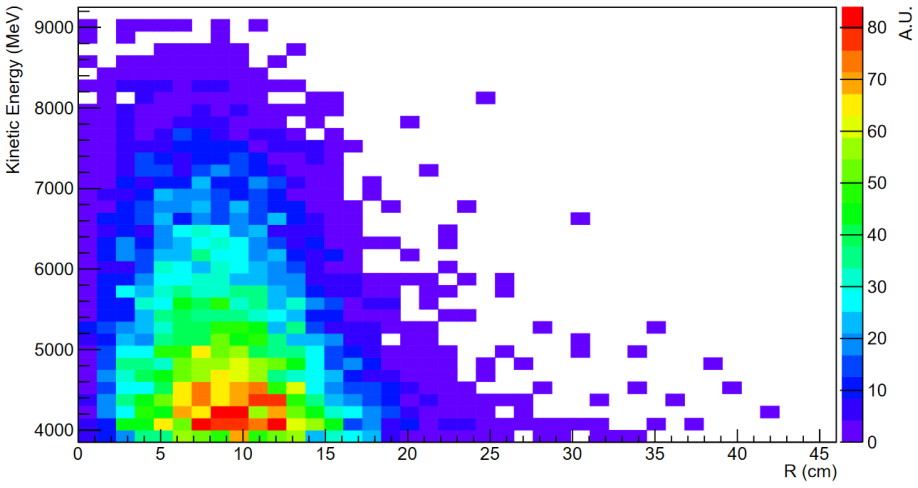

Figure 3.7: Projection of the 3D distribution of sampled muons on the $E - R$ plane.

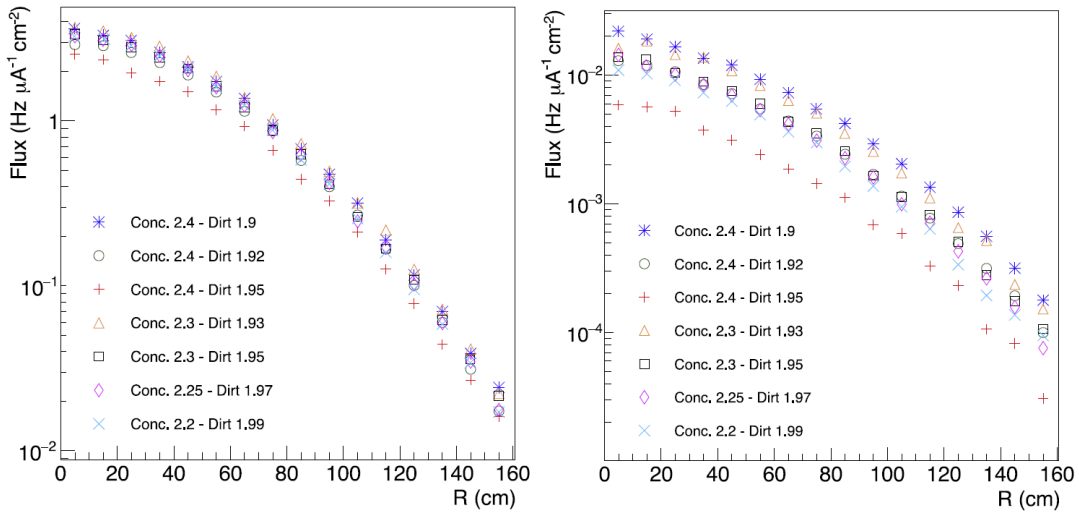

Figure 3.8: Simulated muon flux as a function of the vertical position in Well-1 (left) and Well-2 (right), for different combination of ρ_{dirt} and $\rho_{concrete}$. Values quoted are expressed in g/cm^3.

This approach features various advantages. Firstly, it reduces by several orders of magnitude the computational time required to run simulations: in order to cross the concrete bunker and the dirt, reaching the location of BDX-HODO, a muon must be generated in the beam-dump with high energy (at least of order of $\sim 5-6$ GeV). As mentioned before, the production of such high energy muons is a rare event; the vast majority of the simulated electron events results in no muons exiting the beam-dump enclosure. Generating only μ with larger energy than 4 GeV from the aforementioned sampling surface allows to vastly reduce the simulation time. Secondly, decoupling the muon flux production in the dump from the muons propagation to the detector in two distinct simulations allows to perform different test varying the dirt and concrete density, without having to perform again the muon generation for each density configuration tested. This latter feature was useful for the estimation of the systematic error on the fluxes associated with the uncertainties on ρ_{dirt} and $\rho_{concrete}$, as described in the following section.

3.3.2 Systematic Error on Muon Fluxes

In order to assess the systematic error associated with the uncertainties on ρ_{dirt} and $\rho_{concrete}$ I performed different simulations: starting from the muons distribution sampled at the dump exit, as described in the previous section, I simulated the muon propagation towards the BDX-HODO detector, varying systematically the values of ρ_{dirt} and $\rho_{concrete}$

respectively in the ranges (1.9-1.99)$\frac{g}{cm^3}$ and (2.2-2.4)$\frac{g}{cm^3}$. For each configuration, I calculated the flux of muons reaching the two pipes, at different heights with respect to the beam line. The results of this study are shown in Fig. 3.8: the markers show the muon flux at the wells location, as a function of the distance from the beam height R, for different $\rho_{dirt} - \rho_{concrete}$ combinations. The R profile of the flux is roughly gaussian, with a slightly larger width in Well-2 than in Well-1, due to the muons multiple scattering in the dirt. The profile shape is not affected, to a first approximation, by the density variations, while the flux magnitude varies considerably, up to 30% in Well-1 and up to a factor ~ 4 in Well-2, depending on the density configuration. As a result, the density uncertainty systematic affects also the ratio between the muon rates in the two wells. As expected, the uncertainty on $\rho_{concrete}$ affects the muon flux less severely than the error on ρ_{dirt}. To reach Well-1 (Well-2) location, in fact, muons travel for about 14 m (17 m) in dirt and only 4 m in concrete.

FLUKA simulations predict the same critical dependence of the μ fluxes on $\rho_{concrete}$ and ρ_{dirt} values, which confirms the validity of the simulation procedure I adopted. Since a precise knowledge of the concrete/dirt density would have required an effort beyond the scope of the measurement, we considered the variation described in this section as a systematic error band on the simulations result.

3.3.3 Inhomogeneous Dirt Density Test

As mentioned in Sec. 3.2.2, the measured flux profiles in the two wells have a gaussian shape with a shift with respect to the beam height, about 10 cm for Well-1 and 40 cm for Well-2. Given the strong dependence of the muon flux on the dirt density, we assumed that this shift may be due to the density unevenness of the dirt along the muons trajectory. To test this hypothesis, I performed a simulation of the muons propagation in the following configuration: I divided the dirt region between the concrete bunker and Well-1 in two halves; in the upper half I set the dirt density value to $\rho_{dirt} = 1.95\ \frac{g}{cm^3}$, while in the lower half I set it to a 2.5% lower value $\rho_{dirt} = 1.9\ \frac{g}{cm^3}$ (see Fig. 3.9 for a sketch of this configuration). I then propagated muons from the dump to the wells location, following the procedure described in the previous sections. Figure 3.10 show the resulting flux profile in Well-1: the peak of the distribution is shifted down by ~ 6 cm. I observed a more significant shift in Well-2, where the maximum of the profile is shifted by ~ 30 cm. These results, even if only qualitative, prove that a slightly uneven dirt density distribution can be responsible for an appreciable modification of the muon flux profile. Moreover, the fact that the shift is more significant in Well-2 is in agreement with the measurement (see Sec. 3.2.2), supporting the hypothesis of the shift being originated by the heterogeneity of dirt

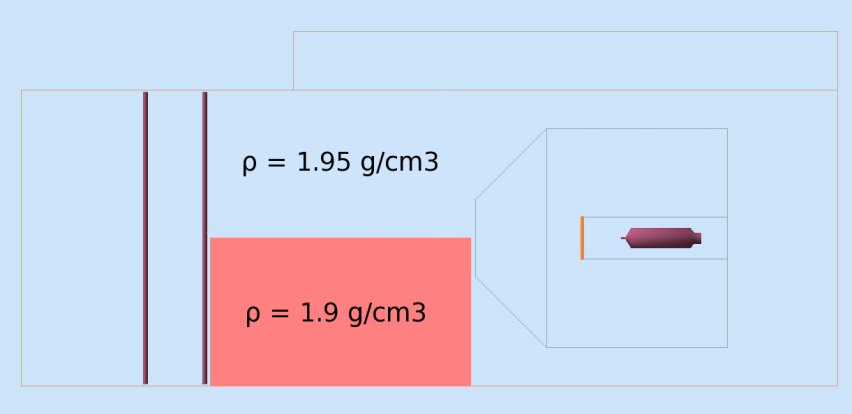

Figure 3.9: View of the uneven dirt density profile implemented in GEMC. From the left to the right: Well-2 and Well-1, dirt, the concrete bunker and the beam-dump (in purple). The orange line represents the planar surface were the muon flux was generated.

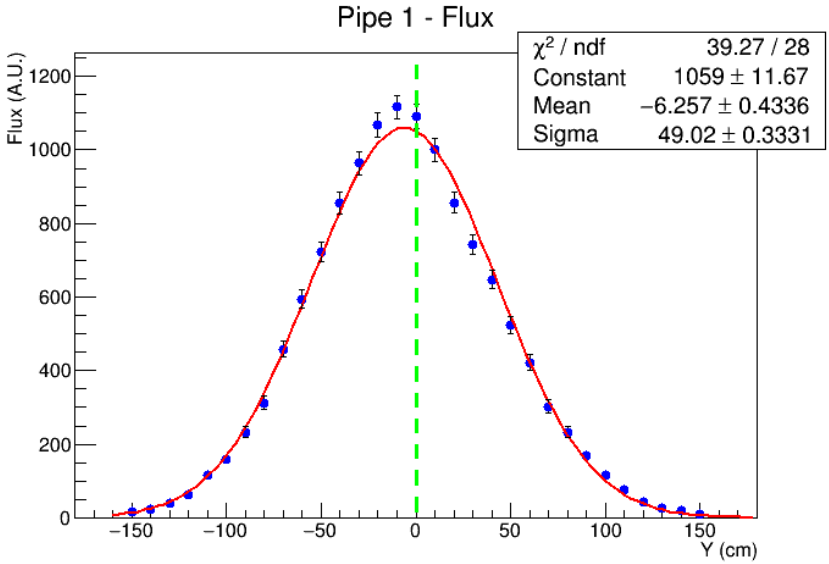

Figure 3.10: Resulting muon flux in Well-1 for the uneven dirt density profile tested. The 2.5% density variation between the upper and lower halves of the dirt region crossed by muons results in a ~ 6 cm shift in the peak of the flux distribution.

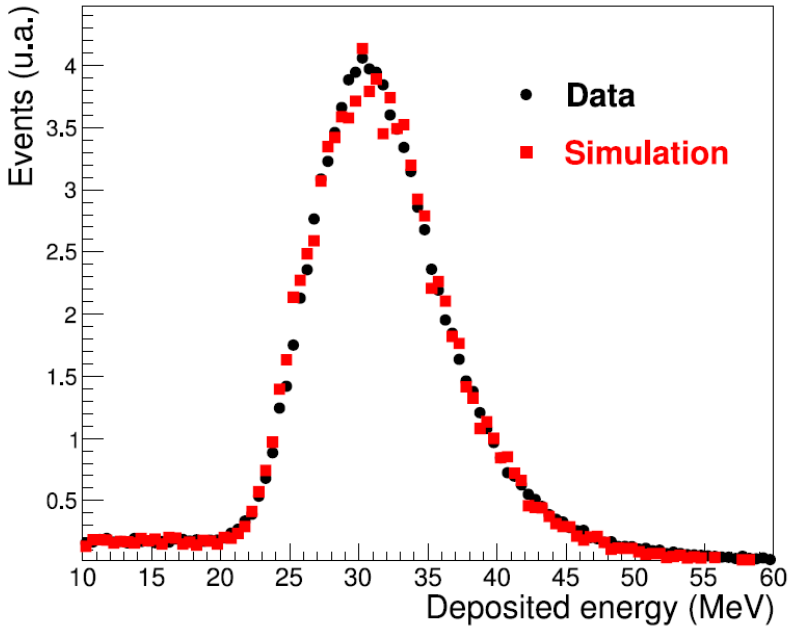

Figure 3.11: CsI(Tl) crystal energy spectrum for events with a coincidence between crystal, front and back plastic scintillator counters. Data are shown as black circles while red squares represents simulation results.

in the region behind the bunker.

3.3.4 Detector Response

The simulation of the detector response to muons was performed with GEANT4. FLUKA was used to generate muons in the beam-dump and propagate them to a plane near the detector. From there, GEANT4 was used to track particles all the way up to the detector. I contributed to the GEANT4 detector response simulation, using muons sampled with FLUKA as an input. We implemented the detector in the GEMC framework; in particular, the detailed description of the CsI(Tl) crystal response includes: a light yield (LY) of 50,000 Photons/MeV and a scintillating decay time of 800 ns (as measured by BaBar Collaboration [54]), a Birks constant of $3.2 \times 10^{-3}\, g/(MeV\, cm^2)$ [62], the charge collection spread induced by the finite crystals attenuation length of 53 cm, as reported in [63], and the SiPM nominal photon detection efficiency (PDE) at the wavelength corresponding to the maximum of the CsI(Tl) scintillation emission spectrum. Using these values it was possible to generate a realistic time-dependent detector response whose integral was compared to the measured energy spectrum.

Since plastic scintillator paddles were only used to tag muons, limiting the angular and

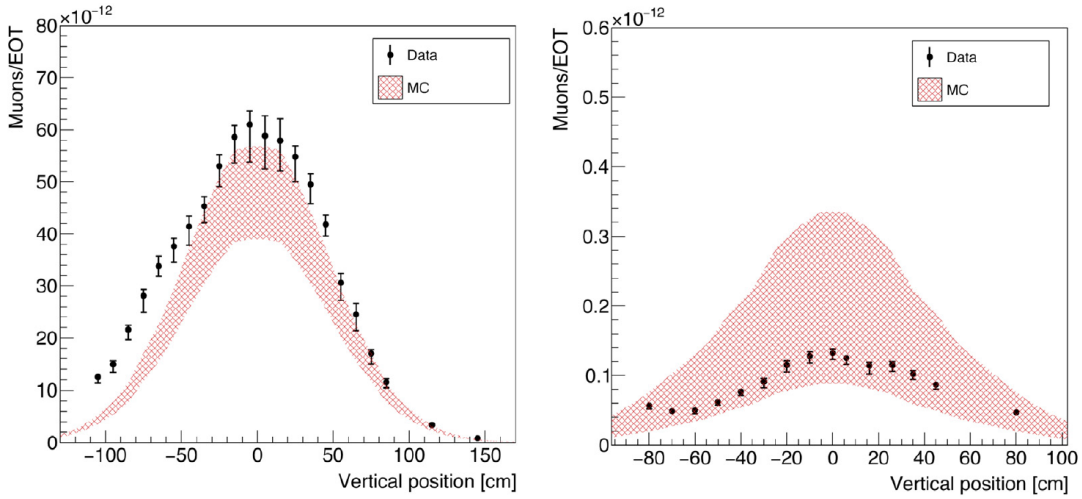

Figure 3.12: Comparison between measured (black markers) and simulated (red band) muon rates. Well-1 (Well-2) is shown on the left (right) panel. The wide red band includes the systematic error related to the dirt and concrete density uncertainty.

the path-length spreads in the crystal, we implemented their response in the simulation in an effective way. The response in photoelectrons as well as the inefficiency to detect a crossing cosmic muon were measured for each paddle in dedicated tests before assembling the detector. On average, a minimum ionizing particle (MIP) was found to have the most probable value of the associated Landau distribution in the range of 170–200 photoelectrons with a detection efficiency $> 98\%$. We implemented these parameters in the simulation, in order to obtain a realistic paddle response allowing for MIP events selection.

Figure 3.11 shows the energy spectrum in the CsI(Tl) crystal, after selecting events with coincidence between crystal, front, and back plastic scintillator counters: data are shown as black circles while simulation results are shown as red squares. The absolute scale of each distribution was tuned to have the same normalization for deposited energy > 10 MeV. The two distributions are in very good agreement, confirming the goodness of the crystal response parameterization in MC to passing-through muons.

3.4 Results And Conclusions

The BDX-HODO response simulation described in previous section was repeated varying the detector vertical position in the two wells, in order to obtain a rate profile that could be compared with measured data. Fig. 3.12 shows the comparison of the measured and simulated rates as a function of the vertical height. Simulations, normalized to the beam

current, agree to experimental data both on absolute values and shape of the rate profile. In fact, taking into account the systematic error (see Sec. 3.3.2), they are able to reproduce the suppression factor of ∼500 between rates measured in Well-1 and Well-2 as well as the gaussian shape and width. This good agreement in absolute value and shape demonstrates that the simulation framework can safely be used to estimate the beam-related muon background in the BDX experimental set-up.

The results of this test were included in the 2018 update of the BDX proposal, together with the BDX optimization work described in the following chapter. This document was submitted to Jefferson Lab PAC46, resulting in the full approval of the experiment.

Chapter 4

BDX Reach Optimization

This chapter illustrates the procedure I adopted to optimize the BDX experiment reach, identifying the set of selection cuts and the experimental setup resulting in the best sensitivity to the LDM parameter space.

As described in [2], the sensitivity s of a counting experiment such as BDX depends on the foreseen average of background counts B as follows:

$$s \simeq 2.3 + 1.5\sqrt{B}.$$

The expected number of signal events depends on the parameters of the LDM model: ε, α_D, $m_{A'}$ and m_χ. For this study, the value of $\alpha_D = 0.5$ was considered, and the ratio between the masses of the LDM particle χ and the A' was fixed to $\frac{m_\chi}{m_{A'}} = \frac{1}{3}$. The minimum value of ε that BDX can probe is therefore given by:

$$N(\varepsilon_{min}, m_\chi) = 2.3 + 1.5\sqrt{B}.$$

In this formula, both the value of B and the dependence of N on ε and m_χ depend on the detector setup and on the selection cuts applied in the analysis. In order to optimize the experiment reach, I performed a study of the signal detection efficiency and background rejection capability of BDX varying systematically the cuts and the experimental setup. For the signal and beam-related background, I based my work on Monte Carlo simulations, while cosmic background estimates were based on the results of BDX-PROTO (see Sec. 2.3). In the following, I assumed that the background yield B is known with a negligible uncertainty. In any case, since the expected B value in the optimized configuration is $B \simeq 5$ events (see next sections), even considering an uncertainty on the background ${\sigma_B}^2 = O(B)$ results in a negligible correction to the sensitivity and minimum coupling ε_{min} that BDX can probe. In the BDX experimental analysis, the effect of background uncertainty will be taken into account through *nuisance* parameters, as described in [2].

In the following sections I will describe the procedure adopted to evaluate expected signal and background counts as a function of selection cuts and detector setup.

4.1 Signal Evaluation

Results were obtained considering the minimal *Dark Photon* model described in Sec. 1.5: the A's are produced in the beam-dump via A'-strahlung of electrons and secondary positrons and decay to $\chi\bar{\chi}$ pairs; χs travel through the dump and the passive shielding reaching the detector, where they can interact via elastic scattering with electrons. In this scenario, the ratio between the A' and χ masses is set at $m_{A'} = 3m_{\chi}$. The estimate of the signal yield involves three steps. First, the evaluation of the number of χ particles produced in the dump. Then, the calculation of the interaction rate in the detector and the simulation of the process. Finally, the study of detector response to the electrons scattered by LDM particles.

4.1.1 χ Production

The interaction of the electron beam in the dump gives rise to an electromagnetic shower. Both electrons and positrons in the shower hence contribute to the total A' yeld of the experiment. The showering of the electron in the dump is usually neglected in this kind of calculation and the solution adopted is to use the "single-radiation length approximation" [35] [40] i.e. to consider an effective length of the target equal to one radiation length, neglecting shower propagation and energy loss effects. I proceeded differently, in order to take into account the showering effect; GEANT4 was used to simulate the flux of electrons and positrons as a function of energy, at different depths in the dump (in radiation lengths). A simplified model of the dump was adopted, considering a uniform Aluminum cylinder. However, all results are expressed in radiation length units and the shower propagation dependence on the material is, to a first approximation, included in this quantity: therefore, no sizable effect due to this approximation is expected. The simulation provided the differential track-length distribution of electrons $T_{-}(E)$ and positrons $T_{+}(E)$ in the dump, normalized to the number of primary particles. From this quantity, the total number of $\chi\bar{\chi}$ pairs produced per EOT can be calculated as follows:

$$N_{\chi\bar{\chi}} = \frac{N_{Av}}{A}\rho X_0 \int_{E_{min}}^{E_0} dE\,(T_{+}(E) + T_{-}(E))\,\sigma(E),$$

where ρX_0 is the product of the Al density and radiation length (24.01 g/cm^2), A is the Al atomic number, $\sigma(E)$ is the total cross section for the $e^{-}N \rightarrow e^{-}NA' \rightarrow e^{-}N\chi\bar{\chi}$

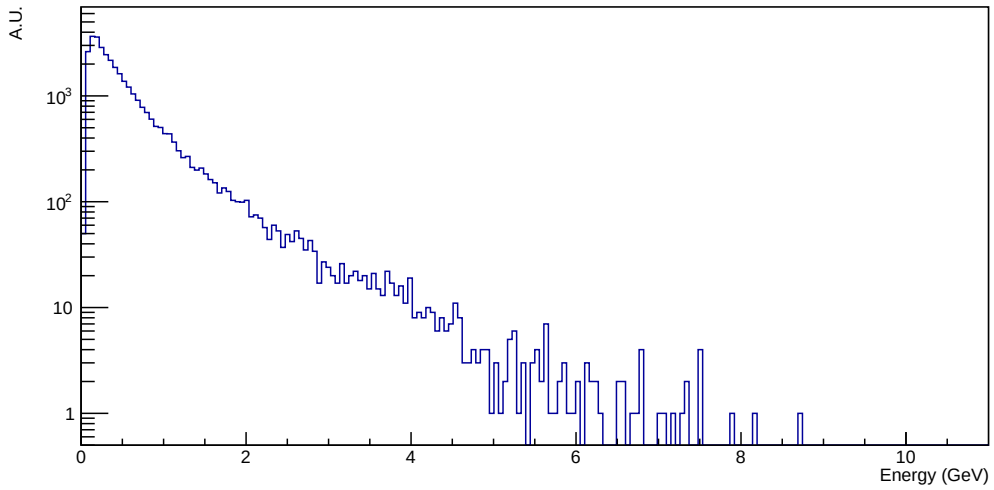

Figure 4.1: Energy spectrum of scattered electrons in the detector, for $m_{A'} = 30\ MeV$, $m_\chi = 10\ MeV$ (a 100 MeV energy threshold has been applied).

process, E_0 is the primary electron energy and E_{min} is the threshold energy. Note that the positron and electron track-lengths have been summed since positrons can produce $\chi\bar{\chi}$ pairs in the dump just like electrons. The simulation of the χs production was performed using a modified version of MadGraph4 [64]. It was used to simulate the LDM events and to calculate the production cross section $\sigma(E)$. For different values of m_χ in the $1 - 150$ MeV mass range, the total χ energy spectrum and yield was estimated by numerically integrating the expression above. For more details, see [26].

4.1.2 χ Interaction

As described in Sec. 2.1.2, χs will be detected via the elastic scattering on atomic electrons of the BDX detector. This process was handled through a custom code: the program, given the incident χ spectrum obtained by MadGraph4, computes the expected event rate within the detector, for a given value of the coupling $\varepsilon_{ref} = 3.87 \times 10^{-4}$. It also provides a set of Monte Carlo events, containing scattered electrons in the detector volume, generated according to the foreseen kinematics. The corresponding cross-sections were implemented in the code, according to the formulas described in [35] The energy spectrum of recoiling electrons, computed for $m_\chi = 10\ MeV$ is shown in Fig. 4.1. The distribution is enhanced at low energies; this is due to the contribution of secondary electrons and positrons produced in the shower. These lower energy particles produce a large amount of LDM particle pairs, contributing significantly to the experiment sensitivity.

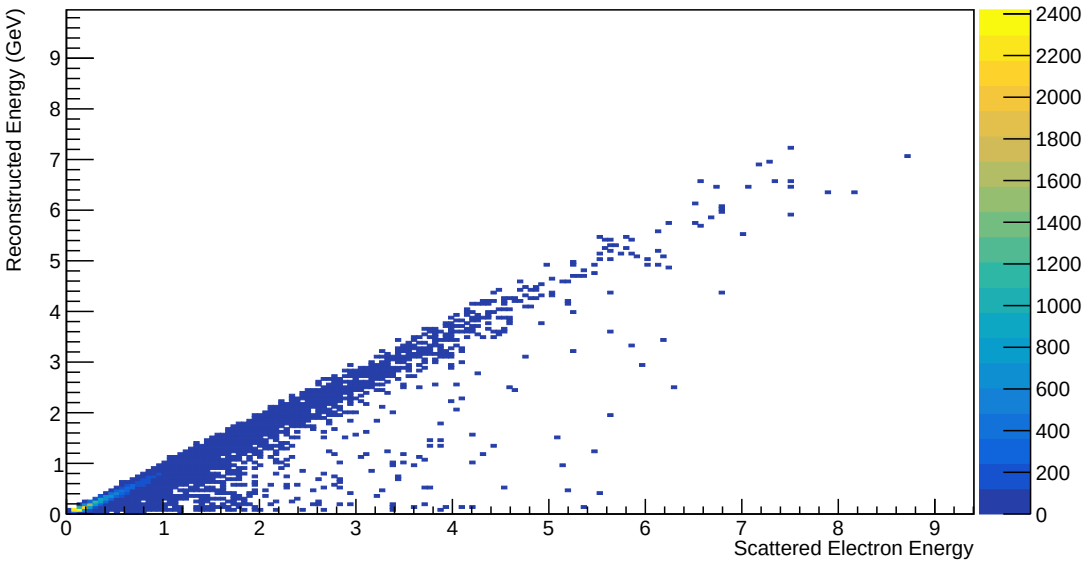

Figure 4.2: Energy spectrum of scattered electron in the detector, for $m_{A'} = 30\ MeV$, $m_\chi = 10\ MeV$ (a 100 MeV energy threshold has been applied).

4.1.3 Detector Response

The BDX detector response to scattered electrons has been studied with a GEANT4-based simulation code [61]. The aforementioned sets of electron events, one for each m_χ value, were used as an input to this simulation, which included the complete BDX detector description (realistic detector geometry, parameterized response of CsI crystals and plastic scintillator vetos). As described above, the code used to generate events provided the total number of foreseen scattered electrons N_I in the detector per EOT, at a the coupling value $\epsilon_{ref} = 3.87 \times 10^{-4}$. Since N_I scales as ε^4, the number of interactions for an arbitrary ε value is:

$$N_I(\varepsilon) = \frac{\varepsilon^4}{\varepsilon_{ref}^4} N_I(\varepsilon_{ref})$$

It is therefore possible to obtain the expected signal rate as a function of ε without having to perform different simulations. As described in detail in the following sections, the detector response has been simulated for different configurations, varying the position of the lead shielding and the crystals dimensions, in order to find the optimal setup providing the best sensitivity to LDM. Figure 4.2 shows the correlation between the generated electron energy and the total energy reconstructed, for $m_\chi = 10$ MeV, for the optimal BDX detector setup. As expected, the energy reconstruction capability of the detector depends on the scattered electron position: if the electron vertex is close to the edge of

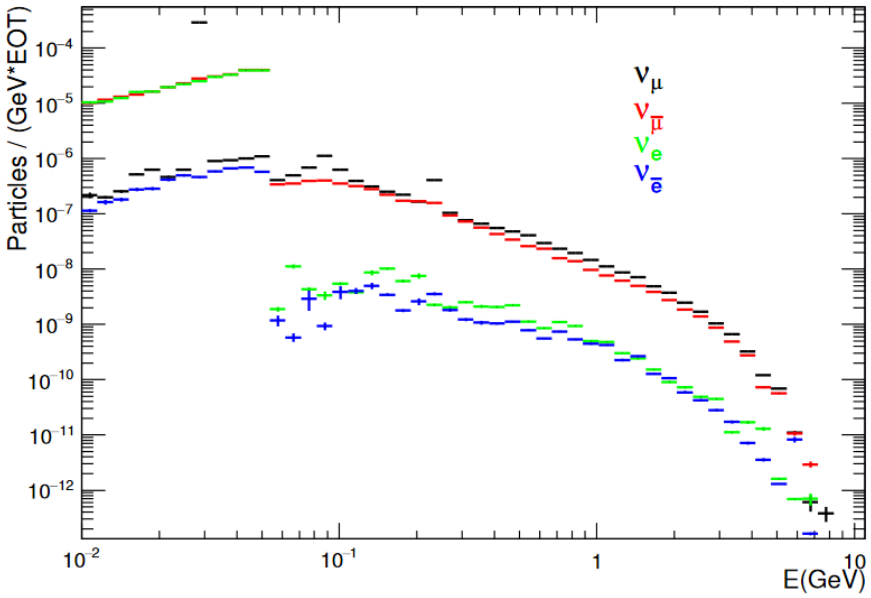

Figure 4.3: Differential energy spectrum of neutrinos ($\nu_\mu, \bar{\nu}_\mu, \nu_e$ and $\bar{\nu_e}$) impinging on the BDX detector volume.

the calorimeter, the event energy is reconstructed only partially. However, given the dimension of the detector and the focusing of the impinging χ beam, the vast majority of hits happens in the central core of the detector, resulting in a good overall signal energy reconstruction capability.

4.2 Beam Related Background

As described in Sec. 2.4, the only SM particles produced by the beam interaction in the dump that can produce a background in BDX detector are neutrinos. In fact it is possible to find an optimized shielding setup that ranges out all other particles (muons, neutrons, gammas,..) [2]. Neutrinos ($\nu_\mu, \bar{\nu}_\mu, \nu_e$ and $\bar{\nu_e}$) are produced in muon decays and hadronic showers (pion decay). The majority come from pion and muon decay at rest but a non negligible fraction, due to in-flight pion and muon decay, receives a boost in energy up to several GeV. High energy neutrinos interacting with BDX detector by elastic and inelastic scattering may result in a significant energy deposition -O(300) MeV- that may mimic an EM shower produced by the $\chi - e$ interaction. In order to evaluate the background contribution due to neutrino interactions, a multi-step procedure was employed:

- The differential neutrino flux, with respect to energy and angle, was sampled on the front-wall of the underground hall where the detector is located. To perform this

calculation we used a FLUKA high-statistics simulation, as described in Sec. 2.4.

- Neutrinos were propagated from the front-wall to the detector volume, where an interaction with the Cs-I nuclei was forced. The primary vertex was randomly distributed along the neutrino trajectory within the detector volume. Both the total interaction cross-section (averaged over the two nuclei) and the kinematics and topology of produced particles were sampled on an event-by-event basis.

- The response of the detector to neutrino secondaries was studied with same procedure adopted for signal events: sets of secondary particles events were used as an input for a GEANT4-based simulation including the response of the detector.

This procedure allowed as to compute the neutrino flux once. The second and third steps were repeated as needed to study different detector setups.

4.2.1 Neutrino Flux Evaluation

The evaluation of the neutrino flux, was performed with FLUKA, considering a simplified model of the Hall-A beamline (only beam-dump included) and assuming a pencil-like 11-GeV beam. The latter assumption is conservative, since an angular spread in the primary beam would reflect in secondary neutrinos, reducing the actual flux on the detector. Figure 4.3 shows the neutrino differential spectra sampled on the detector front face. A small but not negligible part of the spectrum shows energy greater than the detection threshold, O(300) MeV (see the following sections). These events may produce signals in the BDX detector that mimic LDM interactions, thus generating backgrounds and limiting the experimental reach.

4.2.2 Neutrino Interactions In The Detector

Neutrino-nucleus interactions in the detector were simulated by using NUNDIS and NUNRES [65] [66], the FLUKA internal neutrino-nucleon interaction generators. NUNDIS and NUNRES were developed on the basis of the results achieved by the effective nuclear models implemented in FLUKA, which have good predictive power in hadron interactions. The codes simulate both charged current (CC) and neutral current (NC) interactions, for all neutrino species. In order to validate the results, we compared them with those obtained using the GENIE code [67], another widely used simulation tool in the neutrino community. Results obtained from the two codes were found to be in very good agreement (see [2] for more details).

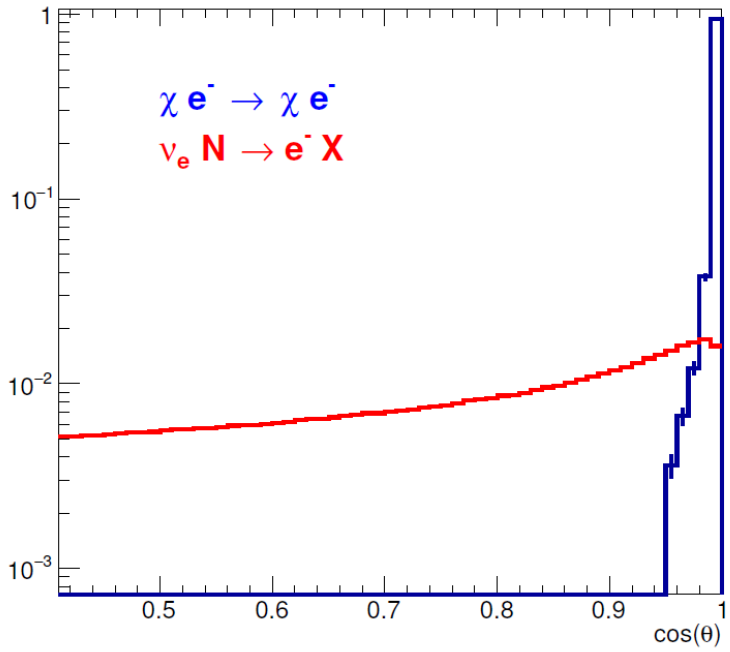

Figure 4.4: Scattered electron angle distribution for the signal ($e^-\chi \to e^-\chi$) and ν_e CC background ($\nu_e N \to e^- X$) reactions. The two histograms have been scaled to the same unitary area.

For each neutrino impinging on the detector, an interaction with Cs(Tl) crystals was forced and both the total interaction cross-section and the kinematics of secondary particles from the reaction were saved on an event-by-event basis, to allow the subsequent simulation of the detector response. To speed-up calculation, only neutrinos with energy greater than 100 MeV were considered -the cut-off still being lower than the foreseen detection threshold (see next sections). Different neutrino flavors give rise to different processes (and different secondary particles); the implications for the $\chi - e$ signal measurement for different neutrino flavors interactions are listed below:

- $\nu_e N \to eX$: **this is the most critical background source for the experiment**, since the CC interaction could produce a high energy electron into the detector that mimics the signal. This background can be reduced considering again the different kinematics of the ν interaction with respect to the $\chi-$electron scattering. The significant difference in the polar angle of the scattered electron (with respect to the beam direction) allows to define a selection cut to identify and separate ν_e from the χ. This difference is shown in Fig. 4.4, which reports the angular distribution of scattered e^- from ν_e CC, compared to the characteristics kinematics of the $\chi e^- \to \chi e^-$ process.

- $\nu_\mu N \to \mu X$: the CC interaction produces a muon in the final state (beside the hadronic state X). Since the muon usually exits the calorimeter hitting the veto layers, this reaction can be identified and therefore this background can be rejected with high efficiency.

- $\nu_\mu N \to \nu_\mu X$ the NC interaction produces an hadronic state X that may interact in the detector (while the scattered neutrino escapes from detection). This can mimic an EM shower if π_0 are produced. However, due to the difference in mass, the scattered ν carries most of the available energy providing a small transfer to the hadronic system and therefore reducing the probability of an over-threshold energy deposition.

- $\nu_e N \to \nu_e X$: same considerations as above.

All the interaction mechanisms described above have been included in the simulations, thus accounting for their possible contribution to the total background yield.

4.2.3 Detector Response To ν Events

Following the same procedure adopted for the signal detection efficiency calculation, we performed a GEANT4-based simulation of the BDX detector response to secondary par-

Energy threshold (MeV)	Expected counts (285 days measurement)
200	740 ± 300
250	57 ± 25
300	4.7 ± 2.2
350	0.037 ± 0.022

Table 4.1: Number of expected cosmic background events as a function of the single crystal energy threshold.

ticles produced by ν interactions. A different simulation was performed for each detector variation studied (see Sec. 4.4). The number of neutrino-induced background events depends on the choice of the selection cuts, other than the detector setup. These have to be tuned by coherently looking at the effect on the signal efficiency and on the background rejection. For the optimized experimental configuration there described, the number of expected neutrino events is ~ 5.

4.3 Cosmic Background

As described in Ch. 2.3, the projections for cosmic background events have been obtained from the measurement of the prototype detector BDX-PROTO at LNS Catania. BDX-PROTO, a single CsI(Tl) crystal enclosed into two scintillating veto layers and a lead shielding, measured cosmic background in a configuration similar to that proposed for the BDX experiment, in a $\sim$ 1 month long measurement. The expected number of cosmic events as a function of the energy threshold was extrapolated from the spectrum of events in anti-coincidence with both vetos measured with the prototype (see Tab. 4.1). This study proves that, with an an energy threshold of about 350 MeV, no cosmic background event is expected for the full BDX measurement run.

4.4 Optimization Procedure

4.4.1 Detector and Cuts Optimization

The nominal concept of the BDX detector, proposed in [26], features an electromagnetic calorimeter made of $\sim$ 800 CsI(Tl) crystals ($5 \times 5 \times 30$ cm^3 each), for a total volume of order $1 \sim$ m^3. The calorimeter is enclosed within two active veto layers made of plastic scintillators; in this nominal setup, a 5 cm thick lead layer is placed between the two vetos (see Fig. 4.5). To optimize this design I tested two new configurations, slightly

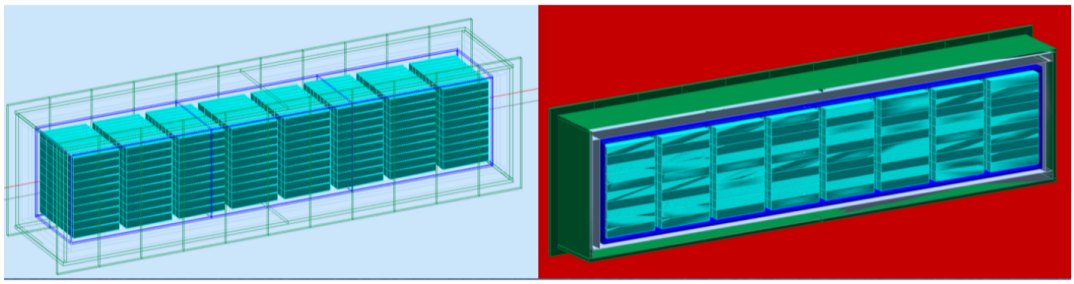

Figure 4.5: A GEANT4 implementation of the original concept of the BDX detector, as proposed in REF Proposal. On the right, the Outer Veto is shown in green, the Inner Veto in blue, the lead in gray and the crystals in cyan.

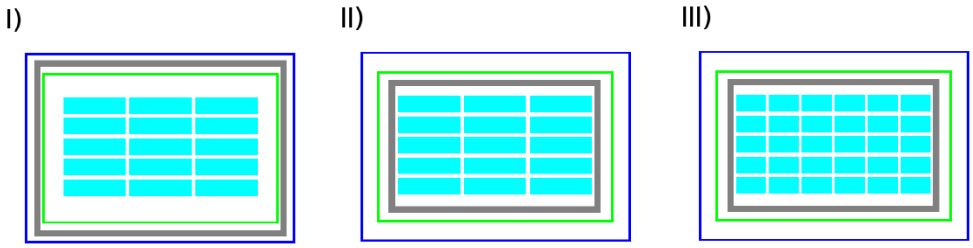

Figure 4.6: Schematic of the three detector configurations tested (lateral view): I) nominal, II) inner lead, III) inner lead, half length crystals. Crystals are drawn in cyan, internal veto in green, external veto in blue and lead in gray.

varying the components arrangement (see Fig. 4.6), without changing the total active volume foreseen in the BDX proposal. In the first setup tested, the lead shielding was moved inside the internal veto layer. This arrangement was motivated by the observation that, in the nominal configuration, electromagnetic shower produced by $\chi - e$ interaction would hit the internal veto resulting in a low signal efficiency. The second setup consisted in reducing the crystals size by a factor of 2 (from 30 cm to 15 cm in length). The rational behind this choice is that an increased calorimeter segmentation provides higher background rejection capability. For each detector setup, signal and neutrino background were simulated, and events were reconstructed and analyzed applying different sets of selection cuts. In particular, the effect of cuts on four different measurable quantities was investigated.

- **Seed energy E_{seed}:** the highest energy measured in a single crystal within one module[1].
- **Module energy E_M:** total energy measured in one module.
- **Number of hits N_{hits}**: number of crystals hit in a module per event. The minimum detection threshold for crystal hits has been set to 20 MeV.
- **Shower transverse dimension R:** quantity indicating the shower deviation from the beam direction[2]. It is defined as follows:

$$R^2 = \frac{\sum_{i=1}^{N_{hits}} w_i X_i^2 - \left(\sum_{i=1}^{N_{hits}} w_i X_i\right)^2}{\sum_{i=1}^{N_{hits}} w_i} + \frac{\sum_{i=1}^{N_{hits}} w_i Y_i^2 - \left(\sum_{i=1}^{N_{hits}} w_i Y_i\right)^2}{\sum_{i=1}^{N_{hits}} w_i}.$$

  Here i runs over the crystals hit in the module, X_i and Y_i are the geometrical indexes of each crystal and w_i is a weight factor accounting for the energy of the i-th hit E_i:

$$w_i = max\left[0, 3.1 + ln(E_i/E_M)\right]$$

  the logarithmic factor preventing from overestimating the contribution of the low energy tails of the electromagnetic shower.

An event passed the selection if at least one of the modules of the calorimeter fulfilled the cuts. The effect of different selection cuts on the experiment sensitivity depends not

[1] A module is defined as a 10×10 crystals matrix of the calorimeter, arranged perpendicularly to the beam direction. In the BDX detector (nominal setup), the calorimeter is composed of 8 modules

[2] The quantity R is defined for a single module; if an event hits more than one module, the R value used for event selection is the one of the module with the higher measured energy E_M

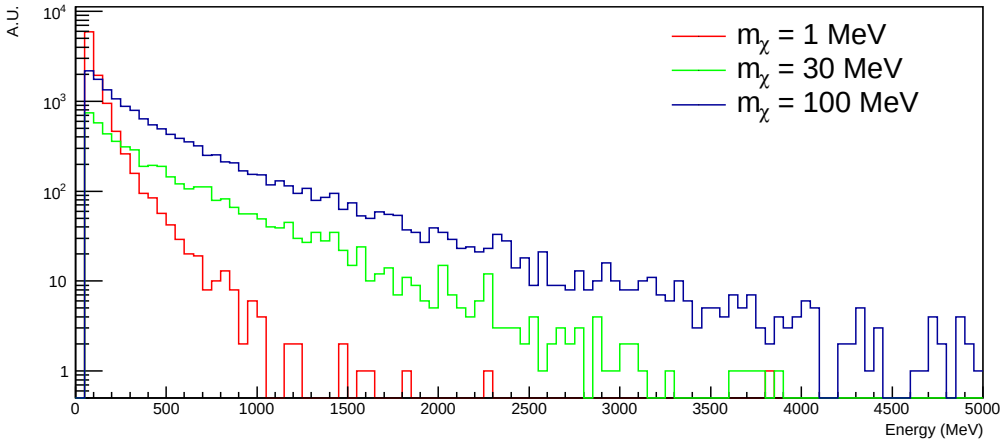

Figure 4.7: Reconstructed E_M distribution for signal, for three different χ mass values: 1 MeV, 30 MeV and 100 MeV. Note that the three distributions have different normalization.

trivially on how cuts affect the signal efficiency and the background rejection capability of a specific detector setup. Being, N_c and N_ν respectively the number of cosmic and neutrino background events and $N_s(m_\chi)$ the number of expected LDM events (for $\varepsilon = 1$), the sensitivity curve $\varepsilon_{min}(m_\chi)$ (for each cuts configuration/detector variation) is given by:

$$\varepsilon^4 = \frac{2.3 * 1.5\sqrt{N_\nu + N_c}}{N_s(m_\chi)}.$$

The optimization of the threshold values for E_{seed}, E_M, N_{hits} and R was performed using a custom code: N_ν and $N_s(m_\chi)$ were estimated through the simulation chain described in the previous sections, varying the threshold values among a large set of configurations; cosmic background events N_c were extrapolated from Tab. 4.1. This process was repeated for different m_χ values in the 1-150 MeV range, in order to obtain the sensitivity curve $\varepsilon_{min}(m_\chi)$ for each cuts set tested and select the optimal one. Note that, being the χ production and $\chi - e$ interaction cross section and kinematics dependent on the χ mass, it is not possible to define an optimal cuts configuration regardless of m_χ. As an example, Fig. 4.7 shows the distributions of E_M for different values of m_χ: for a heavy χ ($m_\chi = 100$ MeV) the distribution features a tail at high energy values, while for a lighter χ ($m_\chi = 1$ MeV) the E_M distribution is peaked at lower energies. As a result, a strong cut on E_M would reduce heavily the sensitivity of BDX in the low χ mass region, less severely affecting it in the high mass region of the parameter space. Optimizing the sensitivity in a given m_χ mass range could therefore affect it in other regions of the LDM parameter space. In this respect, I defined the optimal cuts configuration as the one resulting in the larger

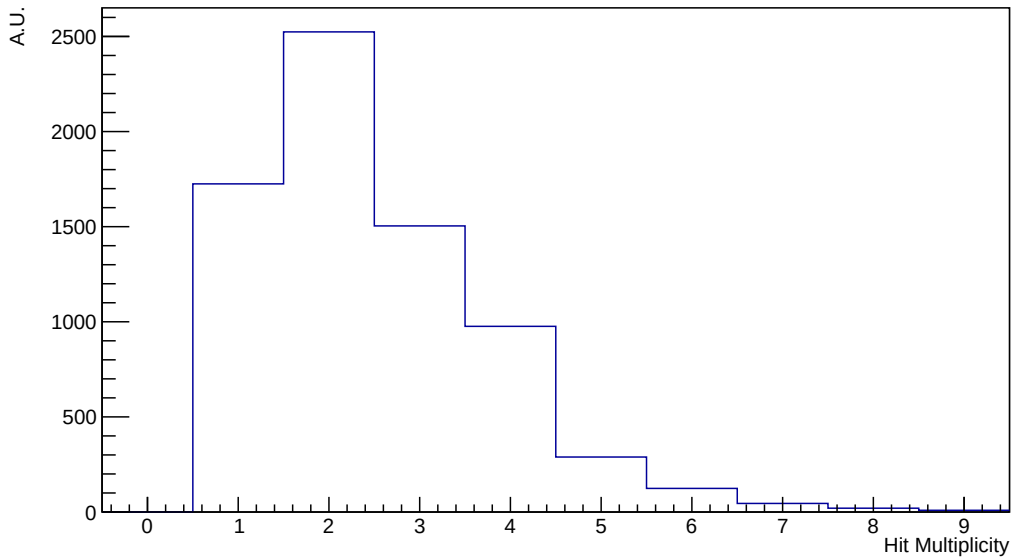

Figure 4.8: Distribution of N_{hits} for signal events ($m_\chi = 10$ MeV). A non-negligible fraction of events produces a single cristal hit.

explored space in the overall $\varepsilon - m_\chi$ plane. This prescription can be changed, in case of future indications (e.g. observed anomalies in other experiments) directing the search in specific regions of the LDM parameter space.

4.4.2 Results of the Optimization Procedure

Among all configurations tested, the set of cuts giving the best reach, for any detector setups, is the following:

$$E_{seed} > 350\ MeV;\ R < 0.6,$$

with no prescription on N_{hits} and E_M. This result reflects the fact that, for both signal and ν background a relevant fraction of events produces a single crystal hit with high energy (see Fig. 4.8), which makes ineffective any cut on the hit multiplicity. It should be noticed, however, that for all events with more than one hit in a single module, the cut on the variable R provides an efficient rejection of ν_e background, because of the different kinematics between χ and ν_e interactions in the detector (see previous sections). Figure 4.9 shows that the selection cut $R < 0.6$ allows to reduce significantly the ν_e background without affecting the signal detection efficiency. Regarding the detector setup, results confirm that the arrangement with the lead shielding placed within both veto layers provides a better efficiency for signal, up to a factor 2 for large m_χ values. This translates

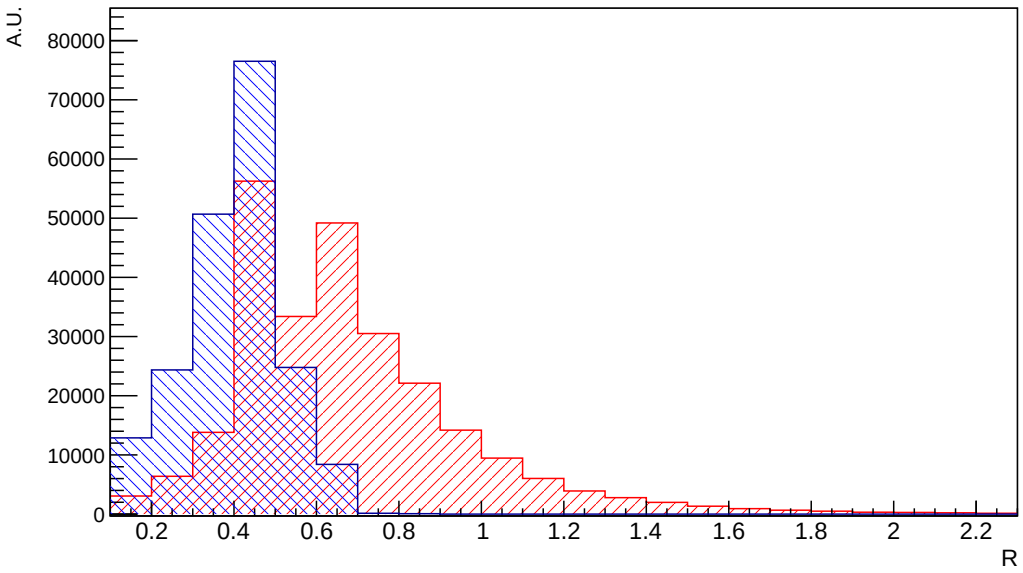

Figure 4.9: Distribution of the variable R for ν_e background events (red) and signal (blue), for $m_\chi = 10$ MeV. Note that the histograms have different normalizations.

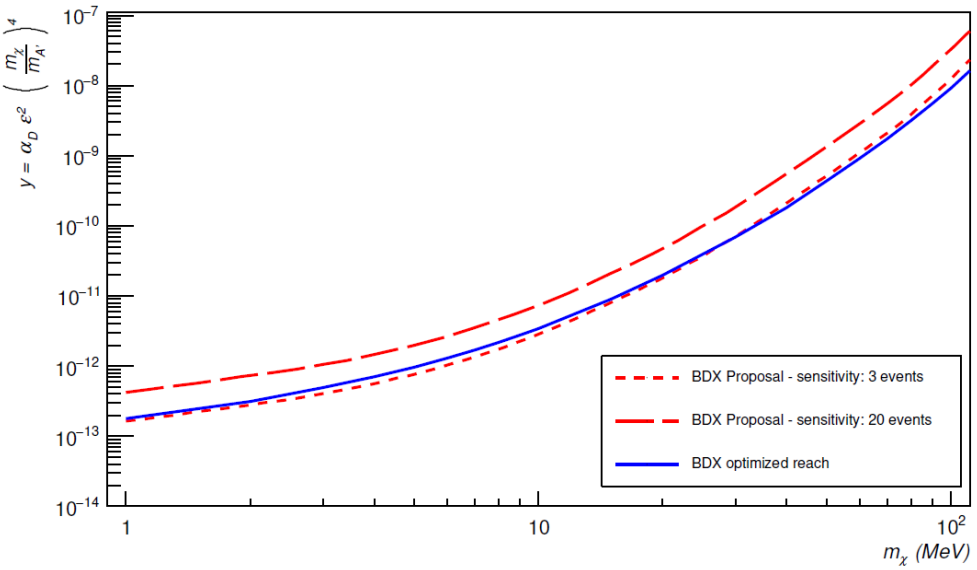

Figure 4.10: Comparison between BDX reach with optimized cuts and detector configuration (inner lead, nominal crystals dimensions) and the reach proposed in the BDX Proposal, for an assumed sensitivity of 3 and 20 events. Here $y = \alpha_D \epsilon^2 \left(m_\chi / m_{A'}\right)^4$, with $\alpha_D = 0.5$, $m_{A'} = 3m_\chi$.

in a clear improvement on the reach. On the other hand, the detector setup with higher segmentation in the calorimeter (crystals length reduced by a factor 2) do not produce a relevant improvement in the experiment sensitivity. In fact, despite the reduced crystal length, the majority of signal and neutrino events affects only a single module of the calorimeter. To increase significantly the background rejection capability of the detector, a much finer segmentation would be necessary, requiring a substantial increase of the number of channels of the calorimeter. In conclusion, *the setup with internal lead shielding and full size crystals is the best option for the experiment.* The detection efficiency for signal events in this configuration is of order of $10\% - 40\%$, depending on the χ mass. This value accounts for both selection cuts and edge effects: as previously mentioned, signal events happening in the outermost crystals have a lower reconstruction efficiency due to the badly contained electromagnetic shower. The number of expected background events is $B \sim 5$ (all due to neutrinos), which corresponds to a sensitivity s of ~ 6 events for signal. Fig. 4.10 shows BDX reach in the $y - m_\chi$ plane, compared to the reach quoted in the BDX proposal [26]. The proposal curves had been derived with the assumption of a 20% signal efficiency and a sensitivity s in the range of 3-20 events. Red dashed lines correspond to the extremes of this interval. The reach obtained with the optimization process described in this section (blue solid line) is comparable to that quoted in the proposal for the most favorable hypothesis $s = 3$; this proves the robustness of the assumptions made in [26].

Chapter 5

BDX-MINI

In the previous two chapters I presented the BDX-HODO measurements (Ch. 3) and the BDX setup optimization (Ch. 4). These works were a fundamental step towards the full approval of the experiment. After the approval of BDX by PAC46, the collaboration decided to construct a small-scale prototype, called BDX-MINI, in order to perform a first physics measurement exploiting the already-existing infrastructure built for BDX-HODO, paving the road toward the full experiment. This pilot measurement is currently ongoing at JLab.

The BDX-MINI detector, composed of an electromagnetic calorimeter (ECal) made of $PbWO_4$ crystals ($\sim 4\times10^{-3}$ m^3 total volume) and two layers of active veto made of plastic scintillator, was placed downstream of the Hall-A beam-dump, in the well previously dug for the BDX-HODO test, without any specific shielding installed upstream. The measurement is being performed with a 2.2 GeV electron beam from CEBAF, with a current up to 150 μA, allowing to collect $\sim 5 \times 10^{21}$ EOT in a $\sim$ three months beam-on run. The LDM production and detection mechanisms are the same as those described in Sec. 2.1 for the full BDX experiment: χ particles are produced from the interaction of the electron beam in the beam-dump, travel across the concrete bunker up to BDX-MINI, where they can scatter with the atomic electrons in the $PbWO_4$ crystals. The expected signal is an electromagnetic shower in the ECal, with energy of order of approximately 300 MeV, paired with null activity in the active veto system.

This test is a critical step towards the realization of BDX, proving the potential of an electron beam-dump experiment using CEBAF beam and providing a definitive validation of the experimental technique chosen for BDX. Moreover, *BDX-MINI is the first modern beam-dump experiment searching for LDM particles with an electron beam.* However, given the small detector dimensions and the lower beam energy (compared to the 11 GeV

beam foreseen for BDX), BDX-MINI projected sensitivity touches the limits of already performed experiments, namely E137, with a very limited new discovery potential.

In this section the detector calibration with cosmic rays and the reach estimate of the experiment are reported. The results of this work are reported in the following sections, after an introductory description of the experimental setup.

5.1 Experimental Setup

The BDX-MINI detector was lowered in the well denominated Well-1, previously used for the BDX-HODO measurement (see Ch. 3.1). A tent was placed on top of the opening of the well, allowing for the installation of BDX-MINI DAQ and trigger system (see following section). The main differences with respect to the setup proposed for BDX are the following: firstly, the iron block shielding between the Hall-A concrete bunker and the detector location is not present; only dirt shields the detector from SM particles (muons, neutrons, etc.) exiting the bunker. As seen in Ch. 2.3, the iron shielding is critical for the full BDX experiment, since the 11 GeV electron beam used produces in the beam-dump a significant flux of high energy penetrating particles that, without shielding, can reach the detector producing a background. However, for the BDX-MINI test the absence of the iron blocks is not a problem: given the low energy of the beam used for this test, the 14 m of dirt between the bunker and Well-1 are sufficient to range out all SM particles produced in the dump (except for neutrinos[1]). Secondly, no concrete overburden is present on top of the detector location, resulting in a higher cosmic particle flux hitting the detector, which translates in a higher cosmic background rate. Therefore, in terms of cosmic background, BDX-MINI setup would provide conservative limits with respect to BDX. This makes the implementation of an efficient veto system, allowing for an effective rejection of cosmic background events, a critical aspect of the measurement.

5.1.1 The BDX-MINI Detector

BDX-MINI was built and tested at the INFN-Genova laboratories. Figure 5.1 shows the different phases of the assembly procedure. In the picture the detector components are shown: the core of the detector is a compact ECal made of $PbWO_4$, surrounded by a tungsten (W) shielding shaped as a prism with an octagonal base. The Ecal and W shielding are enclosed in two veto layers made of plastic scintillator called Inner Veto (IV)

[1] We performed an analytical calculation to estimate the number of ν hitting the detector. Given the 2.2 GeV beam and the BDX-MINI detector volume, no neutrino background event is expected for the measurement run, assuming an energy threshold of about 300 MeV.

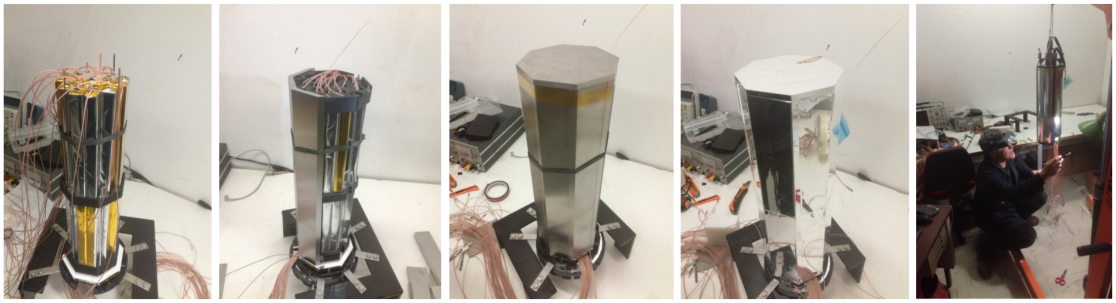

Figure 5.1: Pictures show the assembly of the BDX-MINI detector. The different components of the detector are visible; from left to right: the $PbWO^4$ crystals composing the electromagnetic calorimeter, the tungsten shielding, the innner and outer veto systems (both the crystals and vetos are wrapped in reflecting mylar).

and Outer Veto (OV), respectively. The detector was placed in the same stainless steel, water-proof, cylindrical vessel used for BDX-HODO and lowered in the well using the same hand winches system described in Sec. 3.1. Both the crystals and the vetos are readout with Hamamatsu 6×6 SiPM. The SiPMs are connected to custom amplifiers ([26]) via $\sim$ 12 m long 3M cables. These cable were passed through water-tight PVC pipes, as the detector was lowered to the beam height in the well. A thorough description of the BDX-MINI components is given in the following paragraphs.

Electromagnetic Calorimeter The ECal is the core of the detector. Given the limited volume available in the well (the well radius is $\sim$ 6 cm) we decided to use $PbWO_4$ as a scintillator material. Lead tungstate, despite the lower light yield, is in fact denser than cesium iodide (8.28 $\frac{g}{cm^3}$ compared to 4.51 $\frac{g}{cm^3}$), providing a larger active mass for the same volume. Sixty $PbWO_4$ crystals compose the ECal, for a total volume of 3.68×10^{-3} m^3, which makes the $\sim 0.85\%$ of the BDX detector active material. The crystals have parallelepipedal shape with different dimensions: 28 crystals, called PANDA since they are spare of PANDA ECal, measure $(2 \times 2 \times 20)$ cm^3. The remaining 32, called FT being spares from the CLAS12 Forward Tagger, are sightly smaller, measuring $(2 \times 2 \times 20)$ cm^3. Figure 5.2 shows the PANDA and FT crystals used. As already mentioned, for the ECal readout we used 6×6 mm^2 Hamamatsu SiPMs. Each PANDA crystal is coupled to a SiPM , placed on the small face. In order to contain the number of readout channels, we paired the 32 FT crystals in pairs, using optical glue on the crystals long side to obtain a single optical channel. The resulting 16 compound crystals, measuring $(3 \times 1.5 \times 20)$ cm^3 are readout with a SiPM coupled to the small face, placed on the junction between the two

Figure 5.2: Pictures show the crystals used for the BDX-MINI ECal, wrapped in reflecting mylar to enhance light collection. FT crystals, showed in the left picture, are glued in couples, to contain the number of channel of the ECal.

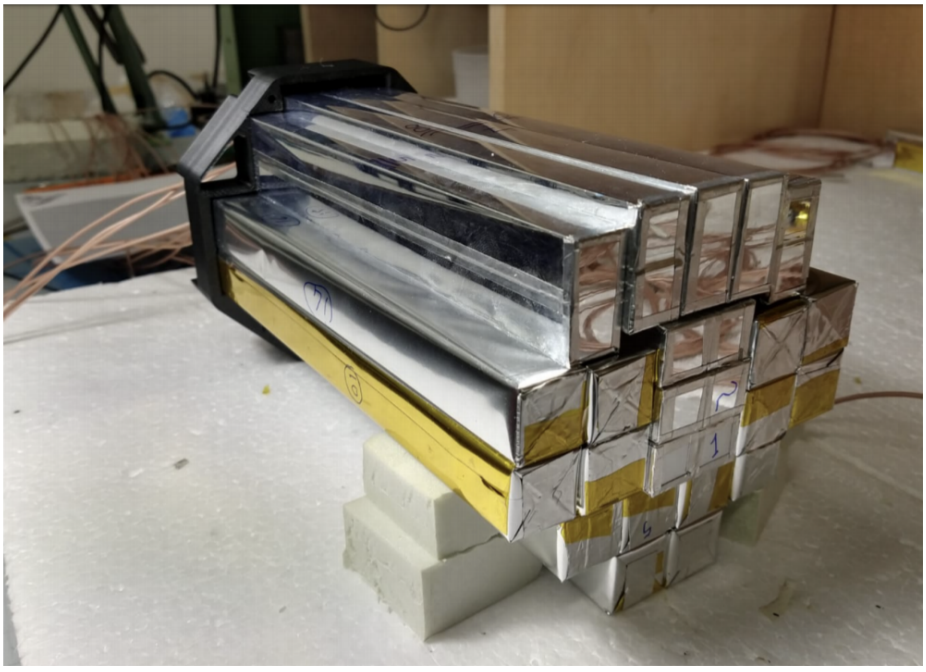

Figure 5.3: Lower module of the BDX-MINI ECal. Crystals are held in place by the black plastic mechanical support.

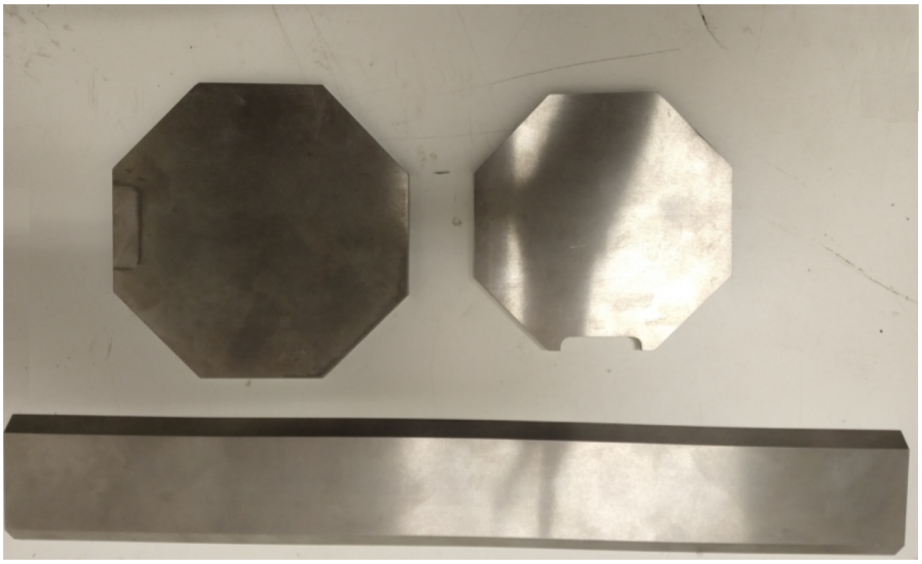

Figure 5.4: The picture shows the components of the W layer enclosing the ECal: the 2 octagonal plates forming the shielding base and one of the bars composing the lateral surface.

glued crystals. This configuration was validated with a measurement performed at INFN-Genova laboratory: the light yield of the compound crystals was measured using cosmic rays and compared to the light yield of single PANDA crystals, resulting in negligible differences.

The BDX-MINI ECal is composed of two modules, each made by 14 PANDA and 8 compound FT crystals, arranged in an approximately cylindrical shape (see Fig. 5.3). A 3D-printed plastic mechanical support holds crystals in place. The two modules are mounted one on top of the other, resulting in a ∼40 cm long, ∼ 11.5 cm wide cylinder-like footprint.

Tungsten Shielding The ECal is enclosed in a 0.8 cm thick tungsten shielding. The purpose of this layer is to shield the vetos from the electromagnetic shower initiated inside the ECal by χ particles hitting the detector.Given the small dimension of the detector, the shower is not fully contained in the ECal, which makes necessary to install an absorber between the ECal and the veto system, in order to avoid the rejection of signal events. The available volume for the absorber layer is limited, therefore we decided to use tungsten: being denser than lead ($\rho_W = 19.28 \frac{g}{cm^3}$), it provides a higher stopping power for the same thickness. The W shielding is shaped as an octagonal prism, with length $l = 45$ cm and

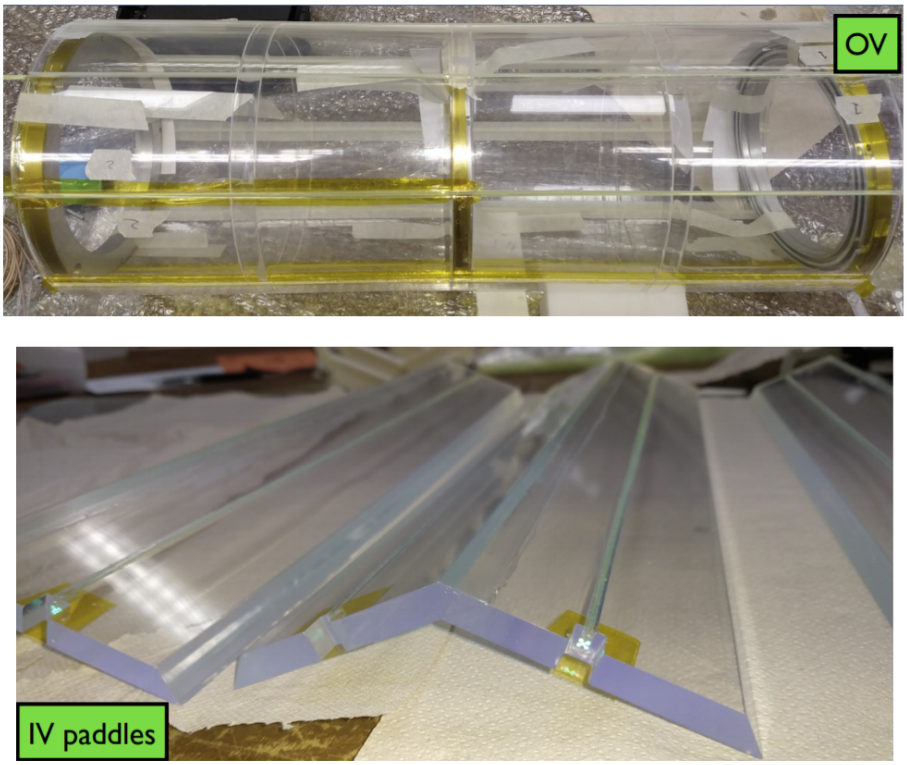

Figure 5.5: top) The OV cylinder. The grooves for the WLS fibers are clearly visible. bottom) Scintillator bars forming the IV lateral surface, before the assembly.

base side 5 cm. It is composed of 10 separate parts: two octagonal plates form the prism upper and lower basis, while the lateral surface is made of 8 bars, as shown Fig. 5.4. In one of the octagonal plates a small open slot allows the passage of the ECal signal cables.

Veto System The Ecal and tungsten shielding are enclosed in two veto layers, made of 0.8 cm thick EJ200 plastic scintillator. The inner layer, called IV, has an octagonal prism shape, with base side 6.2 cm and 49.4 cm long. It is composed two octagonal caps (IV_{top}, IV_{bottom}) and 8 bars forming the lateral surface of the prism. The bars are coupled togother with optical glue, in order to obtain an optically continuous piece (see Fig. 5.5 for a picture of the IV scintillator bars), called IV_{oct}. The outer layer, or OV, has a cylindrical shape with radius 9.7 cm and 53.0 cm long. It is formed by two round caps (OV_{top}, OV_{bottom}) and a single 0.8 cm thick cylindrical tube (called OV_{cyl}). (see Fig. 5.5). The caps of both the IV and OV are readout via SiPM glued to the scintillator surface. The octagonal prism and the cylinder feature 8 equally spaced grooves each, running along the length of the two scintillator pieces. Each groove hosts 4 Wavelength Shifter (WLS) fibers (∼1 mm in

diameter), conveying the scintillation light to a SiPM. In this configuration, both the IV octagonal prism and the OV cylinder have a redundant readout of 8 SiPMs each.

DAQ The 64 SiPMs of the BDX-MINI detector (44 channels from the ECal and 20 from the vetos) are connected via 12 m long 3M cables to boards hosting custom amplifiers (with the same design of those used for the BDX-HODO measurement) and 1:1 splitters based on a passive resistor network. One half of the signal is sent to a leading edge discriminator (CAEN v895), the other half is fed to a Flash Amplitude-to-Digital Converter (CAEN FADC v1725). The digital output from the discriminator is sent to a programmable logic board (CAEN FPGA v1495) implementing the trigger logic and generating the trigger for the FADC. All the boards of the readout system are hosted in a VME64x crate. The global trigger implemented in the FPGA of the v1495 module is the OR of all the crystals of the ECal.

5.2 BDX-MINI Energy Calibration

After a first test at INFN-Sezione di Genova, the BDX-MINI detector was dismounted and sent to JLab, where, during the spring of 2019, it was reassembled and then lowered in Well-1 at about 7.5 m below the ground level, in the foreseen position for the beam-on measurement, currently being performed. In this configuration, during summer 2019, a cosmic rays measurement run was performed. The BDX-MINI data analysis is performed within the already mentioned "JLab Data Analysis Framework" (JANA). For the crystals composing the ECal, the charge is obtained by integrating the signal waveform in a 1 μs time window; for the IV and OV, since they are not meant for energy measurement but to detect MIPs in order to veto events, the amplitude of the waveform is used. Cosmic data taken during summer of 2019 were used to obtain the energy calibration of the detector. The BDX-MINI geometry and response were implemented in GEANT4 via the GEMC interface and Monte Carlo simulations of cosmic muons hitting the detector were performed; in order to get the energy calibration constants the results of simulations were compared with cosmic data. In the following sections the calibration procedure is described in detail.

5.2.1 Cosmic Simulations

BDX-MINI implementation in GEMC In order to calibrate the detector, a realistic MC simulation of cosmic rays was performed. The geometry of the test location (including the dirt and the well) and the detector components were implemented in GEMC-GEANT4

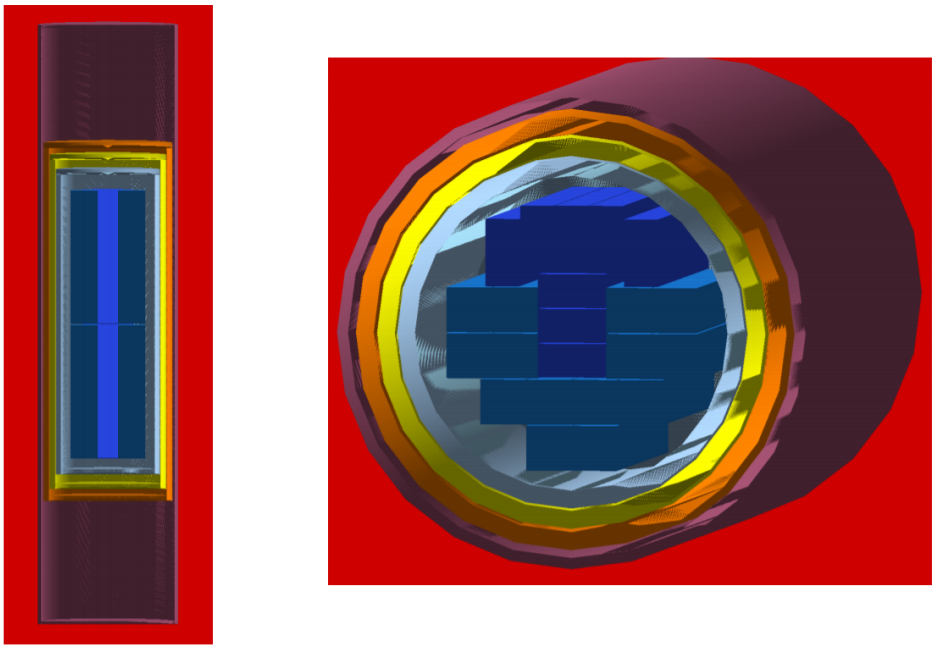

Figure 5.6: BDX-MINI implementation in GEMC, side view (left) and section view (right). The crystals are shown in blue, the tungsten shielding in gray, the IV and OV in yellow and orange respectively, and the stainless steel vessel containing the detector is depicted in purple. Note that the tungsten shielding and the IV have been approximated as cylinders.

(see Fig. 5.6 for the GEMC implementation of BDX-MINI). For each muon hitting the detector, the simulations returned the energy (in MeV) released in each crystal of the ECal, and the number of *phe* collected by the SiPMs reading out the the IV and OV components. For the IV and OV lateral surfaces (OV_{cyl} and IV_{oct}), since they are large scintillators with multiple readout, I implemented in the simulations an effective formula taking into account the light propagation effect for each of the 8 readout channels, as a function of the muon hit position on the scintillator (see Sec. 5.3).

Muon generator As described in the following section, in order to perform the energy calibration it is necessary to identify certain muon trajectories resulting in a fixed path inside the detector, making possible a data-simulation comparison. Therefore, a realistic cosmic muon generation is critical for the calibration of BDX-MINI. The cosmic muons energy spectrum and angular distribution reported in [68] were implemented directly in GEMC. Cosmic particles were generated in a fiducial volume big enough to contain the detector and a careful normalization has been performed to correctly take into account the crossing on the lateral sides. Particles found to cross the fiducial volume where then projected far away and the production vertex extracted outside the dirt. Generating muons at large distance from the sampling surface allows to account for the dirt effect: muons may in fact undergo a significant multiple scattering and produce secondary particles in the dirt surrounding the detector.

5.2.2 Crystals Calibration

As mentioned above, the crystals energy calibration is performed comparing the measured charge to the simulated energy deposition by muons. Most of cosmic muons are MIPs, crossing the crystal with an approximately straight trajctory. It is therefore necessary to select, both in data and simulations, trajectories resulting in well defined path lengths in the crystals. If the muons path in a crystal is fixed, the resulting energy/charge distributions feature a Landau peak, whose position can be used for the calibration. To define such trajectories, the veto system was used.

I observed that, when a muon hits the OV lateral surface (OV_{cyl}), the scintillation light detected by the 8 SiPMs is strongly dependent on the muon hit position on the cylinder. As expected, the SiPMs coupled to the WLS fibers closer to the hit position collect considerably more light than the others. This behavior allows to roughly identify the impact position of a muon on the OV_{cyl} (more precisely the azimuth angle of the impact point, with respect to the cylinder axis): the SiPM collecting the largest number of photo-electrons in a cosmic event indicates that the muon crossed the scintillator near

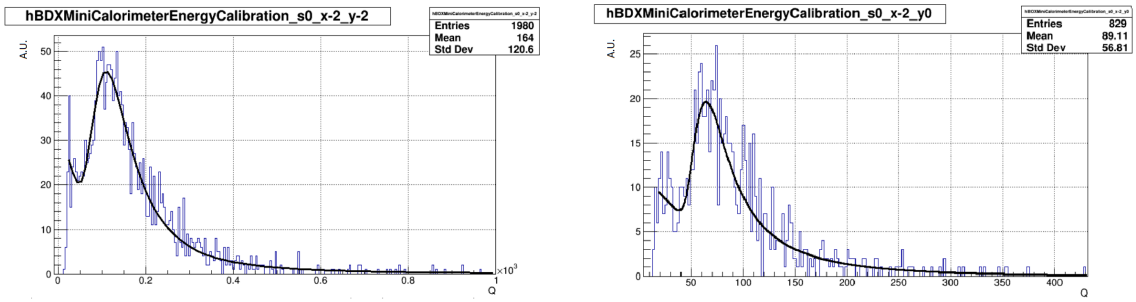

Figure 5.7: Measured charge spectra (expressed in *phe*) of the (-2,-2) and (0,-2) crystals, for events satisfying the conditions described in the text. The Landau peak is clearly visible. Here the distribution are fitted with a Landau curve plus a polynomial curve for background.

the corresponding WLS fiber. This method gives no information on the vertical position of the hit; however, this can be roughly fixed asking for the coincidence/anticoincidence of the vetos top and bottom caps. The IV lateral surface (the IV_{oct}), being an optically continuous piece as the OV_{cyl}, presents a similar behavior. This observation was used to select trajectories and define a set of requirements on the IV and OV channels, including the IV and OV caps. An effective formula for the light propagation in OV_{cyl} and IV_{oct} (see next section) was included in the GEANT4 simulation of the detector, so that the same selection could be applied to the simulated events. As an example, a defined set of trajectories can be chosen asking for the coincidence of the IV_{oct}, the IV top cap and the anticoincidence of the IV bottom cap, with the additional request of the SiPM 2 of the IV_{oct} (see Fig. 5.8) collecting the largest number of photoelectrons among the other SiPMs. Figure 5.7 shows the measured charge distribution of the crystals (-2,-2) and (-2,0) of the ECal upper half, for events satisfying the aforementioned requests (the coordinates indicates the position of the crystals in the ECal, following the scheme showed in Fig. 5.8). The Landau peak is clearly visible, making possible to extract a calibration constant using simulations. To pratically perform the calibration I used the RooFit toolkit [69], using the following procedure:

- For each crystal, a combination of coincidences of the IV and OV components selsecting a muon trajectory crossing the crystal was identified.

- The cosmic muon flux was simulated with GEANT4 and the distribution of the energy released in the crystal was sampled, for events satisfying the same vetos coincidences set. The sampled distribution was then used to build a PDF (Probability

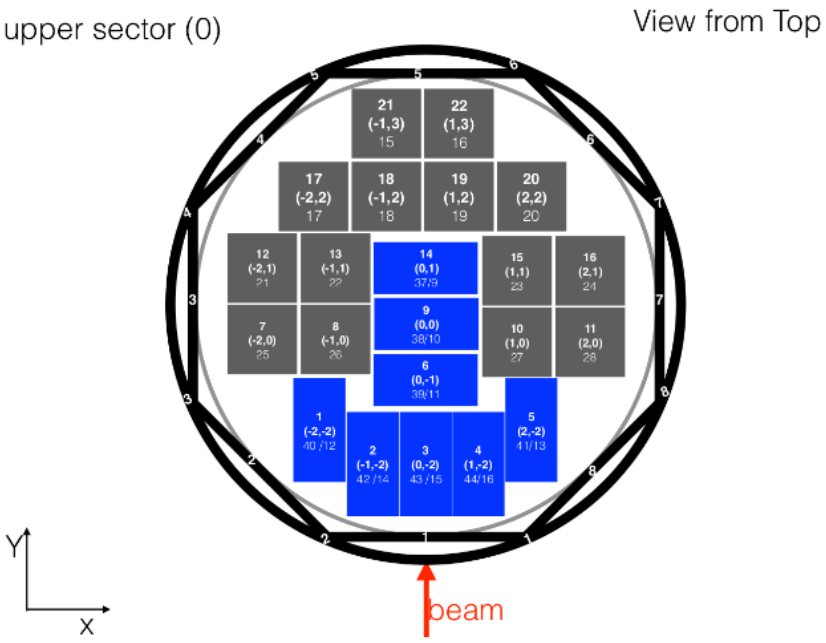

Figure 5.8: Scheme representing the crystals arrangement in the ECal top half (top view). The OV_{cyl} and IV_{oct} enclosing the ECal are depicted in black; the SIPMs reading the two scintillators are identified by numbers from 1 to 8.

Density Function) in RooFit.

- Using RooFit, the measured charge distribution of the crystal (for the same event selection) was fitted with the simulated PDF of the energy, scaled with a free parameter. The value of this parameter returned by the fit is the calibration constant realizing the charge-to-energy conversion.

This procedure was repeated for all the 44 crystals of the ECal, obtaining a set of calibration constants. These parameters were included in the JANA reconstruction software of BDX-MINI, allowing for an event-by-event reconstruction of the energy released in the ECal.

5.3 Vetos Characterization

The characterization of the vetos behavior is particularly important for BDX-MINI, both because vetos are used for the ECal calibration (as explained above) and because an accurate simulation of the vetos is necessary to determine the efficiency of BDX-MINI to LDM, as explained in the following sections. The characterization of the top and bottom caps of the IV and OV was performed selecting vertical muon trajectories imposing the coincidence of in-line crystals of the ECal. The signal amplitude distribution for such events was measured and used to implement a realistic response in the BDX-MINI simulation framework.

The characterization of the scintillators forming the lateral surfaces of the IV and OV (the IV_{oct} and OV_{cyl}) was more challenging. These are optically-continuous scintillator pieces with non-trivial shapes and multiple readout. When a charged particle hits the IV_{oct} or OV_{cyl}, scintillation light travels to the WLS fibers, where it is collected and conveyed to SiPMs. As a result, all photo-detectors produce a visible signal, with an amplitude depending on the WLS fibers position with respect to the hit point in the scintillator. In particular, two main effects affect the light transmission to the WLS fibers corresponding to different SiPMs. Firstly, light transmitted in the plastic undergo an exponential attenuation depending on the distance traveled. Given the dimension of the two components, this effect can't be neglected. Secondly, a large fraction of the scintillation photons is absorbed whenever they cross one of the groove containing the WLS fibers. This translates to a discretized light reduction depending on the number of grooves that the scintillation light crosses while propagating from the hit point to the considered SiPM. Note that, being the IV_{oct} and the OV_{cyl} shaped respectively as an hollow octagonal prism and hollow cylinder, light emitted in a given position can reach a WLS fiber both traveling

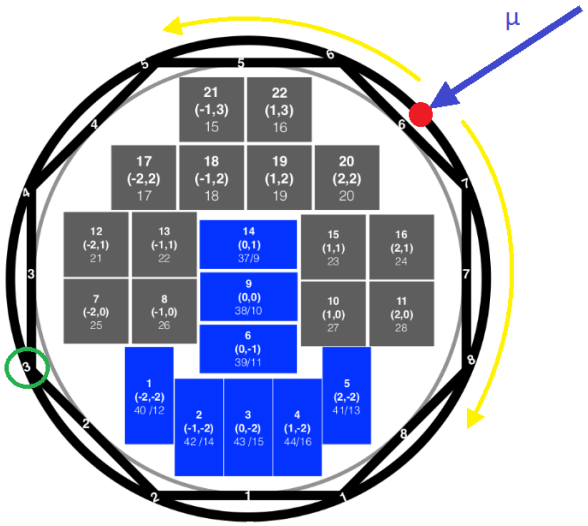

Figure 5.9: Scheme showing the light transmission in the OV_{cyl} (top view). When a cosmic muon hits the OV_{cyl}, scintillation light is emitted from the impact point (red dot in the picture). The generated light then travels through the scintillator both clockwise and anticlockwise. As an example, to reach the WLS fiber coupled to SiPM 3 (in the green circle) light has to cross the grooves containing the other fibers (photons traveling clockwise cross 4 grooves, while light moving anticlockwise crosses 3 grooves).

"clockwise" or "anticlockwise", with respect to the axis of the scintillator (see Fig. 5.9 ref for an explanatory example).

Considering the two aforementioned effects, we found that the following effective formula describes reasonably well the light attenuation in the IV_{oct} or OV_{cyl}, for i-th SiPM:

$$L(\phi)_i = L_{0i} \times \left(F_G^{N_G} \times e^{-\frac{\phi_i}{\phi_{att}}} + F_G^{7-N_G} \times e^{-\frac{360-\phi_i}{\phi_{att}}} \right),$$

where:

- ϕ is the angle between the charged particle hit position and the axis defined by the WLS fiber of the i-th SiPM;
- L_{0i} is the light collected by the i-th fiber when the hit happens in correspondence of the fiber itself;
- F_G is a parameter describing the fraction of scintillation photons absorbed when a single groove is crossed;
- N_G is the number of grooves light has to cross to reach the i-th fiber traveling clockwise looking the scintillator from the top (see Fig. 5.9);
- ϕ_{att} is a parameter defining the light attenuation length in the scintillator, expressed in terms of the azimuth angle covered by scintillation photons[2].

This formula was implemented in the GEMC-GEANT4 description of BDX-MINI, and the parameters F_G and ϕ_{att} were estimated with an iterative procedure, as described below.

In order to evaluate F_G, I used the crystals and veto caps coincidence to select specific muon trajectories allowing to highlight the effect of the light absorption in grooves crossing (see Fig. 5.10 for a representation all the muon trajectories studied). As an example, Fig. 5.11 shows the signal distribution measured by SiPM 2 of the OV_{cyl}, for the set of muon trajectories 19. The distribution presents two distinct peaks. This is due to the fact that muons corresponding to this specific trajectory can hit the OV_{cyl} on the left or on the right of the WLS fiber 1. Depending on this, scintillation photons have to cross 0 or 1 groves to reach the WLS fiber 2, where they are collected and conveyed to SiPM 2. Therefore, from the ratio between the two peaks position, it is possible to estimate the fraction of light absorbed in a groove. I repeated this study for all the SiPMs of the OV_{cyl} and IV_{oct}, using different muon track selections. From this procedure, we obtained a value

[2]The expression of the attenuation length in terms of the angle covered is only approximately correct for the IV_{oct}, since its shape is not cylindrical.

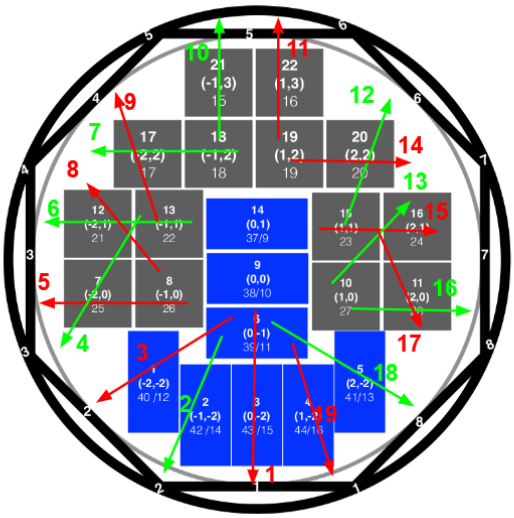

Figure 5.10: The scheme shows the muon tracks (red and green arrows) selected to characterize the response of the OV_{cyl} and IV_{oct}. Each of these trajectories has been selected asking for the coincidence of the top caps of the vetos and two crystals of the ECal, in anticoincidence with the bottom caps. With this selection, muons enter the detector from the top, exiting from the lateral surface in the position defined by the crystals selected for the coincidence.

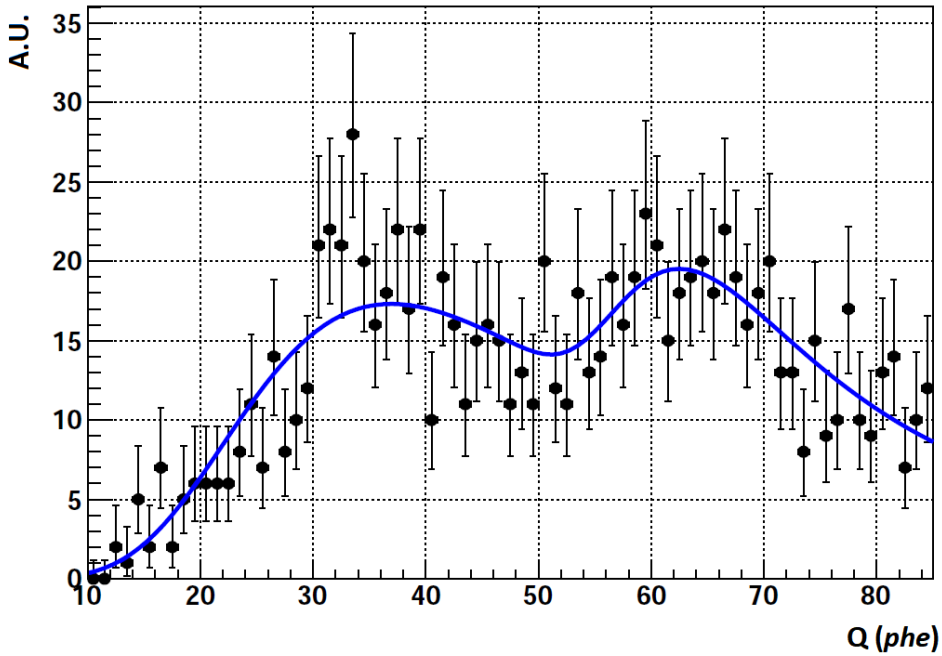

Figure 5.11: The plot shows the signal distribution measured by SiPM 2 of the OV_{cyl}, for the set of muon trajectories 19 (see Fig. 5.10). The two peaks corresponding to the two different event topology are clearly visible.

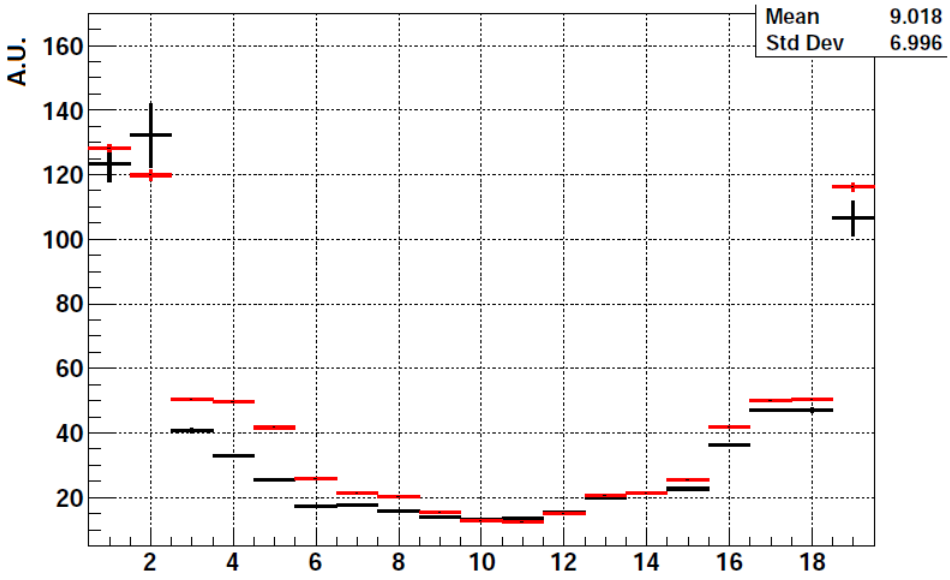

Figure 5.12: Signal peak position of the SiPM 1 of the OV_{cyl} for the different trajectories, data (black) VS simulations (red).

of F_G approximately equal for all grooves:

$$F_G \simeq 0.6.$$

In order to evaluate ϕ_{att}, I implemented this value in the MC response of the vetos and performed a cosmic simulation. Then, from the comparison to data, I tuned the value of ϕ_{att}, until a reasonable agreement between data and simulations was reached. I obtained two different values for the IV_{oct} and the OV_{cyl}, reflecting the different geometry of the two scintillators:

$$\phi_{att\ cyl} = 140^\circ\,;\ \ \phi_{att\ oct} = 120^\circ.$$

Fig. 5.12 shows the obtained result. The plot shows the signal peak position of the SiPM 1 of the OV_{cyl} for the different trajectories showed in Fig. 5.10, data (black) VS simulations (red). Even if the MC tends to slightly overestimate the response for the 3-8 and 12-17 trajectories, the agreement obtained with this modeling appears reasonably good.

5.4 BDX-MINI Sensitivity Estimate

After that the BDX-MINI ECal was calibrated in energy and the vetos response was implemented in the simulation framework, I carried out a first estimate of the experiment sensitivity to LDM. As described in Ch.4, the minimum number of signal events s to which a counting experiment is sensitive is given by the formula:

$$s \simeq 2.3 * 1.5\sqrt{B},$$

where B is the expected number of background events. If $N(\varepsilon, m_\chi)$ is the number of signal events for a given value of the coupling ε and the χ mass m_χ, the minimum ε that BDX-MINI can explore is obtained from the relation:

$$N(\varepsilon_{min}, m_\chi) = 2.3 * 1.5\sqrt{B}.$$

Therefore, in order to evaluate the reach of DBX-MINI, I estimated the expected background rates and simulated the foreseen signal rate as a function of ε and m_χ.

5.4.1 Background Estimate

For the full BDX reach evaluation I had to rely on simulations and on the measurement of BDX-PROTO to assess the experiment background (see Ch. 2). For BDX-MINI, instead, it was possible to directly measure the background contribution during beam-off periods. Given the small detector active volume and the relatively low energy of the beam (2 GeV

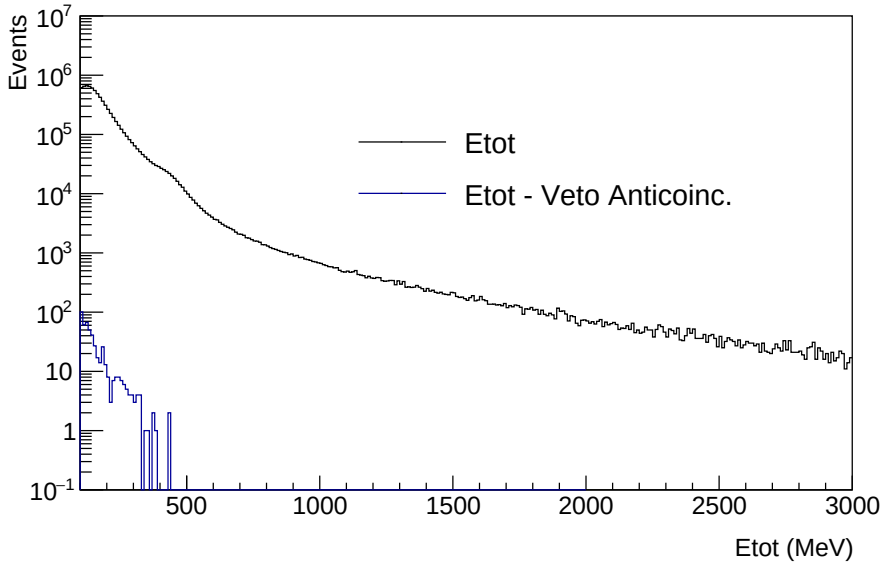

Figure 5.13: Energy distribution of cosmic events measured during the 62 days beam-off run performed at JLab, during the summer of 2019. The histograms shows all events (black) and the events in anticoincidence with the veto system (blue).

compared to the 11 GeV beam foreseen for BDX), no beam-related background is expected. The FLUKA simulations we performed indicate that, even in the current configuration, with only dirt filling the gap between the beam-dump bunker and the BDX-MINI location, no SM particle generated in the dump can reach the detector[3]. Therefore,only cosmogenic particles may produce a background contribution for the experiment. This may happen if a cosmic particle hits the ECal without being detected in the vetos, thus mimicking a LDM signal.

In order to estimate the cosmic background, I analyzed the beam-off measurement performed during the summer of 2019. The data sample considered, consisting in $\sim$ 62 days of data taking, was acquired in the same conditions foreseen for the beam-on run (detector lowered at beam height in Well-1). Being the total length of the cosmic data taking comparable to the duration of beam-on run currently ongoing ($\sim$ 3 months), the background projection made using this set of data is expected to reproduce the background yield foreseen in the BDX-MINI experiment. Figure 5.13 shows the reconstructed energy distribution of events measured by the BDX-MINI during the cosmic run, with no prescription on the vetos (black points) and asking for the anticoincidence of the veto system, both the

[3]The background contribution of neutrinos was estimated with an analytical computation: due to the small dimensions of BDX-MINI and the low beam energy, no ν event is expected to release significant amount of energy in the detector during the whole the measurement run

IV and the OV (blue points). In the data analysis the minimum detectable energy was set to $E_{min} = 10$ MeV for each crystal and the following definition was used for the veto anticoincidence. An event is considered vetoed if:

- At least one of the SiPM signals of the OV or of the IV exceeds a 4 *phe*, threshold, within a time window of 550 ns centered on the trigger time.
- The sum of all SiPM signals of the OV or the IV exceeds a 10 *phe* threshold (only signals occurring in a time window of 550 ns centered on the trigger time are considered).

This definition was selected after some preliminary studies based on both data and simulation, since it allowed to maximize the vetos rejection capability. In addition, it was tested on data collected during a random-trigger run and it resulted in a negligible rate of false positive due to electronic noise. Data shown in Fig 5.13 show the high efficiency of the vetos: when the anticoincidence is requested, no cosmic event with energy higher than 450 MeV is measured (only 2 events with energy higher than 400 MeV were detected).

5.4.2 Signal Rate Evaluation

The evaluation of the signal rate was performed with the same multi-step procedure described in detail in Sec. 4.1 and here summarized:

- The electromagnetic shower initiated in the dump by the 2 GeV electron beam was simulated with GEANT4; the flux of positrons and electrons was sampled at different depths in the dump.
- The χ particles were generated with a modified version of MadGraph4, using the sampled flux of positron and electrons as input.
- The χs propagation to the detector location and the interaction was handled with a custom code, returning a set of scattered electron events in BDX-MINI.
- The response of the detector to the scattered electrons was evaluated through a GEMC-GEANT4 simulation, including the detector geometry and a realistic response of its components (including the parameterized vetos response described in the previous sections).

This procedure was repeated for different values of the χ mass m_χ, keeping fixed the value of the coupling ε to a reference value $\varepsilon_{ref} = 3.87 \times 10^{-4}$. Since the value of ε affects only the number of total events without affecting the χ production and detection

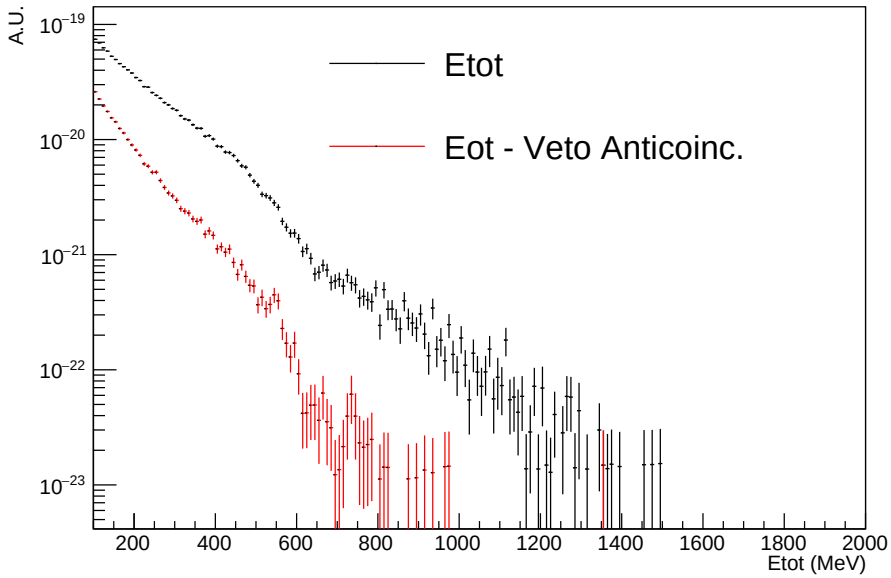

Figure 5.14: Distribution of the total energy released in the ECal by simulated LDM events ($m_\chi = 10$ MeV, $m_{A'} = 30$ MeV). The two histograms represents all events (black markers) and events in anticoincidence with the veto system (red markers)

kinematics, it is not necessary to repeat the simulation varying its value, as explained in Sec. 4.1. Figure 5.14 shows the energy distribution of the simulated signal events for $m_\chi = 10$ MeV, $m_{A'} = 30$ MeV, all the events (black markers) and the events in anticoincidence with the vetos (red markers). Here, I imposed the same anticoincidence definition used in the cosmic data analysis. The plots clearly show that, due to the small detector dimensions, the request of the vetos anticoincidence strongly affects the signal efficiency, because the electromagnetic shower initiated by the scattered electron in LDM events is very likely to hit the IV and OV. This suggests that, for the real data analysis, a more sophisticated vetoing algorithm should be applied, e.g. exploiting the hit position information provided by the IV and the OV.

5.4.3 BDX-MINI Reach

In this section I present the preliminary BDX-MINI reach estimated. Contrary to the BDX optimization presented in Ch.4, for this calculation the signal selection cuts were not optimized; only a rigid cut on the total energy was used to distinguish signal from background events. A systematic study of the BDX-MINI sensitivity dependence on the signal selection is outside the goals of this dissertation and will be performed in future,

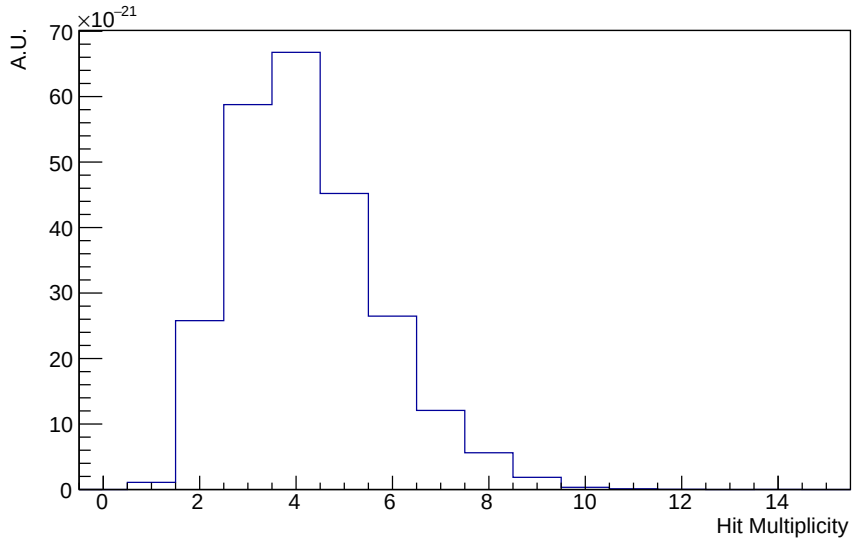

Figure 5.15: Distribution of the number of crystals hit for LDM events ($m_\chi = 10$ MeV, $m_{A'} = 30$ MeV). Here, a crystal is considered hit if it has detected an energy higher than $E_{min} = 10$ MeV.

using data currently being collected in the beam-on measurement. As an example, Fig. 5.15 shows the hit multiplicity (number of crystal hit with energy higher than 20 MeV) for signal events ($m_\chi = 10$ MeV, $m_{A'} = 30$ MeV): the vast majority of events has a multiplicity $N_{hits} > 2$. This suggests that a systematic study of the signal events topology may be carried out, resulting in a refined signal event selection optimizing the reach of the experiment. The result here presented aims to provide a first estimate of the BDX-MINI sensitivity curve. The result of this study is shown in Fig. 5.16. The reach is presented in the $y - m_\chi$ plane, being y defined as $y = \alpha_D \varepsilon^2 (\frac{m_\chi}{m_{A'}})^4$ (the $m_{A'} - m_\chi$ ratio is fixed to 3). For the calculation a collected charge of 5×10^{21} EOT was assumed, with zero background events. The signal rates were evaluated considering three possible energy threshold values, corresponding to the the 3 red curves in the plot: 300 MeV, 400 MeV and 500 MeV. The cosmic measurement analysis suggests that, to reach the zero background level, an energy threshold of ~ 450 MeV must be used. However, for the aforementioned reasons, with a more systematic study will be probably possible to relax this cut using more refined event selection algorithms, resulting in better signal efficiency and background rejection. In this respect the 300 MeV and 400 MeV threshold curves represents a reasonable estimate of the best achievable sensitivity of the experiment, while the 500 MeV curve is more conservative. In any case, despite being a small demonstrator detector, BDX-MINI will achieve a sensitivity comparable, in some regions of the parameter space, to much larger

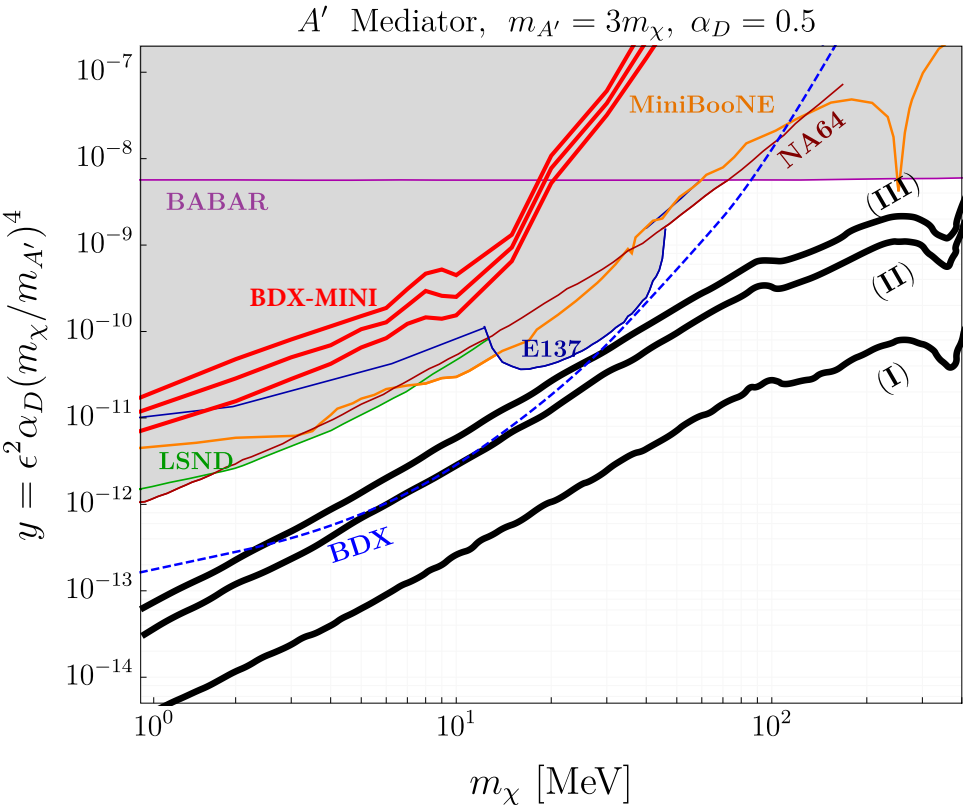

Figure 5.16: Projected reach for BDX mini (red curves), for three different energy threshold values: (from top to bottom) 500 MeV, 400 MeV and 300 MeV. The bump in the reach centered at about $m_\chi = 15$ MeV is due to the contribution of secondary positrons annihilation to the LDM production in the beam-dump.

experimental efforts from the past, such as E137 (see Sec. 1.8).

Chapter 6

Positron Annihilation Contribution To LDM Production

When a high-energy electron impinges on a thick target, such as a beam-dump, it initiates an electromagnetic shower, i.e. a cascade multiparticle production process. The two main reactions contributing to the process are photon production through bremsstrahlung by electrons and positrons and e^+e^- pair production by photons. As a consequence, after a few radiation lengths, the developing shower is made by an admixture of electrons, positrons, and photons, characterized by different energy distributions. As mentioned in Sec. 2.1.1, secondary positrons can contribute significantly to the total LDM yield of beam-dump experiments such as BDX. However, in previous papers describing *Dark Photon* production in electron beam-dump experiments [70], only the A'-strahlung production mechanism by electrons has been included. I performed a study of the contribution of secondary positrons to different electron-beam thick-target experiments searching for LDM (including BDX), both in the visible [4] and invisible [3] A' decay scenario. These works proved that positron effect can't be neglected in the evaluation of the sensitivity of electron beam-dump experiments. This section is focused on the work I carried out in the context of the invisible *Dark Photon* decay scenario, being BDX aimed to explore this paradigm.

To evaluate the A' production by positrons in electron-beam dump-experiment, a multi-step Monte Carlo procedure was employed. Firstly, I evaluated the energy spectrum and the multiplicity of secondary positrons annihilation on atomic electrons in the beam-dump through a GEANT4-based simulation. Secondly, I used a custom code to evaluate the number of χ particles produced by positrons together with their angular and momentum distribution. Then, a custom MC simulation was used to estimate the expected LDM signal rate as a function of ε. The result of this calculation were used to obtain the

sensitivity curves in the LDM parameter space. This procedure was repeated for different experiments, considering the specific experimental setups, described in the following section.

6.1 Studied Experiments

The A' production through secondary positrons is of great interest not only for BDX, but also for all other past and future electron-beam thick-target experiments searching for LDM in the *Dark Photon* scenario. These experiments can be divided in two main categories: passive beam-dump experiments (BDE) such as BDX, and active beam-dump experiment (ABDE). The layout of the typical BDE is presented in Ch.1: an intense primary beam is dumped on a passive thick target followed by a significant amount of shielding material. Beside the cascade of SM particles, electrons or positrons stopped in the beam dump may produce an A' decaying to a $\chi\bar{\chi}$ particle pair, resulting in an effective LDM secondary beam. LDM particles then propagate through the shielding region to the detector. Scattering on the electrons of the detector active material may result in a detectable signal.

Active beam-dump experiments (ABDE), instead, use the active dump as a detector, exploiting the missing energy signature of produced and undetected χ to identify the signal. The active dump, detecting the EM shower, allows to measure the energy of individual leptons of a monochromatic beam, provided the intensity is low enough to have one particle at a time impinging on the detector. When an energetic A' is produced, its (invisible) decay products carry away a significant fraction of the primary beam energy, resulting in a visible defect in the energy deposited in the active dump. Signal events are identified when the missing energy, defined as the difference between the beam energy and the detected energy, exceeds a minimum value E_{miss}^{CUT} .

I calculated the contribution of secondary positron annihilation for the following experiments: E137 [71] and LDMX [72] at SLAC and NA64 at CERN [73], in addition to BDX, which is the focus of my PHD. I also investigated the sensitivity of the same experimental setups replacing the e^- beam with a e^+ beam, to show the unique potential of this production mechanism when an optimized experimental setup is adopted.

E137 E137 is a BDE that ran at SLAC in 1980–1982 searching for long-lived neutral objects which might be produced in the electromagnetic shower initiated by 20 GeV electrons in the SLAC beam dump East. The detector, located at a distance of $\sim$ 378 m from the dump, was an 8-radiation length electromagnetic calorimeter made by a sand-

wich of a 1 cm plastic scintillator paddle and 1 X_0 iron (or aluminum) converters. To satisfy the trigger condition, χ particles should have scattered in the first five layers. A total charge of ~ 30 C was dumped during the live time of the experiment in two slightly different experimental setups, denoted as "E137-I" (~ 10 C dumped) and "E137-II" (~ 20 C dumped). The main difference between the two setups lies in the detector dimensions: the "E137-I" front-face dimension was $2 \times 3\ m^2$, while for the "E137-II" front detector surface was $3 \times 3\ m^2$. The original data analysis searched for axion like particles decaying in e^+e^- pairs, requiring a deposited energy in the calorimeter larger than 1 GeV with a track pointing to the beam-dump production vertex. The absence of any signal above the threshold, satisfying a tight directionality cut ($\theta_{track} < 30$ mrad), provided stringent limits on axions and photinos.

LDMX LDMX is a missing-momentum experiment proposed at SLAC that will use the LCLS-II 4 GeV e^- beam [74]. The detector is made by a silicon tracker surrounding a 10% X_0 tungsten thin target to measure each incoming and outgoing electron individually, a fast and highly hermetic Si-W sampling EM calorimeter, and a hadron calorimeter used to identify and reject penetrating particles. In the first phase, LDMX plans to collect $\sim 10^{14}$ EOT. Although LDMX is designed for missing-momentum searches using the tracker and the EM calorimeter information (see Sec. 1.8), it can also acts as an ABDE using the EM calorimeter as an active target with a corresponding energy cut of 1.2 GeV.

NA64 The NA64 experiment is an ABDE making use of the 100 GeV secondary electron beam at SPS-CERN. The detector consists of an upstream magnetic spectrometer (tracker + bending magnet), followed by an active target, a Shashlik-type EM calorimeter made of lead and plastic scintillator plates. A signal event is defined as an upstream reconstructed track with less than 50 GeV energy deposited in the EM calorimeter and no activity in the surrounding veto system or in the hadron calorimeter installed downstream. The corresponding detection efficiency, only slightly dependent on $m_{A'}$, is about 50%. At the time this work was carried out, NA64 had accumulated 4.3×10^{10} EOT, with no events measured in the signal search window.

6.2 LDM Production Through Positron Annihilation

6.2.1 Dark Photon Production Mechanisms

As already described in Sec. 2.1.1, positrons can produce A's, other than though A'-strahlung, via the resonant ($e^+e^- \to A'$) and non resonant ($e^+e^- \to A'\gamma$) annihilation

with atomic electrons, as depicted in Fig. 2.3. In the invisible scenario, the produced A' than decay into $\chi\bar{\chi}$ pairs. The formula of the cross section for the resonant process reads:

$$\sigma_r = \sigma_{peak} \frac{\Gamma_{A'}^2/4}{(\sqrt{s} - m_{A'})^2 + \Gamma_{A'}^2/4},$$

where s is the e^+e^- invariant mass squared, $\sigma_{peak} = \frac{12\pi}{m_{A'}^2}$ is the resonant cross section at the peak and $\Gamma_{A'} = \frac{1}{3} m_{A'} \varepsilon^2 \alpha_D$ is the A' decay width in the limit $\frac{m_e}{m_{A'}} \to 0$. For the non-resonant annihilation process the total cross section is:

$$\sigma_{nr} = \frac{8\pi\alpha^2\varepsilon^2}{s} \left[\left(\frac{s - m_{A'}^2}{2s} + \frac{m_{A'}^2}{s - m_{A'}^2} \right) \log \frac{s}{m_e^2} - \frac{s - m_{A'}^2}{2s} \right],$$

where m_e is the electron mass. The corresponding differential cross section reads:

$$\frac{d\sigma}{dz} = \frac{4\pi\alpha^2\varepsilon^2}{s} \left(\frac{s - m_{A'}^2}{2s} \frac{1 + z^2}{1 - \beta^2 z^2} + \frac{m_{A'}^2}{s - m_{A'}^2} \frac{1}{1 - \beta^2 z^2} \right).$$

Here z is the cosine of the A' emission angle in the CM frame, measured with respect to the positron axis, and $\beta = \sqrt{1 - \frac{4m_e^2}{s}}$. These results have been derived at tree level, keeping the leading m_e dependence to avoid non-physical divergences if $|z| \to 1$. To avoid infrared divergences when $\to m_{A'}^2$, we applied a low-energy cut-off for the nonresonant mode. We required that the real photon energy in the center-of-mass frame is at least 1% of the impinging positron energy. For a thorough description of the implications of using this cut-off value, see [3].

6.2.2 χ Production Yield

The total $\chi/\bar{\chi}$ yield per electron on target EOT due to positrons annihilation is given by:

$$N_\chi = N_{\bar{\chi}} = N_{A'} Z\rho = \frac{N_A}{A} \int_{E_{min}^R}^{E_{beam}} dE \int_{4\pi} d\Omega T_+(E, \Omega) \sigma(E), \tag{6.1}$$

where A, Z and ρ are, respectively, the beam-dump atomic mass, atomic number and mass density, N_A is Avogadro's number, $\sigma(E)$ is the energy-dependent A' production cross section, and $E_{min}^R = [\frac{m_{A'}^2}{(2m_e)}]$ is the minimal positron energy required to produce a *Dark Photon* with mass $m_{A'}$ through positron annihilation on atomic electrons. Finally, $T_+(E_e)$ is the positrons differential track-length distribution. The track-length distribution $T_+(E_e)$ is defined as the integral over the beam-dump volume of the differential fluence $\Phi(E_e)$, corresponding to the density of particle tracks in the volume [75]. Intuitively, the quantity $T_+(E_e)dE_e$ represents the total path length in the dump taken by positrons with energy in the interval between E_e and $Ee + dE_e$.

6.3 Simulation Procedure

To evaluate the contribution of secondary positrons to the sensitivity of the considered experiments, it is necessary to estimate the expected signal rate $N(\varepsilon, m_\chi)$ as a function of the *Dark Photon*-SM coupling ε, for different values of the χ mass m_χ (for the sake of this work, the ratio between the mass of the χ and the mass of the A' was fixed to $\frac{m_\chi}{m_{A'}} = \frac{1}{3}$). The sensitivity curve in the $y - m_\chi$ plane can be obtained from $N(\varepsilon, m_\chi)$, as explained in Ch. 4. In this section, the simulation chain adopted to evaluate $N(\varepsilon, m_\chi)$ for the 4 considered experiments is described in detail.

6.3.1 Production

The number of produced χ depends on positron track length distribution $T_+(E_e, \Omega)$ differential in energy and angle. To calculate T_+, for a generic electron-thick target setup, the following GEANT4- based procedure was developed. The target (beam-dump) geometry was implemented in the simulation, divided in N layers of thickness Δt, located at a depth t_i, and the differential positron current $I_e^+(E, \theta)$ was sampled on a plane positioned at each t_i (here θ is the positron angle with respect to the primary beam axis). The differential track length $T_+(E, \theta)$ was then obtained by summing over the different planes and multiplying by the layer thickness:

$$T_+(E_e, \theta) = \Delta t \sum_{i=1}^{N} I_e^+(E, \theta, t_i).$$

The values of N and Δt have to be tuned to the primary electron-beam energy and to the beam-dump characteristics. For a multi-GeV electron beam impinging on a thick target with length $L_{dump} \gg X_0$, this procedure yields stable results for $\Delta t < X_0/10$ and $N > 200$ [3]. Using this technique, the differential track length distribution was calculated for each experimental setup considered: E_{beam}= 11 and 20 GeV on an Aluminum target (E137 and BDX), E_{beam}= 4 GeV on a Tungsten target (LDMX), and E_{beam}= 100 GeV on a Lead target (NA64). The same calculation was performed using FLUKA, obtaining good agreement. Figure 6.1 shows the $T^+(E_{e^+})$ distribution obtained from the simulations. In the plot, in order to eliminate the dependence on E_{beam}, results are reported as a function of the scaling-variable $x = E_{e^+}/E_{beam}$. The numerically evaluated track length was used to obtain the total number of χ particles produced in each experiment, using equation 6.1. In order to obtain the energy and angular spread of χs, the positrons energy and angular distribution in the dump was convolved numerically with the kinematic dependence of A'

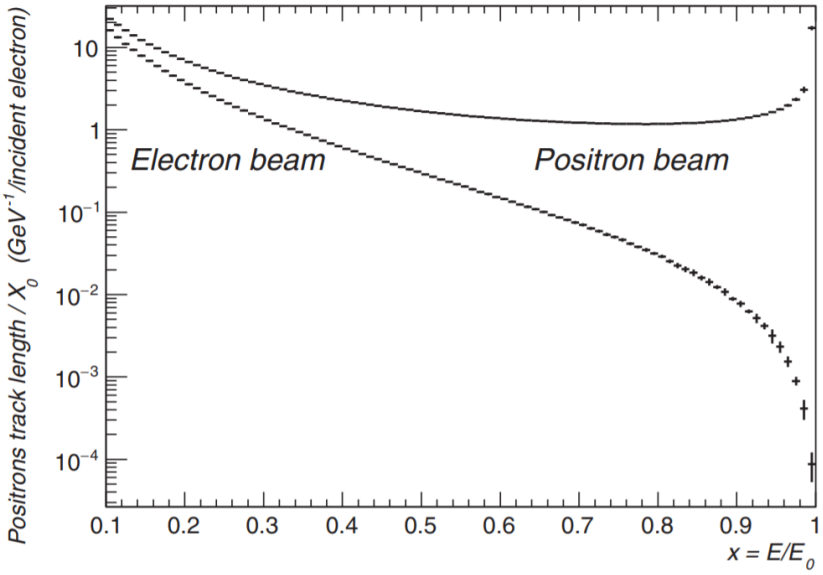

Figure 6.1: Differential track-length distribution as a function of $x = E/E_0$ for positrons produced in a thick target by an impinging e^+/e^- beam, normalized to the radiation length X_0.

production and subsequent decay to χ particles[1] (assumed to be isotropic in the A' rest frame).

6.3.2 Detection

The number of detected events depends on on the the considered experimental setup. For BDE, the χ are detected through the elastic scattering on the electron on the detector. Therefore, the number of signals is given by:

$$N_s = N_{\chi\bar{\chi}} n_e \bar{L} \bar{\sigma}_{\chi e} \epsilon_s, \tag{6.2}$$

where $N_{\chi\bar{\chi}}$ is the total number of χ and $\bar{\chi}$ particles impinging on the detector, $n_e = \rho Z \frac{N_{av}}{A}$ is the electron density of the detector, $\bar{L}$ is the mean path of χs in the detector, $\bar{\sigma}_{\chi e}$ is the total $\chi - e^-$ elastic cross section, integrated over the detection threshold and averaged over incoming χ energy distribution and ϵ_s is the average detection efficiency. In order to obtain $N_{\chi\bar{\chi}}$ I projected the χ angular distribution in the dump to the detector front-face plane and measured the fraction of crossing particles. The mean path $\bar{L}$ and the cross section $\bar{\sigma}_{\chi e}$ were evaluated with a custom MC code, including the $\chi - e$ elastic scattering

[1]For the resonant process, being the energy of the incoming positron mach larger than the energy of the electron at rest, the A' emission was assumed to occur in the same direction of the incoming e^+

differential cross-section formula [35]:

$$\frac{d\sigma_{\chi e}}{dE_R} = 4\pi\alpha\alpha_D\varepsilon^2 m_e \frac{4m_e m_\chi^2 E_R + \left[m_\chi^2 + m_e\left(E - E_R\right)\right]^2}{\left(m_{A'}^2 + 2m_e E_R\right)^2 \left(m_\chi^2 + 2m_e E\right)^2}.$$

Here, E and E_R are, respectively, the incoming χ and the scattered e^- energies. LDM particles were generated on the front face of the detector, following the aforementioned projected distribution; starting from the χ energy, angular and impact point on the detector front-face, the code computed the path length of the particle in the detector, forced its interaction and returned the cross-section and the scattered electron angle and energy.

For ABDE, instead, I computed the number of signal events as the number of A' with energy higher than the detector missing energy cut E_{miss}^{CUT}. The detection efficiency ϵ_s of each considered experiment was determined by applying the same selection cuts used in the original analyses.

6.4 Results

Figure 6.2 shows the 90% confidence level exclusion limits obtained considering the positron annihilation mechanisms in the aforementioned experiments. In case of E137 and NA64, the limit on the number of signal events derived from published data - no events measured and zero background events expected - is $N_{90\%} = 2.3$. For BDX and LDMX, a null background contribution was assumed. A conservative (see Sec. 4.4) efficiency value $\epsilon_s = 0.15$, not dependent on m_χ, was assumed for BDX. The limits are shown in the $y - m_\chi$ parameter space, whith $y = \alpha_D\varepsilon^2\left(\frac{m_\chi}{m_{A'}}\right)^4$. The three continuous black lines represent the thermal relic target for different hypothesis on the LDM nature: elastic and inelastic scalar (I), Majorana fermion (II), and pseudo-Dirac fermion (III).

For some selected kinematics positron annihilation extends by more than an order of magnitude the exclusion limits of the considered experiments. The shape of ABDE lines is related to the high missing-energy threshold. For this class of experiments, the sensitivity at low masses is strongly connected to threshold value, resulting in a sharp dip. For BDE, instead, the threshold effect is less pronounced, since the energy threshold is usually lower, and the dependence on threshold of the sensitivity for low masses is weaker. However, the detection techniques of BDE requires the LDM particles to scatter in the detector, which results in the scaling for the number of signal events $N_s \propto \varepsilon^4$. By comparison, the signal number for ABDE scales as $N_s \propto \varepsilon^2$. As a result, the positron annihilation contribution to the exclusion limits of DBE is wider and less pronounced.

In the right plot I report the exclusion limits, in case of null result, by running future BDE and ABDE with positron beams. The total accumulated (positron) charge and the

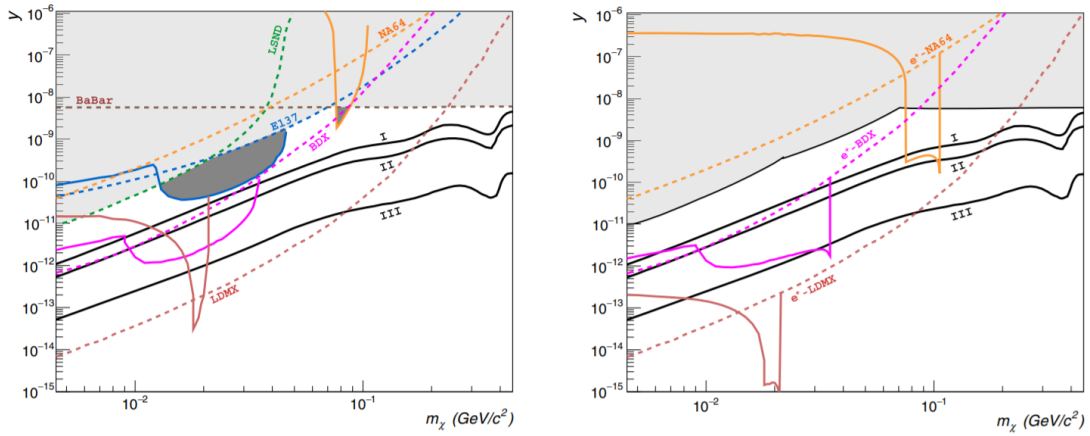

Figure 6.2: **Left:** Continuous lines show exclusion limits at 90% CL for electron BDX e ABDE due to resonant and non-resonant positron annihilation (only). Dashed lines show exclusion limits obtained by A'-strahlung only. The combined exclusion region is shown as filled area: light gray indicates previous limits (including E137, BaBar and LSND); dark gray shows the effect of including positron annihilation on existing. Different colors correspond to the different experiments: E137 (blue), BDX (magenta), NA64 (yellow) and LDM (brown). Limits are given in the $y - m_\chi$ plane, in the assumption $\alpha_D = 0.5$, $m_{A'} = 3m_\chi$. **Left:** The same as in the Left plot but for possible BDE and ABDE with positron beams. Exclusion limits are derived assuming the same (positron) charge and experimental efficiency quoted for the corresponding electron beam setups.

detection efficiency of LDM is assumed to be similar to that of the electron-beam counterparts. Nowadays positron beams with such characteristics are not available, but proposals to run future experiments with positrons at JLab [76] are currently under discussion.

In conclusion, this work proves that, in a positron-rich environment, such as the electromagnetic shower produced by the interaction of GeV electrons or positrons with a beam-dump, e^+ resonant and non-resonant annihilation are two LDM production mechanism competitive with the considered A'-strahlung. In addition, this result strengthens significantly the physics case for BDX, enhancing its sensitivity by ~ 1 order of magnitude in the 10-20 MeV LDM mass region.

Conclusions

The *Beam-Dump eXperiment* is an approved experiment at JLab, searching for light Dark Matter (LDM) particles in the *Dark Photon* theoretical scenario. The experiment makes use of the CEBAF 11 GeV electron beam impinging on the Hall-A beam-dump, in order to produce a secondary LDM beam. LDM particles propagate though some passive shielding reaching a detector placed about 20 m downstream, where they may interact with electrons of the active material producing a detectable signal.

My PhD research covered all aspects of the experiment. BDX was proposed in 2016, and my contribution to the validation and optimization of the experimental setup granted the experiment the JLab Program Advisory Committee approval with maximum rate in 2018. A critical aspect of BDX concerns the evaluation of the beam-related background, i.e. penetrating SM particles produced by the beam in the dump, e.g. neutrinos, which could mimick a LDM particle signal in the detector. The estimate of this background requires Monte Carlo (MC) simulations, making the simulation framework reliability crucial for the experiment. A measurement of the muon flux produced by the 11 GeV electron beam was performed in order to validate simulations. A detector, called BDX-HODO, was lowered in a well dug in the same location of the future BDX experiment and the measured muon flux was compared to rates predicted by simulations. The good agreement proved the reliability of the BDX simulation framework, providing confidence in predictions of unmeasurable (e.g. neutrino) beam-related background.

The sensitivity of the experiment depends on LDM detection efficiency and expected background. A comprehensive study was performed using FLUKA and GEANT4 in order to identify the optimal detector setup and the analysis cuts resulting in the best compromise between detection efficiency and background rejection. This study improved the original detector design providing a set of selection cuts for an efficient neutrino rejection. All these results proved the feasibility of the BDX experiment at JLab and demonstrated the robustness of the proposed experimental technique that, in turn, resulted in the full BDX approval.

While waiting for the run time, the BDX collboration focused on the construction of a small demonstrator, that will provide the first beam-dump measurement at JLab. The detector, BDX-MINI, is composed of a $PbWO_4$ electromagnetic calorimeter enclosed in an active veto system. The measurement is currently ongoing and results are expected for the end of this year. The preliminary sensitivity estimate of BDX-MINI, providing a reach similar to what achieved by previous experiments, suggests a significant discovery potential for the BDX experiment. This study will be used in the BDX-MINI reach evaluation as soon as the data taken will be over.

In addition to the BDX simulations and data analysis, I carried out a phenomenological study about the contribution of secondary particles produced in electron beam-dumps to the LDM production yield, finding a significant enhancement of the reach due to the secondary positrons annihilation. This study significantly increased the portion of LDM parameter space that BDX can explore. This effect, neglected in many other studies, needs to be included in all sensitivity evaluation of electron-beam thick target experiment searching for LDM.

Bibliography

[1] M. Battaglieri et al. Measurements of the muon flux produced by 10.6 GeV electrons in a beam dump, *Nucl. Instrum. Meth.* A925 (2019) 116-122

[2] The BDX Collaboration. Dark matter search in a Beam-Dump eXperiment (BDX) at Jefferson Lab: 2018 update to PR12-16-001, 2018. `https://misportal.jlab.org/mis/physics/experiments/viewProposal.cfm?paperId=943`.

[3] L. Marsicano et al. Dark photon production through positron annihilation in beam-dump experiments. *Phys. Rev.* D 98, 015031, 2018.

[4] L. Marsicano et al. Novel Way to Search for Light Dark Matter in Lepton Beam-Dump Experiments. *Phys. Rev. Lett.*, 121:041802, 2018.

[5] K.A. Olive et al. (Particle Data Group), *Chinese Physics* **C38**, 090001 (2014).

[6] P. A. R. Ade et al. Planck 2015 results. XIII. *Cosmological parameters*. 2015.

[7] Mario Mateo. Dwarf galaxies of the Local Group. *Ann. Rev. Astron. Astrophys.*, 36:435–506, 1998.

[8] Kim Griest and Marc Kamionkowski. Unitarity Limits on the Mass and Radius of Dark Matter Particles. *Phys. Rev. Lett.*, 64:615, 1990.

[9] G. Bertone and J. Silk, *Particle Dark Matter : Observations, Models and Searches*. Cambridge University Press, 2010.

[10] Annika H. G. Peter. Dark Matter: A Brief Review. 2012.

[11] The Planck Collaboration. Planck 2018 results. VI. Cosmological parameters, 2018. arXiv:1807.06209

[12] Gerard Jungman, Marc Kamionkowski, and Kim Griest. Supersymmetric dark matter. *Phys. Rept.*, 267:195–373, 1996.

[13] Savas Dimopoulos and Howard Georgi. Softly Broken Supersymmetry and SU(5). *Nucl. Phys.*, B193:150–162, 1981.

[14] P. Cushman at al., Snowmass CF1 Summary: WIMP Dark Matter Direct Detection 2013.

[15] M. Ackermann et al. Constraining Dark Matter Models from a Combined Analysis of Milky Way Satellites with the Fermi Large Area Telescope. *Phys. Rev. Lett.*, 107:241302, 2011.

[16] Vardan Khachatryan et al. Search for dark matter, extra dimensions, and unparticles in monojet events in protonproton collisions at $\sqrt{s} = 8$ TeV. *Eur. Phys. J.*, C75(5):235, 2015.

[17] Georges Aad et al. Search for dark matter candidates and large extra dimensions in events with a jet and missing transverse momentum with the ATLAS detector. *JHEP*, 04:075, 2013.

[18] D. S. Akerib et al. (LUX Collaboration) Results from a Search for Dark Matter in the Complete LUX Exposure. *Phys. Rev. Lett.* 118, 021303, 2017

[19] Z. Ahmed, et al. Results from the Final Exposure of the CDMS II Experiment. *Science* 327:1619-1621, 2010

[20] E. Aprile et al. (XENON Collaboration) Dark Matter Search Results from a One Ton-Year Exposure of XENON1T. *Phys. Rev. Lett.* 121, 111302, 2018.

[21] Brian Batell, Maxim Pospelov, Adam Ritz. Exploring Portals to a Hidden Sector Through Fixed Targets. *Phys. Rev.* D 80, 095024, 2009.

[22] Jonathan L. Feng. Dark Matter Candidates from Particle Physics and Methods of Detection. *Ann. Rev. Astron. Astrophys.*, 48:495–545, 2010.

[23] Gordan Krnjaic. Probing Light Thermal Dark-Matter With a Higgs Portal Mediator. 2015.

[24] Bob Holdom. Two U(1)'s and Epsilon Charge Shifts. *Phys. Lett.*, B166:196–198, 1986.

[25] J. Alexander et al. Dark Sectors 2016 Workshop: Community Report. 2016.

[26] Marco Battaglieri et al. Dark matter search in a Beam-Dump eXperiment (BDX) at Jefferson Lab, 2016.

[27] Douglas P. Finkbeiner, Silvia Galli, Tongyan Lin, and Tracy R. Slatyer. Searching for Dark Matter in the CMB: A Compact Parameterization of Energy Injection from New Physics. *Phys. Rev.*, D85:043522, 2012.

[28] Tongyan Lin, Hai-Bo Yu, and Kathryn M. Zurek. On Symmetric and Asymmetric Light Dark Matter. *Phys. Rev.*, D85:063503, 2012.

[29] D.E. Kaplan, M. A. Luty, and K. M. Zurek, *Phys. Rev.* D79, 115016 (2009), 0901.4117.

[30] Micheal E. Peskin, Daniel V. Schroeder, (1997) Gauge Theories with Spontaneous Symmetry Breaking. *In: An Introduction to Quantum Field Theory*, Addison-Wesley Publishing Company, 689-730.

[31] David Tucker-Smith and Neal Weiner. Inelastic dark matter. *Phys. Rev.*, D64:043502, 2001.

[32] Michael Klasen, Martin Pohl, Günter Sigl. Indirect and direct search for dark matter. *Progress in Particle and Nuclear Physics,* 2015

[33] M. Battaglieri et al. US Cosmic Visions: New Ideas in Dark Matter 2017: Community Report, 2017. `https://arxiv.org/pdf/1707.04591`.

[34] Bernard Aubert et al. Search for Invisible Decays of a Light Scalar in Radiative Transitions $\Upsilon(3S) \to \gamma A^0$. 2008.

[35] Eder Izaguirre, Gordan Krnjaic, Philip Schuster, and Natalia Toro. New Electron Beam-Dump Experiments to Search for MeV to few-GeV Dark Matter. *Phys. Rev.*, D88:114015, 2013.

[36] Rouven Essig, Jeremy Mardon, Michele Papucci, Tomer Volansky, and Yi Ming Zhong. Constraining Light Dark Matter with Low-Energy e^+ e^- Colliders. *JHEP*, 1311:167, 2013.

[37] J.P. Lees et al. (BaBar Collaboration) Search for Invisible Decays of a Dark Photon Produced in e^+e^- Collisions at BaBar *Phys. Rev. Lett.*, 119, 131804, 2017.

[38] Anson Hook, Eder Izaguirre, and Jay G. Wacker. Model Independent Bounds on Kinetic Mixing. *Adv. High Energy Phys.*, 2011:859762, 2011.

[39] David Curtin, Rouven Essig, Stefania Gori, and Jessie Shelton. Illuminating Dark Photons with High-Energy Colliders. *JHEP*, 1502:157, 2015.

[40] James D. Bjorken, Rouven Essig, Philip Schuster, and Natalia Toro. New Fixed Target Experiments to Search for Dark Gauge Forces. *Phys. Rev.*, D80:075018, 2009.

[41] Mauro Raggi and Venelin Kozhuharov. Proposal to Search for a Dark Photon in Positron on Target Collisions at $DA\Phi NE$ Linac. *Adv. High Energy Phys.*, 2014:959802, 2014.

[42] Paola Gianotti et al. The investigation on the dark sector at the PADME experiment *Nucl. Instrum. Meth.* A936 (2019) 259-260

[43] Mikhail Kirsanov, Recent results of the NA64 experiment at the CERN SPS *EPJ Web Conf.* 212 (2019) 06005

[44] LDMX experiment, https://confluence.slac.stanford.edu/display/MME/Light+Dark+Matterm+Experiment.

[45] F. Petricca et al. (CRESST Collaboration) First results on low-mass dark matter from the CRESST-III experiment. *J. Phys. Conf. Ser.* 1342 (2020) no.1, 012076 arXiv:1711.07692 [astro-ph.CO]

[46] Rouven Essig, Aaron Manalaysay, Jeremy Mardon, Peter Sorensen, and Tomer Volansky. First Direct Detection Limits on sub-GeV Dark Matter from XENON10. *Phys. Rev. Lett.*, 109:021301, 2012.

[47] Rouven Essig, Marivi Fernandez-Serra, Jeremy Mardon, Adrian Soto, Tomer Volansky, and Tien-Tien Yu. Direct Detection of sub-GeV Dark Matter with Semiconductor Targets. 2015.

[48] Brian Batell, Maxim Pospelov, and Adam Ritz. Exploring Portals to a Hidden Sector Through Fixed Targets. *Phys. Rev.*, D80:095024, 2009.

[49] Patrick deNiverville, Maxim Pospelov, and Adam Ritz. Observing a light dark matter beam with neutrino experiments. *Phys. Rev.*, D84:075020, 2011.

[50] Patrick deNiverville, David McKeen, and Adam Ritz. Signatures of sub-GeV dark matter beams at neutrino experiments. *Phys. Rev.*, D86:035022, 2012.

[51] R. Dharmapalan et al. Low Mass WIMP Searches with a Neutrino Experiment: A Proposal for Further MiniBooNE Running. 2012.

[52] L. B. Auerbach et al. Measurement of electron - neutrino - electron elastic scattering. *Phys. Rev.*, D63:112001, 2001.

[53] A. A. Aguilar-Arevalo et al. Dark matter search in nucleon, pion, and electron channels from a proton beam dump with MiniBooNE. *Phys. Rev.* D98:112004, 2018.

[54] Bernard Aubert et al. The BaBar detector. *Nucl. Instrum. Meth.*, A479:1–116, 2002.

[55] F. Ameli et al. A low cost, high speed, multichannel analog to digital converter board. *Nucl. Instrum. Meth.*, A936:286-287, 2019

[56] A. Ferrari, P. R. Sala, A. Fasso, and J. Ranft. FLUKA: A multi-particle transport code (Program version 2005). Technical Report CERN-2005-010, SLAC-R-773, INFN-TC-05-11, 2005.

[57] S. Agostinelli et al. Geant4 - A Simulation Toolkit, *Nuclear Instruments and Methods* A 506. 2003, 250-303

[58] T. Whitlatch, S. Chandra, K. Trembly, Private communication, 2018.

[59] E. Winslow, C. Curtis, T. Michalski, Private communication, 2018.

[60] D. Lawrence, Multi-threaded event reconstruction with JANA. *Journal of Physics: Conference Series*, 119, 4. 2008.

[61] M. Ungaro, Clas12 GEANT4 simulation package GEMC, 2016, `http://gemc.jlab.org`.

[62] V.I. Tretyak, Semi-empirical calculation of quenching factors for ions in scintillators, *Astropart. Phys.* 33 (2010) 40.

[63] M. Bondi et al. Large-size CsI(Tl) crystal read-out by SiPM for low-energy charged-particles detection, *Nucl. Instr. and Meth.*, A867:148, 2017.

[64] Johan Alwall, Pavel Demin, Simon de Visscher, Rikkert Frederix, Michel Herquet, et al. MadGraph/MadEvent v4: The New Web Generation. *JHEP*, 0709:028, 2007.

[65] G. Battistoni, A. Ferrari, M. Lantz, P. R. Sala, and G. Smirnov. A neutrino-nucleon interaction generator for the FLUKA Monte Carlo code. In *12th International Conference on Nuclear Reaction Mechanisms Varenna, Villa Monastero, Italy, June 15-19, 2009*, pages 387-394, 2009.

[66] G. Battistoni, P. R. Sala, M. Lantz, A. Ferrari, and G. Smirnov. Neutrino interactions with FLUKA. *Acta Phys. Polon.*, B40:2491-2505, 2009.

[67] C. Andreopoulos et al. The GENIE Neutrino Monte Carlo Generator. *Nucl. Instrum. Meth.*, A614:87-104, 2010.

[68] I. C. Appleton, M. T. Hogue, and B. C. Rastin. A study of the muon momentum spectrum and positive-negative ratio at sea-level. *Nucl. Phys.*, B26:365-389, 1971.

[69] W. Verkerke, D.P. Kirkby, The RooFit toolkit for data modeling, in Proceedings for CHEP03 (2003).

[70] S. Andreas, C. Niebuhr, and A. Ringwald, *Phys. Rev.* D 86, 095019 (2012).

[71] J. D. Bjorken et al. Search for neutral metastable penetrating particles produced in the SLAC beam dump. *Phys. Rev.* D 38, 3375 (1988).

[72] J. Mans (LDMX Collaboration), *EPJ Web Conf.* 142, 01020 (2017).

[73] D. Banerjee et al. (The NA64 Collaboration), Search for vector mediator of dark matter production in invisible decay mode. *Phys. Rev.* D 97, 072002 (2018).

[74] T. Raubenheimer et al. DASEL: Dark Sector Experimentsat LCLS-II, (2018), `arXiv:1801.07867[physics.acc-ph]`.

[75] A. Chilton, A note on the fluence concept. *Health Physics* 34, 715 (1978).

[76] L. Marsicano, Searching for dark photon with positrons at Jefferson Lab *AIP Conference Proceeding* 1970. 020008. 10.1063/1.5040202 (2018)